2012

Investigating the Relationship Between Material Property Axes and Strain Orientations in Cebus Apella Crania

Christine M. Dzialo

University of Massachusetts Amherst, christinedzialo@gmail.com

INVESTIGATING THE RELATIONSHIP BETWEEN MATERIAL PROPERTY AXES AND STRAIN ORIENTATIONS IN CEBUS APELLA CRANIA

A Thesis Presented

by

CHRISTINE MARY DZIALO

Submitted to the Graduate School of the

University of Massachusetts Amherst in partial fulfillment

of the requirements for the degree of

MASTER OF SCIENCE IN MECHANICAL ENGINEERING

September 2012

Department of Mechanical and Industrial Engineering

INVESTIGATING THE RELATIONSHIP BETWEEN MATERIAL PROPERTY AXES AND STRAIN ORIENTATIONS IN CEBUS APELLA CRANIA

A Thesis Presented

by

CHRISTINE MARY DZIALO

Approved as to style and content by:

_____

Ian Grosse, Chair

_____

Robert Hyers, Member

_____

David Strait, Member

_____

Donald Fisher, Department Head

Department of Mechanical and Industrial Engineering

ACKNOWLEDGMENTS

I would like to thank my lab mates and fellow graduate students: Sarah Wood, Briana Tomboulian, Mike Berthaume, Jay Breindel, Andrew LaPre, Krishna Samavedam, Lieselle Trinidad, Lu Huang, Jeff McPherson, Vivek Premkumar, and Sameer Jade: without you guys, I'd be lost.

Last but certainly not least, I would like to thank my family and friends for their endless support and encouragement.

ABSTRACT

**INVESTIGATING THE RELATIONSHIP BETWEEN MATERIAL PROPERTY
AXES AND STRAIN ORIENTATIONS IN CEBUS APELLA CRANIA**

September 2012

CHRISTINE MARY DZIALO, B.S., SMITH COLLEGE

M.S.M.E., UNIVERSITY OF MASSACHUSETTS AMHERST

Directed by: Professor Ian Grosse

In this research we used probabilistic finite element analysis to determine whether there
is a statistically significant relationship between maximum principal strain orientations
and orthotropic material stiffness orientations in a primate cranium during mastication.
Before carrying out the probabilistic finite element analysis, we sought to validate our
cranium finite element model. This validation involved sampling *in-vivo* strain and *in-
vivo* muscle activation data during specimen mastication, the collection of specimen-
specific post-mortem data of physiological cross sectional area of masticatory muscles,
and post-mortem measurement of orthotropic material properties of the cranium. We used
various geometric-modeling permutations of a previously constructed finite element
model of the cranium of a tufted capuchin monkey (*Cebus apella*) individual called
Curly. Curly's *in vivo* bone strains and electromyography signals were obtained at the
University of Chicago as the individual masticated hard food items. At Baylor College of
Dentistry post-mortem *in vitro* experiments were carried out to gather orthotropic

material property values for Curly, and at Duke University post-mortem *in vitro* experiments provided Curly's PCSA values of its masticating muscles. A comparison of *in vivo* and finite element predicted (i.e. *in silico)* strains was performed to establish the realism of the FEM model. To the best of our knowledge, this thesis presents the world's only complete *in-vivo* coupled with *in-vitro* validation data set of a primate cranium FEM. In general, reasonably good agreement was obtained at most of the strain sampling locations. Thus, our results indicate that a validated FEM of a *Cebus apella* cranium was achieved. This gives collaborating anthropologists, biologists, and engineers the confidence that these models have sufficient accuracy to address the research questions pertaining to cranial structure morphology.

Probabilistic finite element analysis design was then utilized to determine the dependence of maximum principal strain orientations on material stiffness orientations in particular craniofacial regions during mastication. It was discovered that the relationship between material stiffness and maximum principal strain orientations is more localized and does not have a consistent global trend. This suggests that the maximum principal strain orientations are more dependent on loading conditions and/or the shape of and location in the cranium rather than the material stiffness orientation of a particular region. It was also uncovered that the material stiffness orientations are not developed in a way that is optimal for feeding biomechanics from the perspective of minimization of total elastic strain energy. Therefore, a more thorough examination of biting/chewing situations is needed to fully understand the co-evolution of bone morphology and material properties in the facial skeleton. Results from this research will provide insights into the co-evolution of bone morphology and material properties in the facial skeleton.

TABLE OF CONTENTS

Page

CHAPTER

LIST OF TABLES

LIST OF FIGURES

CHAPTER 1

INTRODUCTION

Anthropologists, biologists, and engineers have been collaborating recently to investigate the impact of feeding biomechanics on cranial structure morphology using finite element analysis (FEA). Each field contributes to this research topic, especially regarding the application of anatomically correct boundary conditions and the proper interpretation of results from finite element analyses (Dumont, E. R., et al., 2011; Dumont, E. R., et al., 2005; Rayfield, E. J. , 2007; Richmond, B. G., et al., 2005; Ross, C. F., et al., 2005; Strait, D. S., et al., 2005; Strait, D. S., et al., 2007; Wood, S. A., et al., 2011). Feeding behaviors are believed to influence the evolution of craniofacial morphology as natural selection induces adaptation in skull form to improve mechanical performance during feeding. This Master's Thesis examines one aspect of feeding mechanics that may have evolved in this fashion. Specifically, this Thesis uses a probabilistic design FEA to determine whether there is a significant relationship between the maximum principal strain orientation and the material property axis orientation in particular cranial regions during mastication. This may provide insights into the co-evolution of bone morphology and material properties in the facial skeleton.

This study will be undertaken on the tufted capuchin (*Cebus apella*). This species has emerged as a model organism for studying feeding adaptations because it possesses highly derived craniodental features that are thought to be evolutionary adaptations for feeding on mechanically challenging food items (Dumont, E. R., et al., 2005; Berthaume, M., et al., 2010; Lucas, P. W. , 2004; Strait, D. S., et al., 2010; Strait, D. S., et al., 2009;

Wright, B. , 2005).   Tufted capuchins are New World monkeys belonging to the subfamily *Cebinae*, which contains two genera *Cebus* (capuchins) and *Saimiri* (squirrel monkeys). Capuchins are known for their dietary flexibility (Swindler, D. R. , 2002). Among anthropoids (monkeys, apes and humans), *C. apella* possesses the thickest molar enamel which is believed to be related to its diet of fruits with hard food covers (Shellis, R. P., et al., 1998). Thick tooth enamel is often interpreted as an adaptation that prolongs tooth life in species that consume hard or tough the foods (Vogel, E. R., et al., 2008). While *C. apella* prefers soft foods, it relies on hard, tough, and stiff food items during periods when preferred foods are not available. (Wright, B. , 2005). There is a growing consensus that the consumption of such "fallback foods" (Marshall, A., et al., 2007) may be an important selection pressure influencing the evolution of skull form in primates.

Another reason for examining *C. apella* is that we have the necessary *in vivo* experimental data to validate the FEM process. This work is very time consuming, and the amount of data collected is limited regarding the number of sample regions. Only so many strain gages can be implanted, usually averaging two to three strain gages per experiment. Nonetheless, finite element models of only one other vertebrates species (*Macaca fascicularis,* another primate) have been validated using *in vivo* bone strain data ((Strait, D. S., et al., 2005; Strait, D. S., et al., 2007; Strait, D. S., et al., 2009; Strait, D., et al., 2008; Kupczik, K., et al., 2007; Kupczik, K., et al., 2009)). Thus, the opportunity to validate a cranial FEM of *C. apella* is exceptional.

The method of finite element analysis is advantageous with regard to investigating craniofacial strains because it allows investigators to look at resulting strains all over the skull. Moreover, by using FEA, researchers are able to reconstruct

stresses and strain present at a given instance during the mastication process and test hypotheses regarding the evolution of the skull due to mechanical adaptation (Rayfield, E. J. , 2007; Richmond, B. G., et al., 2005; Strait, D. S., et al., 2005; Wroe, S., et al., 2007). Finite Element Analysis enables researchers to predict the performance of man-made devices and furthermore view the stresses and strains of a system in three dimensions (Richmond, B. G., et al., 2005). The technique is used to digitally reconstruct a structure into a mesh, assign material properties, apply boundary conditions, and solve for the stress, strain, and deformation within the model. The structure is divided into a finite number of elements (rods, plates, bricks, etc). Nodes interconnect elements, with the number of nodes per element depending on the geometry of that element. The complexity of geometry in FEA (1D to 3D, 4-noded tetrahedral to 10-noded tetrahedral, etc) is directly proportional to computational time and the potential for more realistic stress and strain results.

This thesis often uses the term "*in silico*" to refer to the results obtained through computer simulation of finite element analysis (FEA). Strain is the biomechanical quantity of interest to compare *in silico* and *in vivo* data. Average strain in one dimension is defined as the change of length over the original length ($\varepsilon = \Delta l/l$). The definition for average stress in one dimension is the applied force over a certain area ($\sigma = F/A$). However, a more mathematically rigorous definition is required to describe three-dimensional infinitesimal stress and strain (Rayfield, E. J. , 2007; Richmond, B. G., et al., 2005). The strain tensor is given by

$$\varepsilon_{ij} = \frac{1}{2}\left(\frac{\partial u_i}{\partial x_j} + \frac{\partial u_j}{\partial x_i}\right)$$

<div align="right">1)</div>

where the displacement vector is defined by u, i and j are the indices of the three dimensional space {1, 2, 3}, and x takes the form of the coordinate of interest. The stress tensor (2) is a force per unit area and is related to strain in a linear elastic material by Hooke's law (Cook, R., et al., 2002).

$$\sigma = \begin{bmatrix} \sigma_{xx} & \sigma_{xy} & \sigma_{xz} \\ \sigma_{yx} & \sigma_{yy} & \sigma_{yz} \\ \sigma_{zx} & \sigma_{zy} & \sigma_{zz} \end{bmatrix}$$

<div align="right">2)</div>

Nine stress components, defined by two subscripts, make up the stress matrix. The first subscript represents the direction of the surface normal upon which the stress acts. The second subscript represents the direction of the stress component.

One main advantage of FEA in biomechanics is the ability to build accurate FEM through validation, and then using alterations of model geometry material properties and external forces to fit in-vivo bone strain (Ross, C. F., et al., 2005; Kupczik, K., et al., 2007; Bright, J. A., et al., 2011; Ross, C. F., et al., 2011; Ross, C. F., 2008; Schileo, E., et al., 2007). Another aim is the use of FEM to investigate how fossil skulls might have functioned during life (Ross, C. F., et al., 2005; Strait, D. S., et al., 2005). The sensitivity of FEA results to their input parameters is essential to determine how close the FEA model mimics reality (Ross, C. F., et al., 2005; Strait, D. S., et al., 2005; Kupczik, K., et al., 2007; Bright, J. A., et al., 2011; Wang, Q., et al., 2008). "If the assumption used to

build the models are inaccurate, then the results will be inaccurate also" (Bright, J. A., et al., 2011), this demonstrates the importance of sensitivity analyses. The geometry, boundary conditions, and material properties are the main components of FEA modeling, the latter posing the greatest challenge and thus often not modeled realistically. Many studies are still assigning uniform (homogeneous) material properties to the cortical bone of the skulls as a simplifying assumption despite the potential importance of accurate material properties on strain results from FEA (Dumont, E. R., et al., 2011; Kupczik, K., et al., 2007; Wroe, S., et al., 2007; Bright, J. A., et al., 2011). Other researchers are beginning to strive towards anisotropic and heterogeneous material properties (e.g., Strait *et al.,* 2005) through the use of spatial-mapping techniques: on long bones such as the femur (Schileo, E., et al., 2007; Taddei, F., et al., 2007; Tsubota, K., et al., 2009), modeling the PDL (Panagiotopoulou, O., et al., 2011), or constructing a primate skull (Davis, J. L., et al., 2011).

Primate feeding biomechanics is investigated using two methods: by directly examining bone strain (*in-vivo* and *in vitro*) and by developing and interpreting finite element biomechanic feeding models (*in silico*). Hylander (e.g., Hylander, 1978; Hylander *et al.,* 1991) pioneered the measurement of *in vivo* strains in primates, as discussed thoroughly in (Wang, Q., et al., 2008; Ross, C. F., et al., 1996; Ross, C. F. , 2001). *In vivo* bone strains, electromyography (EMG) signals, and X-rays are recorded for each experiment and extracted using custom batch code. During mastication the key muscles that are activated are the left and right superior masseter, deep masseter, anterior temporalis, and the medial pterygoid (Strait, D. S., et al., 2005; Wright, B. , 2005; Taylor, A. B., et al., 2009). From video analysis when *C. apella* initially cracks (bites) a hard

food item the use of the left or right canine is apparent. However, after the crack is initiated, the video captures the use of the premolars. This collection process is further outlined in (Ross, C. F., et al., 2005; Ross, C. F., et al., 2011; Ross, C. F. , 2008; Ross, C. F. , 2001).

In vitro methods are often used to obtain bone material properties and muscle properties from the specimen of interest.   Muscle properties can be determined through dissection of the specimen or through anatomical knowledge and use of X-ray/CT scans (Rayfield, E. J. , 2007). The physiological cross-sectional area (PCSA) data are needed in order to determine more accurate muscle forces exerted during mastication (Ross, C. F., et al., 2005; Taylor, A. B., et al., 2009; Perry, J., et al., 2008). Specimen specific mean fiber lengths (NLf), physiological cross-sectional area (PCSA), and the ratio of muscle mass to predicted effective maximal tetanic tension (M/P0) are typical measurements. The accepted maximum muscle stress researchers use for *C. apella* is 25 N/cm2 (Strait, D. S., et al., 2005; Herzog, W. , 1994; Wood, S. , 2011). This accepted value is multiplied by the PCSA and EMG activation percentage (as collected from *in vivo* experiments), to determine the muscle force firing at a given time (Ross, C. F., et al., 2005; Ross, C. F., et al., 2011). Muscle forces are applied to the FE model in vector form, including magnitudes, direction, and area of application (Davis, J. L., et al., 2010; Grosse, I. R., et al., 2007).

The *in silico* methods of FEA can be used to interpret the skulls resistance to masticatory loads ((Richmond, B. G., et al., 2005; Grosse, I. R., et al., 2007; Huiskes, R., et al., 1983). Computed Tomography (CT) scans are used to create a finite element model of a specimen's skull. Material properties are assigned to the various regions of

the skull, and boundary conditions are applied with respect to the anatomy of the specimen. When the finite element model is solved, this simulates a predefined biomechanical movement. *In silico* data extracted from the solved model is most often three dimensional displacements, strains, and stresses. For FEA validation purposes it is imperative to realize that the strain data recorded from in-vivo strain gages only provides two-dimensional surface strains. Strain is mathematically defined as a second order tensor, so some researchers have resorted to using 2D membrane elements with a very fine thickness (0.001mm) superimposed onto the FEA model in places where the in-vivo strain gages are located. The stiffness of model location covered by the membrane element is not affected because of the thinness of the membrane and its compliant material stiffness (E = 1 MPa). This process allows for 2D strain results to be extracted directly from this surface membrane element (Bright, J. A., et al., 2011). Others have written custom code MATLAB to convert the three dimensional strain output to two-dimensional surface strains (Ross, C. F., et al., 2011).

A topic of much concern is how to properly model the elastic material properties of craniofacial bone. Bone in nature is a composite and heterogeneous material (Rayfield, E. J. , 2007). Also known as anisotropic or orthotropic, these materials vary in elastic properties with respect to direction. For the sake of simplicity, bone is often modeled in FEA as a homogeneous (isotropic) material, consisting of uniform elastic material properties in all directions. Elastic material properties are categorized by force-displacement relations, including the elastic modulus (stiffness of a material), the shear modulus (material stiffness under shear), density (mass over a unit volume), and Poisson's ratio (the strain in the transverse direction divided by the strain in the loaded

direction) (Rayfield, E. J. , 2007). Isotropic materials have uniform elastic properties in all axes orientations. Anisotropic materials differ in elastic properties with respect to direction (axis). Orthotropic materials are also considered anisotropic, with three orthogonal material axes containing different elastic properties in each direction. Orthotropic elastic material properties consist of three elastic moduli (E_1, E_2, E_3), three shear moduli (G_{12}, G_{31}, G_{23}), and six Poisson ratios (v_{12}, v_{21}, v_{13}, v_{31}, v_{23}, v_{32}). The Poisson ratios of orthotropic material properties are often assumed to be symmetric and thus resulting in only three unique values (v_{12}, v_{13}, v_{23}) (Wang, Q., et al., 2006). In this thesis we will designate the maximum stiffness in the cortical plane of the region of interest as E_3. E_1 will be defined as normal to the region's surface. The direction of E_1 will naturally vary greatly with the curvature of the skull. E_1 is consistently less than E_2, the elastic moduli that is perpendicular to E_3 and lies in the plane of the specimen.

Bone can be modeled with isotropic or anisotropic elastic properties (Strait, D. S., et al., 2005; Wang, Q., et al., 2008; Taddei, F., et al., 2007; Berthaume, M., et al., 2012*; Bryan, R., et al., 2010). The breakdown of material property axes in cortical bone mostly consists of two out of three axes approximately parallel to the surface while the third axis is oriented normal to the surface. Thus, surface curvature in craniofacial bone poses a challenge in the modeling bone property axis. In long bones the major anatomical axes often coincide with material axes making it easy to apply orthotropic properties; however in complex anatomy such as the cranium, isotropic materials are usually used for simplicity. In (Strait, D. S., et al., 2005) FEM is used to model a macaque skull in simple isotropy, regional isotropy, and regional orthotropy. In this work the skull was divided into various anatomical regions, each assigned with specific elastic properties (isotropic

or orthotropic), while simple studies apply a constant isotropic elastic property to the entire bone. The ratio (E_2/E_3) is often used to differentiate between these divided regions (Wang, Q., et al., 2006; Peterson, J., et al., 2003). It is not surprising that when was bone modeled with regional orthotropic elastic properties it deformed the most realistically when compared to in-vivo strains (Strait, D. S., et al., 2005; Strait, D., et al., 2008). However with this process, the question arises: what breakdown of anatomical regions is practical? This question and hypothesis are still under investigation and will be investigated in greater detail later in this thesis.

Comparison of *in vivo*, *ex vivo*, or *in vitro* strains and material property orientations to *in silico* results is imperative when determining the realism of a model and ultimately addressing evolutionary questions pertaining to feeding biomechanics (Ross, C. F., et al., 2005; Kupczik, K., et al., 2007; Kupczik, K., et al., 2009; Bright, J. A., et al., 2011; Ross, C. F., et al., 2011). When modeling biological systems it is important to note, "FEA [...] is only as realistic as the variables on which the model is based" (Strait, D. S., et al., 2005). Depending on the desired FEA results, it may be important to measure specimen specific material properties (*in vitro*) when modeling for FEA due to the variability in bone amongst species, specimens, and regions of the bone (Rayfield, E. J. , 2007; Richmond, B. G., et al., 2005). The material property axes of bone vary with bone shape and region (Taddei, F., et al., 2007; Wang, Q., et al., 2006; Peterson, J., et al., 2003; Wang, Q., et al., 2010). Bones that make up the skull include the frontal, parietal, occipital, sphenoid, and temporal bones, each of these bone vary in shape, region, and whether or not the bone muscle-bearing (Peterson, J., et al., 2003). The age of the specimen can alter the material properties in bone as well (Kupczik, K., et al., 2007).

Material mapping strategies are becoming more popular in the FEA of bone. These studies, allowing for spatial variation within the bone, originated with (Helgason, B., et al., 2008). Commercial FE programs allow material properties to be defined as temperature and/or density-dependent, using temperature and/or density as auxiliary variables to alter elastic material properties varying from node to node in an FEM (Davis, J. L., et al., 2011; Bryan, R., et al., 2010; Helgason, B., et al., 2008). Spatially-varying the elastic modulus throughout a FEA model allows for a non-homogeneous (heterogeneous) distribution of material property in voxel-based FEM (volumetric pixel based). Voxel-based technology is another form of FEA modeling approach that directly converts each individual voxel into a 3D finite element. This method minimizes the model construction time. However, it creates models with large quantities of elements drastically increasing computational solve time (Rayfield, E. J. , 2007). The method developed by Helgason et al minimizes the time it takes to apply heterogeneous material properties to a FEM of a femur using CT data. Young's modulus (Elastic modulus) values are assigned to each node using a nonlinear relationship acquired by comparison to bone ash density and a linear relationship by comparison to temperature. A solution is provided for the structural complications by increasing the precision of the model by assigning highly complex material properties to bone. Although this process is likely to simplify the assignment of orthotropic materials it does require the use of a voxel-based FEM (Helgason, B., et al., 2008). A downside to voxel-based FEM is that the correlation coefficient of cortical bone density to Young's modulus is relatively low (Davis, J. L., et al., 2011). Davis uses techniques developed by (Helgason, B., et al., 2008) to spatially vary material properties in skulls, assigning experimentally measured material properties

to the corresponding specific locations in the FE mesh. In (Davis, J. L., et al., 2011) three FE models were created; the Uniform Isotropic (UI) mode, the Regionally Isotropic (RI) model, and the Thermally Graded (TG) model.   The UI model was the most simplistic, assigning uniform bone material properties to the entire skull model. The skull was divided up into 53 anatomical regions for the RI model assigning unique material properties to each region. The thermal-structural functionality in commercial code allowed a full thermal FE model to be solved, creating a temperature-dependent Young's modulus gradient based on heat transfer through the TG model. The results imply that without complete studies of single individuals (regional material properties, *in vivo* strains, and *in silico* strains from an FE model derived from a single individual) modeling bone as a functionally graded isotropic material is relatively easy and accurate (Davis, J. L., et al., 2011). One main advantage of this method is the gradual transitions of material properties, avoiding unrealistic transitions across anatomical regions.   However, this technique is limited to isotropic material properties due to the fact that temperature is a scalar.   A vector or tensor parameter would provide more control of variation of properties.   Using a single scalar as the parameter does not contain the directional properties needed to spatially control the principal material axis of each of the nine orthotropic material constants.

Probabilistic Design is becoming more widely used in biological finite element analyses. This analysis technique is used for assessing the effect of uncertain input parameters and assumptions used in finite element modeling (ANSYS Mechanical APDL Advanced Analysis Techniques Guide, 2011).   These uncertainties may include geometry, boundary conditions, and material properties.   Probabilistic Design

computations extract useful information pertaining to the statistical distribution of response parameters (Olsson, A., et al., 2002). In biology it is nearly impossible to determine material properties through *in vivo* techniques for all locations of the skull. With probabilistic design researchers can randomize the material stiffness orientations of different regions of the skull to obtain the most realistic configuration. With continuous variables, probability density functions are used to define the distribution of random parameters. In biological systems a uniform distribution of continuous variables is highly unlikely, so statistical sampling techniques (Latin Hypercube) are often used in conjunction with Monte Carlo simulations (Berthaume, M., et al., 2012*). ANSYS software contains a Probabilistic Design tool which allows users to predefine a statistical distribution to input variables. The randomized input variables produce results through deterministic FEA. The post-processing portion of this tool yields statistics for output variables, the accuracy of which can be improved by the predetermined sampling rate. The benefits of a simple yet accurate probabilistic design model come with complications, in this case high computational time and memory.

A significant amount of thought and refining goes into FEA model creation; however, there is no guarantee that the results will turn out realistic (Cook, R., et al., 2002). This is why validation is so vital when relying on results from FEA modeling of biological systems. The accuracy and precision both need to be considered. Accuracy is defined as "the closeness of the model's results to the real biological situation" while precision is defined as "the closeness of the model's results to the exact solution of that biomechanical model"(Richmond, B. G., et al., 2005). The mathematical definition of precision is repeatability, and in the context of FEA this pertains to the concept of

discretization error.   To gain more accurate results in-vitro (Ross, C. F., et al., 1996) and

in-vivo (Ross, C. F. , 2001; Hylander, W. L., et al., 1989) data need to be considered. A

broad data collection needs to be done in order to accurately build a biological FE-model,

including: PCSA values, material property and orientations, EMG, and strain gage data

(Rayfield, E. J. , 2007).   Increasing precision of a model highly correlates with

convergence testing. Convergence testing can be achieved by creating increasingly finer

meshes until a particular solution reaches a plateau (Richmond, B. G., et al., 2005). This

is very time consuming as the complexity of the model increases, and is virtually

impossible for cranium models without significant computational resources.

The validation *in silico* results through use of in-vivo data has been achieved in

macaques (Strait, D. S., et al., 2007; Ross, C. F. , 2001), but in those studies the

individuals being used in the *in vivo* and *in silico* studies were not the same.   The

research presented in this thesis is the first of its kind in the area of cranial biomechanics

regarding a specimen specific comparison of *in vivo* and *in silico* data. X-rays are used to

determine the location and orientation of the strain gages used during in-vivo strain

experiments. These locations are superimposed onto various FEA models (altered with

regard to dentition simplification methods) of the same specimen allowing the *in-vivo* and

in-silico data to be compared to reasonable accuracy. This will not only validate the FEA

process of primate crania (Wood, S. A., et al., 2011), but also validate any simplification

methods that can be used when modeling the alveolus region. Thus, a great amount of

time will be spent validating a specimen specific model before attacking the hypotheses

of this thesis.

Modeling of bone has been a real challenge in FEA; the elastic properties can vary within and between bones of an individual (Peterson, J., et al., 2003; Wang, Q., et al., 2010; Dechow, P. C., et al., 2010). It is even possible for each element within a finite element model to have its own elastic modulus depending on its geometry and position within the skull (Rayfield, E. J. , 2007). The complexity of a model needs to be monitored; how should the anatomical regions of the skull be segmented in FEA? And will this time consuming manner of modeling material property orientation of each anatomical region increase the accuracy of the model? Peterson and his collaborators hypothesized that "the grain in cortical bone, or the direction of maximum stiffness, aligns in the direction of maximum stress may be a reasonable conjecture about directions of maximum stiffness" (Peterson, J., et al., 2003). Based on previous research and hypotheses, investigating the relationship between material property orientation and maximum strain orientation seems to be an important research topic. Exploring this relationship will require extensive specimen specific data: orthotropic material property data obtained from Professor Paul Dechow, PCSA data from Professor Andrea Taylor, Strain and EMG data collected by Professor Callum Ross, and FEA models created by Professor Ian Grosse's lab. This thesis will tie together these diverse areas and advance our knowledge of evolutionary feeding biomechanics within *C. apella*.

The following chapters describe the objective of this research, the approach taken to test and validate hypotheses relating to the material property orientation, the maximum strain orientation results from the FE studies, and the conclusions that can be drawn from this work.

CHAPTER 2

RESEARCH OBJECTIVE

The research presented in this thesis focuses on investigating the relationship between material property axis orientations in each anatomical segment of the crania and resulting principal strain orientation during a static loading that simulates mastication. A direct trend between these axes will help morphologists better understand cranial development and/or adaptation due to feeding biomechanics. We will also be validating the simplification methods of various cranial features in FEMs proposed in (Wood, S. , 2011). Comparing specimen specific in-silico and in-vivo data will complete the validation process. The validation of Wood's work will allow us to create future specimen specific finite element models that have sufficient accuracy to address the research questions of interest.

This thesis is divided into two main sections; the first portion is a continuation of S.A. Wood's Master's Thesis research regarding the simplification of the alveolus region and presence of PDLs. This section will explore various permutations of Wood's FEMs, ultimately addressing which model most accurately corresponds to the in-vivo specimen specific strain data. The second section investigates the trend (if any) in the material property axis orientation with the maximum and minimum strain orientations under static loading of the crania. We propose the following hypotheses:

(H1)   There is a relationship between orientation of principal strains in anatomical regions of the cranium and orientation of orthotropic material properties.

(H2)   The orientations are such that the work expended by mastication is minimized.

CHAPTER 3

MATERIALS AND METHODS

3.1 Research Approach

In order to ultimately obtain Von Mises stress and strain results, a series of computational techniques were followed as outlined by (Wood, S. , 2011). Computed Tomography (CT) scans of a *C. apella* specimen crania were used. The scans are from an adult male called *Curly.* The stacks of CT slices were imported to Mimics 14.1 (The Materialise Group, Leuven, Belgium) to convert two-dimensional images into a three dimensional surface representations of each specimen. Mimics allows for segmentation of various features; for each study the cortical and trabecular bone were separated. A stereolithography binary file format (*.stl) was then used to export the triangulated surface model and import it into Geomagic Studio 12 (Geomagic, Inc., Research Triangle Park, NC). This software enables the user to cleanup imperfections caused by the segmentation process in order to make a suitable volume mesh. These cleanup methods include smoothing, filling holes, defeaturing, and other finalizing techniques. Once the anatomical surface is modeled to a sufficient level of detail, the surface model is transferred into 3-Matic 6.0 (The Materialise Group, Leuven, Belgium) using the STL binary file format. 3-Matic software is able to perform a variety of design and meshing operations directly on the anatomical data. The volume mesh generated in 3-Matic is exported as a NASTRAN file to be read by the finite element analysis program, Strand7 (Strand7 Pty Ltd, Sydney, Australia), for subsequent finite element analysis.

Periodontal ligaments (PDL) can be defined in multiple teeth or an individual tooth, adding more detail to the model. The process introduced by (Wood, S. , 2011) was followed to create the LUC and LP^3 PDLs using Geomagic software. First, copies of the inside surface of the tooth socket and the outside surface of the tooth roots were made (Figure 1.a-b). The surface orientations were flipped so that the inside surface becomes the outside surface (Figure 1.c-d). Finally the two surfaces were fused together by filling existing holes (Figure 1.e). These surface models can then be meshed in 3-Matic 6.0 to create a 3D volumetric mesh of each PDL which was then exported to a NASTRAN file. The NASTRAN file is read into Strand7 and material properties are assigned to the PDL(s) as stated in (Table 1). Teeth that do not contain PDLs are often simplified by fusing these teeth with the maxilla. This is done using Geomagic by first deleting the tooth root elements in the teeth .stl file by creating holes in each tooth. In addition, the elements located in the sockets of the maxilla are also deleted, exposing holes in each socket. The holes from the sockets and the holes from each tooth are lined up and filled by creating consecutive bridges connecting the two surfaces and finally filling the remaining holes. Once the teeth are fused to the maxilla, they are assigned cortical bone properties in Strand7 (Table 1). Other maxilla modeling techniques that have been investigated include models with empty sockets that do not contain the PDLs and models with leveled off teeth at the gum line (Wood, S. A., et al., 2011).

Table 1: Material models and properties values

Material	Youngs Modulus (GPa)	Poisson's Ratio
Cortical bone	14.5	0.33
Trabecular bone	0.64	0.28
LE PDL	6.8E-04	0.49
Tooth enamel	70	0.30
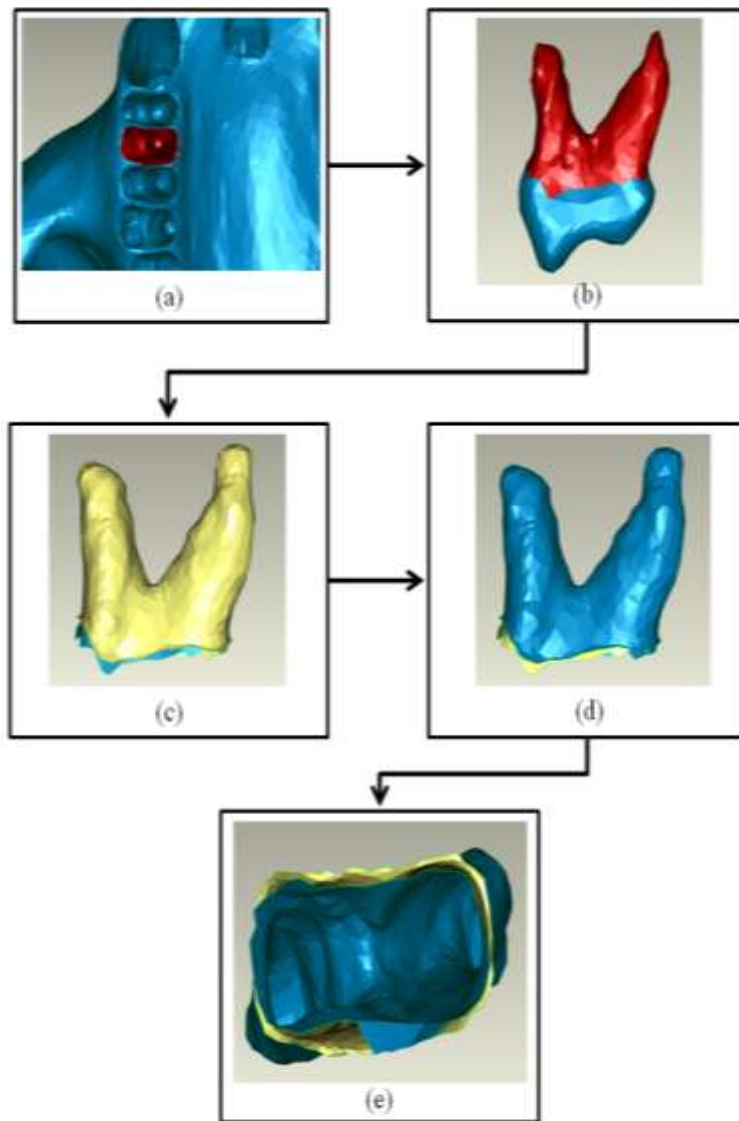
Figure 1: PDL Modeling Process (Wood, S. , 2011)

Three-dimensional volumetric elements are called bricks in Strand7 and take on tetrahedral (4 or 10 nodes), pyramidal (5 or 13 nodes), wedge (6 or 15 nodes), and/or hexahedral (6, 16, or 20 nodes) geometries. Two-dimensional surface elements, also known as shell elements, are called plates in Strand7. The geometry behind plate

elements are either triangular (3 or 6 nodes) or quadrilateral (4, 8, 9 nodes). In the purpose of this research we use 4-noded tetrahedral element models to mesh the bone and teeth volumes. Specifically, 4-noded models contain linear tetrahedral, Tet4, brick elements and constant strain triangle, Tri3, plate elements. In order to line up the nodes of brick and plate elements, specific geometries must be selected. One use of plate elements is in 3D membranes, which are used to model very flexible structures; we used 3D membrane shell elements as a mechanism for applying , muscle forces to the volumetric skull model of brick elements. Applying the muscle forces to mimic feeding biomechanics requires the plate and brick nodes to be lined up together and connected using a particular "zipping" function in Strand7.

In order to simulate accurate feeding biomechanics, forces need to be applied to various locations of the skull to mimic the forces applied by the muscles to the skull during chewing. In these particular studies MATLAB programs entitled *Area Centroids* and *BoneLoad* are necessary to apply muscle forces to the finite element model consistent with the muscle origin and insertion attachments of the crania. *Area Centroids* uses 3-D spatial positioning of the areas and centroids of muscle insertions to enable *BoneLoad* to accurately distribute forces over the muscle origins (Davis, J. L., et al., 2010). The specimen specific muscle properties measured by Professor Andrea Taylor (Duke University) can be are found in **Error! Reference source not found.**. To imitate feeding biomechanics, three specific restraints are required, allowing for the skull to deform elastically in response to muscle forces (Dumont, E. R., et al., 2011). Cranial contact with the mandible is mimicked by fixing nodes at the left and right Temporomandibular joints (TMJ). The right TMJ node was restrained in all directions while the left TMJ

node was left free to move laterally to avoid the model being over constrained (Figure 2.A-B). A third displacement restraint (Figure 2.c) was assigned to the LP3 in the vertical direction (x-axis) to imitate the contact with the hard food item.
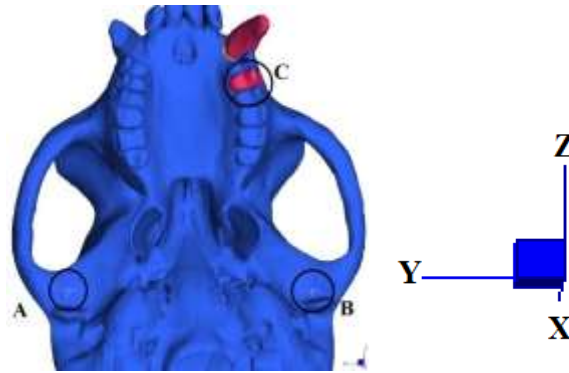
Figure 2: Restraints A) Right TMJ, B) Left TMJ, and C) Loaded tooth

The MATLAB programs "Area Centroid" and "BoneLoad" (Davis, J. L., et al., 2010) are used to simulation the muscle attachment forces. Individual .stl files are created for each muscle insertion and origin, creating 20 files in all (Figure 3.a). The insertion areas of the left and right deep masseter, superior masseter, anterior temporalis, lateral ptyreoid and medial ptreyoid are imported into "Area Centroid to achieve the appropriate muscle origin attachment forces to be imported into *BoneLoad*. *BoneLoad* reads in two files, one data sheet (.xls) and a NASTRAN file containing the muscle origin plates. In order to create such a NASTRAN file, one needs to import the origin muscle .stl files one by one into the Strand7 file that contains the skull one wants to apply the muscle attachment forces to. Then the material properties of cortical bone are applied to the attachments, with a very small thickness (0.001mm). This ensures that these plates have negligible stiffness and negligible strain energy when the model is solved. All of the volumetric (brick) elements are selected and deleted, leaving only the surface

elements (plates).   This file is then exported into a separate NASTRAN file labeled CombinedMuscleAttachment.NAS.   *BoneLoad* can now be run by importing CombinedMuscleAttachment.NAS and BoneLoadinput.xls. In the case of this research the "Gradient Traction" solver was used. The first MATLAB image created by BoneLoad allows the user to check if vector normals are pointed outward (Figure 3.b). The final plot displays the area centroids and the muscle attachment vectors (Figure 3.c). BoneLoad will export a "results summary file" and a "Muscle attachment force.NAS" file that is imported back into Strand 7 as a new *Load Case*. Then the plates and bricks are re-meshed (zipped) to make sure that each pair of coincident nodes are replaced with a single node.
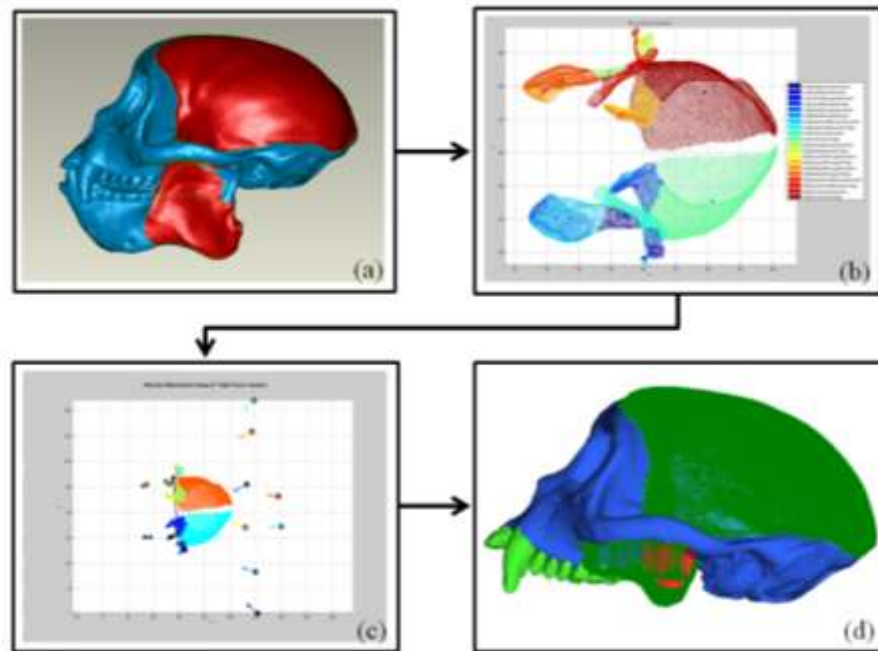
Figure 3: Applying muscle forces to FE mesh (Wood, S. , 2011)

A linear static solver is used for all studies presented in this document using the NASTRAN load-case obtained by methods discussed above. We are only interested in

solving for the brick stress, brick strain, and node reaction results. Based on past methods, linear tetrahedron (i.e. 4-noded) models were solved using the default method. These models range in solving times from 30 minutes to 45 minutes due to the number of nodes present. Once each linear static model is run, the result file can be opened. We extracted both normal and shear strain results at each sample location defined by in-vivo strain gage location (Table 2). These 3D extracted strain components where used to calculate 2D principal strains (discussed below in further detail). The challenge of extracting results from various models was keeping the sample locations consistent. Re-meshing the models altered the location of each individual brick and node; therefore the coordinate location of the brick of interest was used to compare models.

Table 2: Specimen Strain Gage Locations

Specimen	Experiment	Location #1	Location #2
	137	Right zygomatic arch	NA
Curly	155	left anterior pillar	right anterior pillar
	201	right zygomatic arch	NA

3.2 Study 1

This study is a continuation of Sarah A. Wood's Master's thesis research (Wood, S. , 2011). The differences in finite element Models A-D are displayed in Table 3. Model A and C correspond respectively to Models 2 and 3 in S. A. Wood's research. The teeth modeled in Figure 4 are the LP^3 and LUC with PDLs present for both; all other sockets are completely empty. *C. apella* are known for their robust upper and lower canines, used for opening hard coverings of food items (Swindler, D. R. , 2002). By modeling the enlarged upper canine we were able to determine whether it plays an

essential role in accurately predicting the working-side in-silico strains to compare to the actual strains of the specimen *Curly*. The various configurations of the FE model of Curly demonstrate the importance of key features in the maxilla region. Comparing Model B to Model D allowed us to determine the importance of modeling a tooth realistically (with tooth enamel and PDL material properties). Investigating the in-silico strain result indicated which modeling method was most accurate when compared to in-vivo results. The importance of modeling empty sockets versus with teeth present was also examined (comparing Model A to Model B). In addition by comparing Model C to Model D we examined the necessary complexity needed to model the teeth as cortical bone in the maxilla region. Are the local strains affected by the presence of teeth in the maxilla region? To what detail do the teeth need to be modeled? Is there a significant difference between modeling teeth as cortical bone versus as tooth enamel with PDL present? Such questions were investigated in this portion of the thesis to determine the most realistic way to model the *C. apella* cranium.

Table 3: Finite Element Models

Model	Nodes per element	Teeth modeled	Presence/absence of PDL for the teeth being modeled	State of sockets of the teeth that are not being modeled[**]	PDL material model	Loading conditions
A[*]	4	LP^3 and LUC	Present	Sockets completely empty	Linear elastic PDL	Static
B	4	LP^3 and LUC	Present	Other teeth modeled/bone filled	Linear elastic PDL	Static
C[*]	4	LP^3	Present	Sockets capped/bone filled	Linear elastic PDL	Static
D	4	LP^3	Present	Other teeth modeled/bone filled	Linear elastic PDL	Static

*Correspond to Models 2 & 3 in (Wood, S. A., et al., 2011)

The main difference between Model A and Model B was that instead of leaving the sockets empty, the sockets were modeled with the actual teeth shapes and then fused to the maxilla (Figure 4). In addition, the teeth that do not have a PDL (i.e. fused to the maxilla) were assigned cortical bone. The teeth that have a PDL (i.e. LP3 and LUC) were assigned enamel properties as in Model A. Adding in the remaining teeth altered the finite element model in terms of element and node quantity and location. Model A contains 169,594 nodes and Model B has 169,860 nodes. The purpose behind comparing Models A and B was to investigate the impact of modeling teeth in cranium FEM. Human research shows that edentulation may alter the material properties of cortical bone in the craniofacial skeleton (Dechow, P. C., et al., 2010). How much detail is necessary when modeling the maxilla region of the cranium? This particular comparison provides insight on the importance of adjacent teeth to the tooth that comes in contact with the hard food item. The significance was determined when comparing the in-silico deformed cranium to the corresponding specimen specific in-vivo strain data.

In Model C the LUC has been eliminated and the teeth sockets have capped off and filled with cortical bone; the LP3 was modeled as tooth enamel with PDL (Figure 5 top). Model D includes all teeth modeled as cortical bone, except for the LP3 which was model as tooth enamel with PDL (Figure 5 bottom). Models C and D are meshed with four-noded tetrahedral brick elements with 184,935 and 169,860 nodes respectively. The isotropic material properties follow (Wood, S. , 2011) trabecular bone, linear elastic PDL, and tooth enamel (Table 1). The value for cortical bone was achieved by averaging the specimen specific (Curly) orthotropic material properties for each sample area, discussed in more detail below.
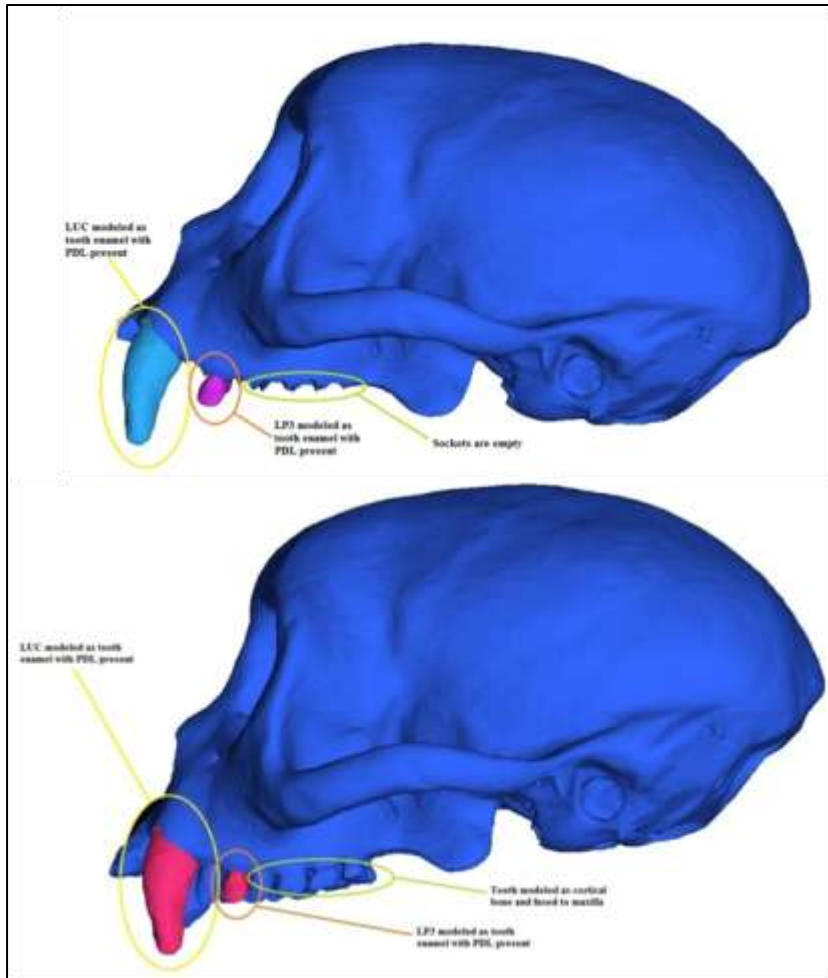
Figure 4: Alveoli modeling for Model A (top) Model B (bottom)   Figure 5 : Alveoli modeling for Model C (top) Model D (bottom)
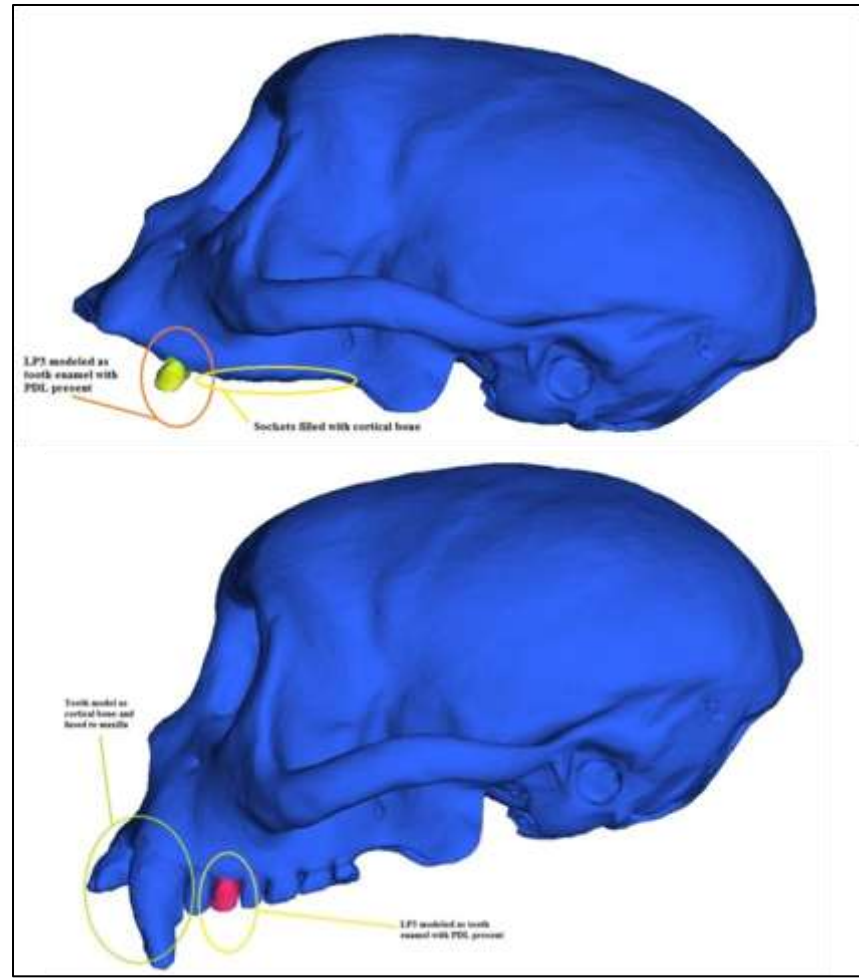
The corresponding areas, centroids, and input muscle forces were based upon previous research with this specimen (Wood, S. A., et al., 2011). The maximum allowable input force of each muscle attachment was calculated by simply multiplying the physiological cross-sectional area (PCSA) by the maximum muscle stress, 25 N/cm^2 (Herzog, W. , 1994), by the EMG activation level (Table 4). Trial 8 (Almond in shell) in Experiment 201 was used to achieve the percentage of muscle activation for each muscle was recorded for per individual chew (power stroke). Accurate EMG signals for each muscle were obtained by extracting in-vivo data using IGOR 4.0 (WaveMetrics, Inc.n Lake Oswego, OR, USA) and custom written code. The EMG data was normalized for each individual muscle. The largest EMG signal was assigned a value of 1.0 (100 % activation) and all other EMG signals for that muscle were normalized compared to the full activation. After normalizing the data, the activation percent was multiplied by the maximum muscle force values in order to create the specimen specific muscle force for a particular food item (Table 4). One chew from Ex 201, Trial 8 was selected to create a *BoneLoad* input file. These specimen specific EMG signals allowed for the FE model of *Curly* to be accurately loaded.

In addition to using Experiment 201, Trial 8 to gain right zygomatic arch strain data; Experiment 155, Trial 06 was also used to achieve stain data at the Left and Right anterior pillars. To do this, we examined left premolar chews resulting in similar EMG levels (when compared to the BoneLoad input file for Experiment 201 Trial 8). The strains were extracted in a similar manner and are discussed in further detail later. For a given experiment (defined by strain gage location), the specimen was sedated for the strain gage and EMG wire implantation done by Professor Callum Ross (University of

Chicago). The procedure is outlined in (Ross, C. F., et al., 2011). The animal recovered for at least an hour before the trials began. An individual trial was defined as ingestion of a single food item by the specimen. For a given experiment, there can be anywhere from 5 to 100 trials. Each trial was video recorded to track the chewing sequences and identify bite type and side. When processing the data from the experiment, each individual video file was viewed to indicate which trials have acceptable data (clarity of chewing side without movement artifacts).

Table 4: Curly's *BoneLoad Input* Muscle Forces (N) with corresponding EMG signals

	Muscle Activated	EMG (%)	Force (N)
Left Side	Deep Masseter	0.52	40.17
	Lateral Pterygoid	0.41	0
	Medial Pterygoid	0.35	47.42
	Superficial-Masseter	0.25	44.73
	Anterior Temporalis	0.69	242.79
Right Side	Deep Masseter	0.68	52.85
	Lateral Pterygoid	0.18	0
	Medial Pterygoid	0.19	25.66
	Superficial Masseter	0.86	155.22
	Anterior Temporalis	0.57	201.13

The strain and EMG data file was loaded into IGOR 4.0 as delineated text; channel numbers were assigned to each wave present (CH01-CH15). A calibration file was written for each trial and saved in binary format then loaded into the IGOR 4.0 as Igor binary; this file converts the strain data-sampling rate of 1000 Hz to microstrain ($\mu\varepsilon$) (Ross, C. F., et al., 2011). The channels were renamed with corresponding strain gage location (each consisting of three waves for Rosette configuration) and EMG wire location (RAT, LAT, etc). The information regarding channel number and corresponding data was found in the experimental notes written by Professor Callum Ross and colleagues; for example paperwork see APPENDIX A (Documentation).

Raw strain data were then sorted and scaled by running through a Butterlow filter at a rate of (1000 Hz). Finally the strain data are decimated and displayed in graph form in order to define principal strains. The EMG data were preprocessed using corresponding sampling frequency recorded in lab notes in **APPENDIX A** (Documentation) and a RMS (root mean square) algorithm to reduce the signal noise. The power strokes (chews) were defined by displaying maximum and minimum principal strains for each strain gage. Defining power strokes at 'PSTART' and 'PEND' allowed for principal strain and EMG data to be selected and processed. The power strokes that occur early were often eliminated due to the manipulation of the food item (rolling around tongue or adjusting location) by the specimen (Figure 6).
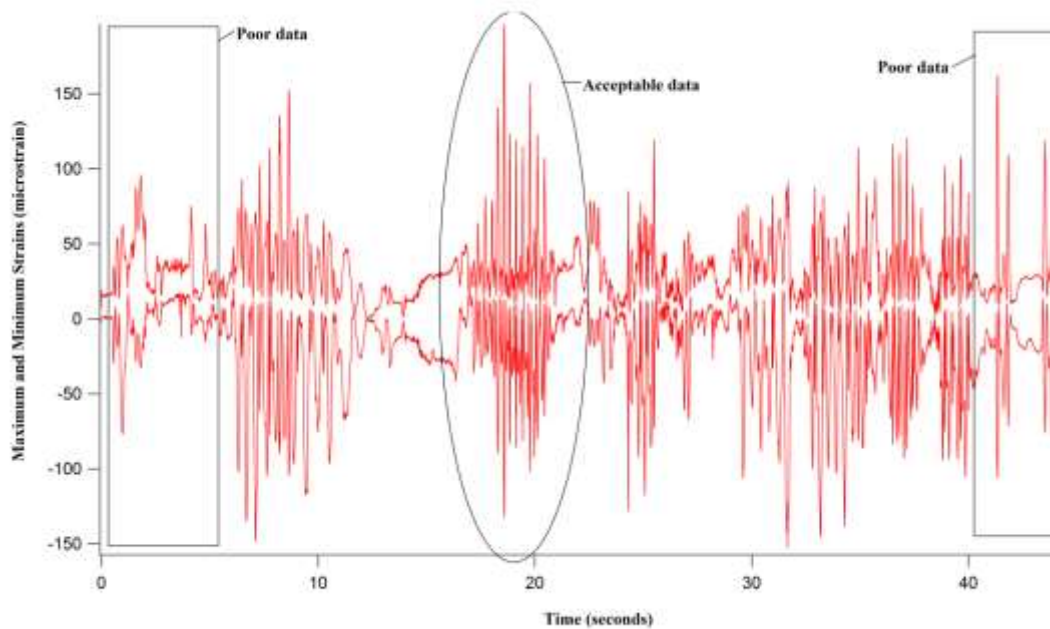
Figure 6 : Mastication of Brazil nut, each peak represents a chew

In addition, power strokes occurring late in the trial were also eliminated if the strains decrease significantly, often being mistaken as noise (Ross, C. F., et al., 2011). Ideal

power strokes occur simultaneously with (or slightly after) peak EMG signals.   A clear image of the animal chewing in the video recording (Figure 7) was necessary for determining the location of the chew. The peak value and peak position (time) for each defined EMG signal was exported along with corresponding minimum, maximum, and shear strains to a spreadsheet. The rosette strain gages used in Professor Callum's lab were rated with a $120.0 \pm 0.8\%$ grid resistance in ohms and $+1.3 \pm 0.2$ TC of gage factor, $\%100°C$.
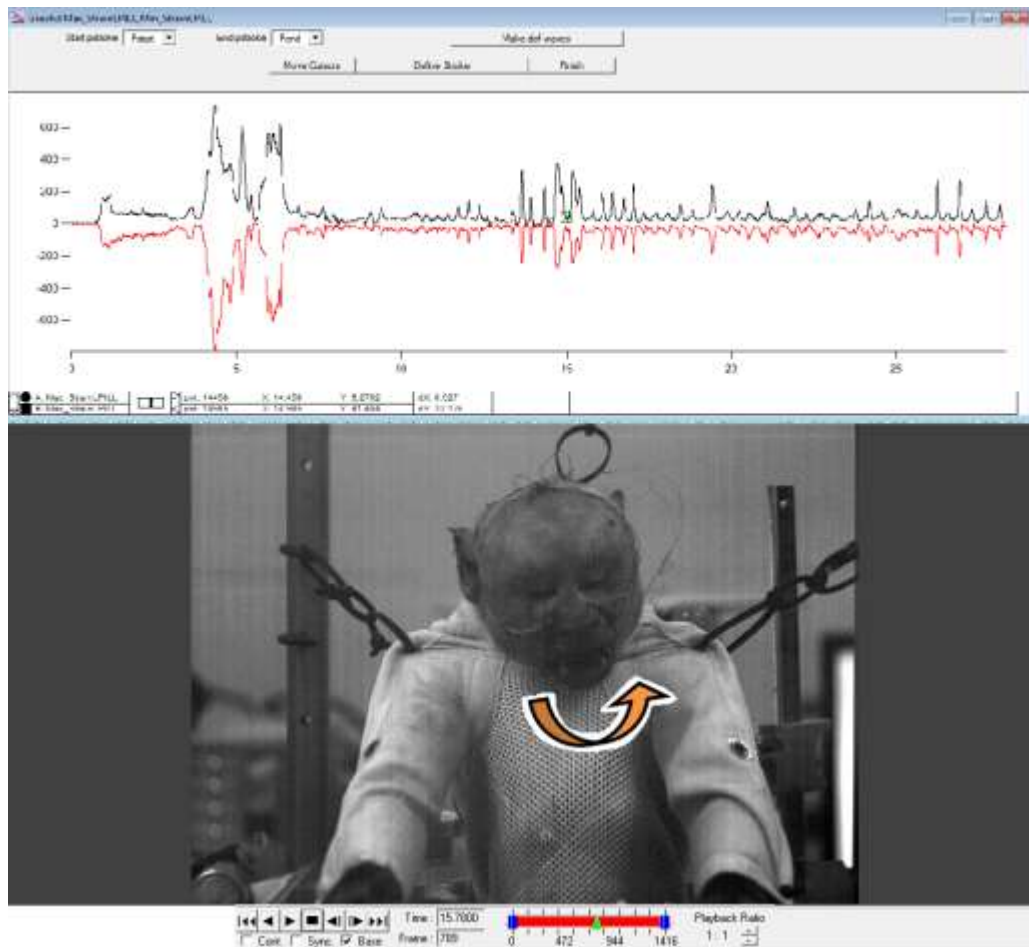
Figure 7: Comparing In-vivo data to Video Analysis

The process of determining the precise location of each strain gage began by obtaining the X-rays taken after each of the experiments conducted in Professor Callum Ross's lab (APPENDIX A). Increasing the brightness and contrast scale of the image and then inverting the colors to a negative scale clarified the location of each strain gage. Since the orientation of the strain gage (location of element A) was not noted in the experimental notes, it was determined by investigating rosette strain gage specifications and then confirmed by Ross. Overlaying the X-ray image (Figure 35 & Figure 36) on the FEA model allowed for a rough location of the strain gage to be determined. Measuring specific anatomical distances on the X-ray (Figure 8.a) and superimposing these distances onto the FEA model image in the same 2D plane (Figure 8.b) allowed the strain gage location to be verified. The exact strain gage location at the right zygomatic arch was unknown due to limited documentation (no x-rays) in Experiment 201. Thus, the location to extract In-Silico model (Figure 9.a) data had to be approximated. This approximation was done by looking at the location of the strain gage (blue box) relative to other facial features in the video analysis of Experiment 201 (Figure 9.b). A prior experiment conducted on *Curly* (Ex 137), implanted a strain gage at the right zygomatic arch and x-rays were present (Figure 9.c). Both the Ex 137 x-ray and image obtained through the Ex 201 video were used to approximate the right zygomatic arch location using overlaying techniques (Figure 9.d). The reason why Ex 137 and Ex 155 were not used when extracting in-vivo data was because Ex 137 did not have EMG data, and Ex 155 had over recorded EMG signals.
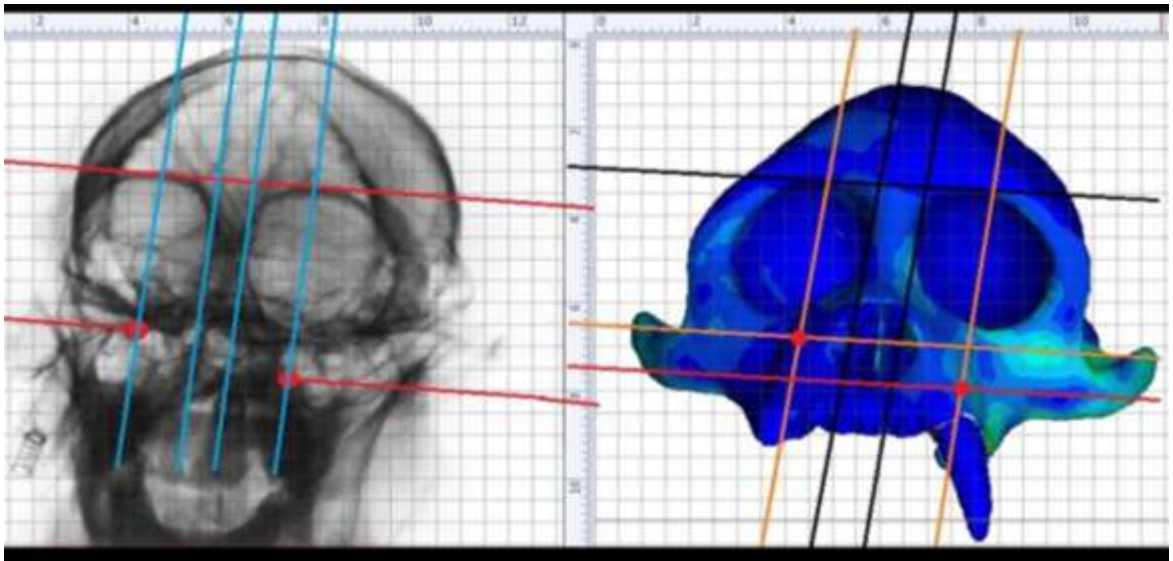
Figure 8 : Measuring anatomical distances (a) in-vivo and (b) in-silico
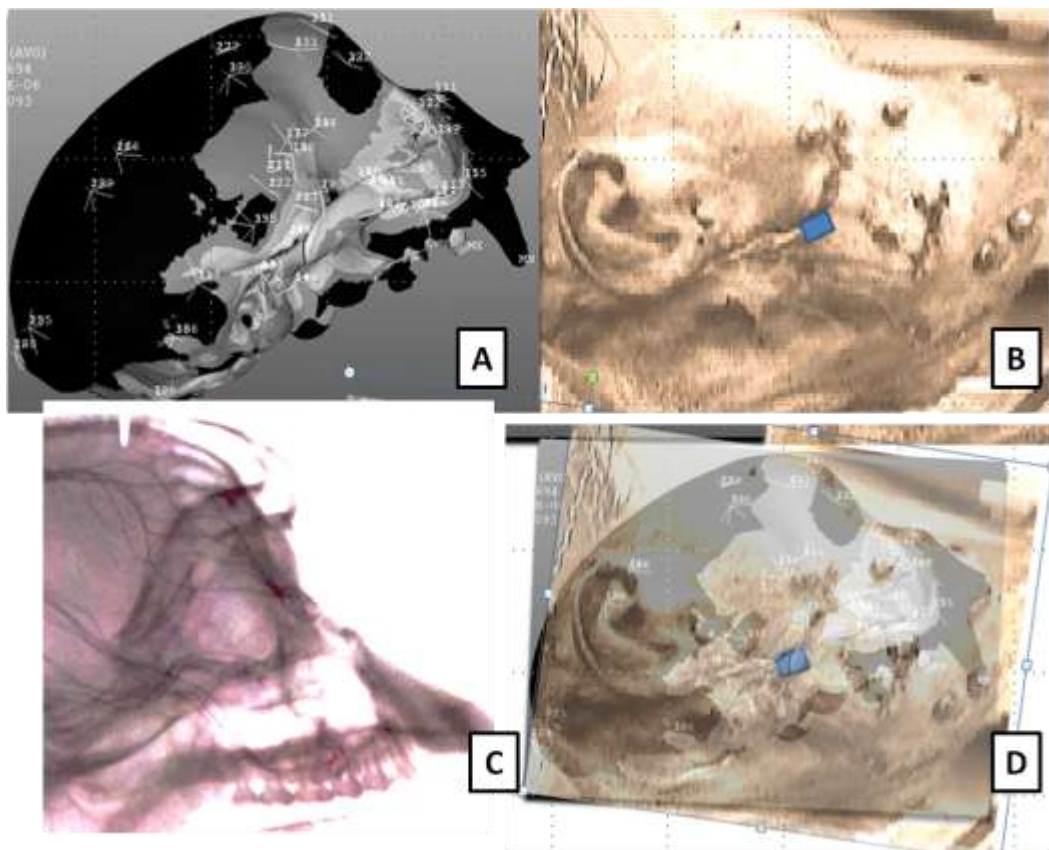
Figure 9: Technique to determine In-Silico location of right zygomatic arch strain gage

Two sampling techniques were employed in attempt to mimic an in-vivo strain gage reading. The first technique assigned the orientation of Element A (0°) to the x-axis when applying a local coordinate system (UCS) to the strain gage location. It is important to note that a local coordinate system was set up on each strain gage location (with x-axis running along Element A of the strain gage). Thus, when recording strains in a particular sample region the corresponding local coordinate system needs to be activated. Also since the in-vivo strain gage only allows us to obtain strains only in the plane of the strain gage, the strains in the normal vector direction from the local coordinate system (the z-axis) need to be removed when solving for principal strains (Ross, C. F., et al., 2011; Berthaume, M., et al., 2012*). The local coordinate system presents six strain components (xx, yy, zz, xy, yz, zx). All strains involving the z-axis (or whatever is normal to the surface of the strain gage location) are removed. Basic mathematics of biaxial state of strain and the remaining three components were used to calculate the maximum and minimum principal strains (**Equation 3**) and principal orientation (**Equation 4**).
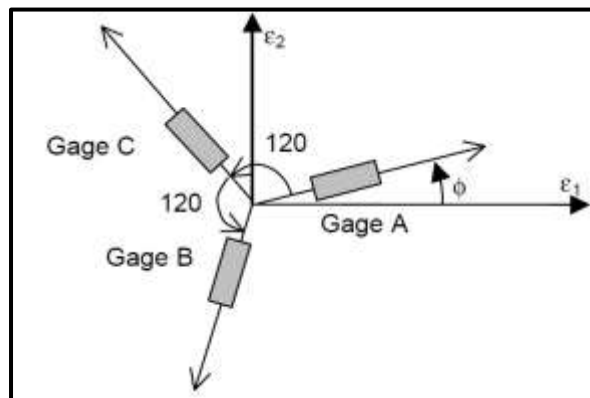
Figure 10: Equilateral strain gage setup

$$\varepsilon_{1,2} = \frac{\varepsilon_{xx} + \varepsilon_{yy}}{2} \pm \sqrt{\left(\frac{\varepsilon_{xx} - \varepsilon_{yy}}{2}\right)^2 + \left(\frac{\gamma_{xy}}{2}\right)^2} \qquad\qquad 3)$$

$$\tan(2\theta_p) = \frac{\gamma_{xy}}{\varepsilon_{xx} - \varepsilon_{yy}} \qquad\qquad 4)$$

The active strain area on the rectangular rosette strain gages used is roughly 5 mm^2. With respect to the FEA model, about six bricks were sampled in the region of the strain gage location to ensure this active strain area was covered. These six bricks define the strain gage area; this area was then moved to four other locations in an "X" pattern (Figure 11). By sampling five different regions using the strain gage area allowed for us to achieve a statistical mean and standard deviation for the in-silico data. It is important that we randomized the sample location because of the difficulty of superimposing the 2D strain gage location accurately onto the 3D model.
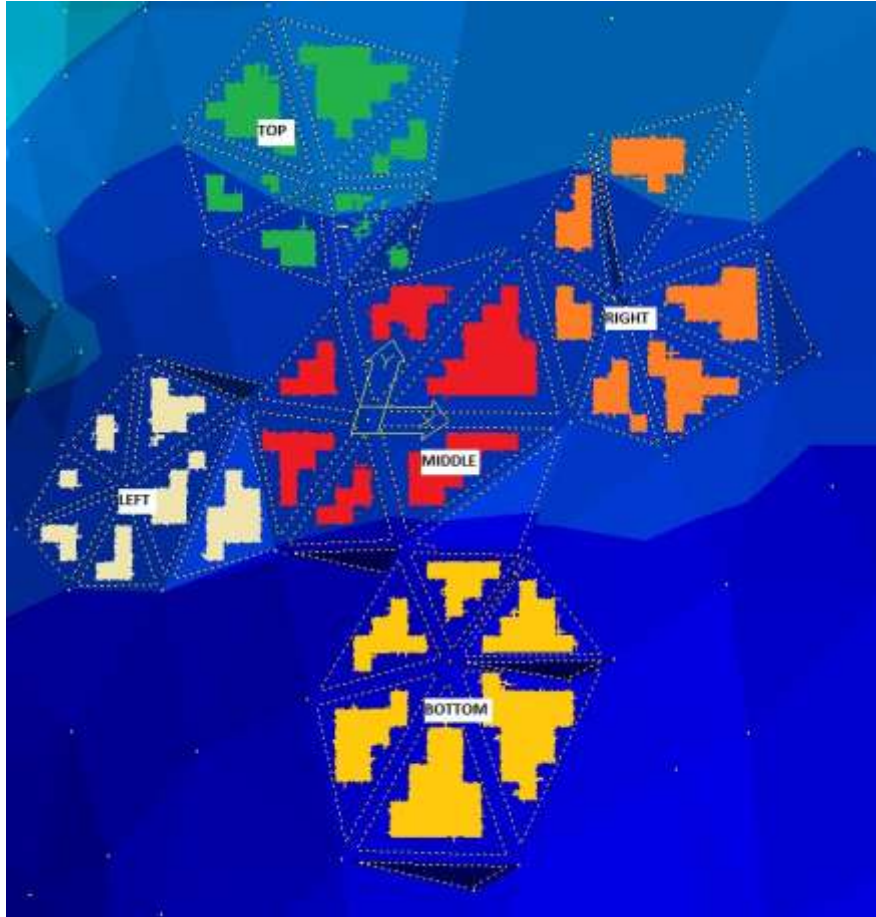
Figure 11: Strain gage sample location 1-5

The second sampling technique that was used assigned a separate local coordinate system to each equilateral gage (Figure 12). The x-axis of each local coordinate system (Gages A-C) was then assumed to be the component strain of that gage. This method allowed us to average 2-3 bricks at each gage site due to the decreased activation area. Standard equilateral principal strain equations were used to calculate the minimum, maximum, and shear strains along with the principal strain orientation (Equations 5 and 6).
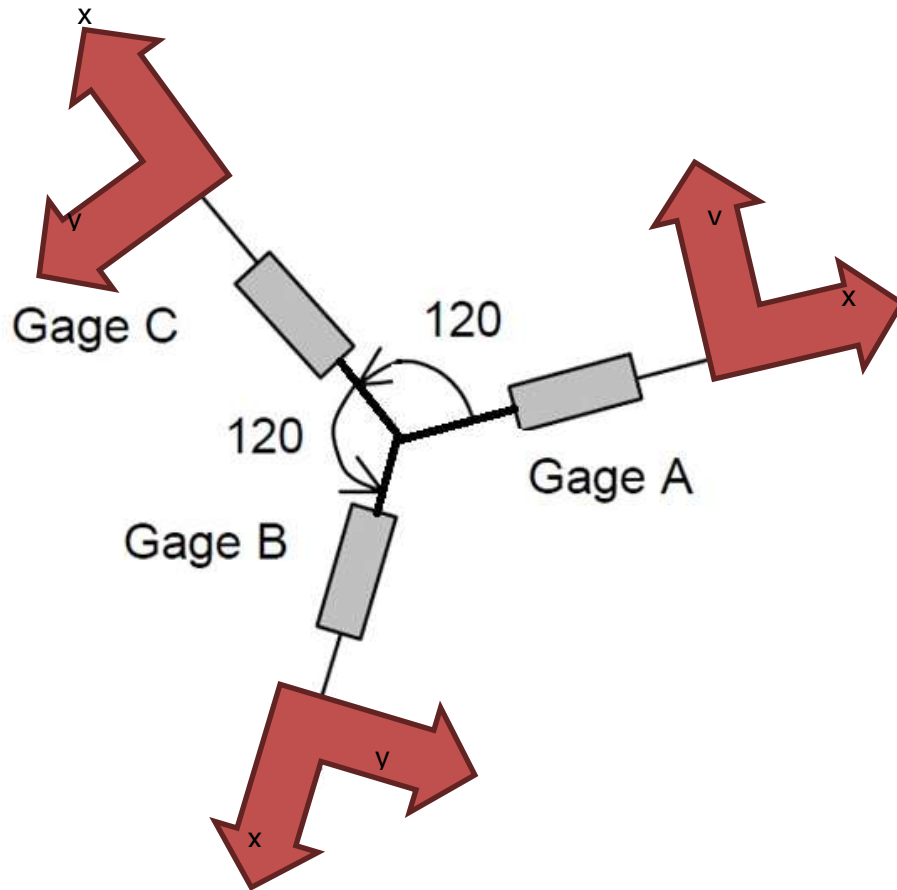
Figure 12: Local Coordinate Systems assigned to equilateral strain gage

$$\varepsilon_{1,2} = \frac{\varepsilon_A + \varepsilon_B + \varepsilon_C}{3} \pm \sqrt{(\varepsilon_A - \varepsilon_B)^2 + (\varepsilon_B - \varepsilon_C)^2 + (\varepsilon_C - \varepsilon_A)^2}$$

5)

$$\theta = \frac{1}{2}\tan^{-1}\left[\frac{\sqrt{3}(\varepsilon_C - \varepsilon_B)}{2\varepsilon_A - \varepsilon_B - \varepsilon_C}\right]$$

6)

Renumbering of elements and nodes amongst models made the recording strain results difficult. The coordinates (x, y, z) of a central node of strain gage area number one (yellow bricks in Figure 11) was recorded from Model A to make certain the strain

gage location stayed consistent between Models A-D. When the coordinates originally measured from Model A can be matched in a node in a different model, the centroid strain values are recorded. However if the new node did not exactly match the coordinates, the average strain values were recorded. The average value of strain components at each node was used to produce the graphical plot below (Figure 13). For instance, the value of strain components at node 5 was calculated by taking the average the values of strain components predicted by elements 1 – 4 that share node 5.
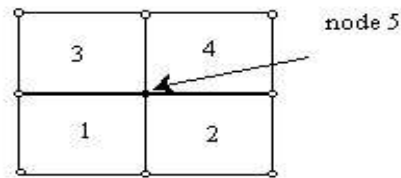
Figure 13: Averaging (Using Strand7: Introduction to the Strand7 Finite Element System, 2010)

In order to validate which model of Curly was the most accurate, the muscle force resultant file from *BoneLoad* was applied to each 4-noded model, and the calculated strain results that were extracted from the In-silico models were examined and compared to the in-vivo data. The in-silico model that was closest to the in-vivo strain data was used for the second study in this thesis. The second study applies specimen specific orthotropic material properties and orientations to *Curly's* model. The results obtained from running the model from Study II were compared to the isotropic models of Study I to investigate the effect of applying more precise material property data to a finite element model.

3.3 Study 2

The Probabilistic Design portion of ANSYS APDL 14.0 was used to investigate the specimen specific FEA model of *Curly*. The skull was subdivided into anatomical segments so we could apply unique orthotropic material properties to various regions. The anatomical regions were based upon past research (Strait, D. S., et al., 2005; Berthaume, M., et al., 2012*) and the available material property sample locations. The model of Curly was subdivided into 32 anatomical regions in Strand7 (Figure 13). Data from Paul Dechow's lab (Baylor College of Dentistry, Dallas, unpublished) defined 8 major regions on the right hand side of the skull (Table 5). The right side of the cranium is depicted below (Figure 15) the left side was assumed to be symmetric, so mirror orientations were assigned to each anatomical segment with corresponding material properties. Regions with larger areas and or drastic curvature were broken down into subgroups, summing to a total of 32 regions. Strand7 was selected on an ease-of-use basis and the efficiency of its grouping technique when compared to ANSYS. Major anatomical regions were first defined by creating a "*New: Group*", and then the brick elements making up the anatomical region were selected. Then each major anatomical region was further separated into subgroups with respect to sampling regions (Figure 14). The desired size and shape of each group was achieved by continuously selecting elements corresponding to that anatomical region. Elements not directly on the surface were selected by using a unique Strand7 setting which hides any already selected elements, exposing what is beneath the surface. This process was done countless times from multiple orientations of the skull to make sure the anatomical regions were properly subdivided.
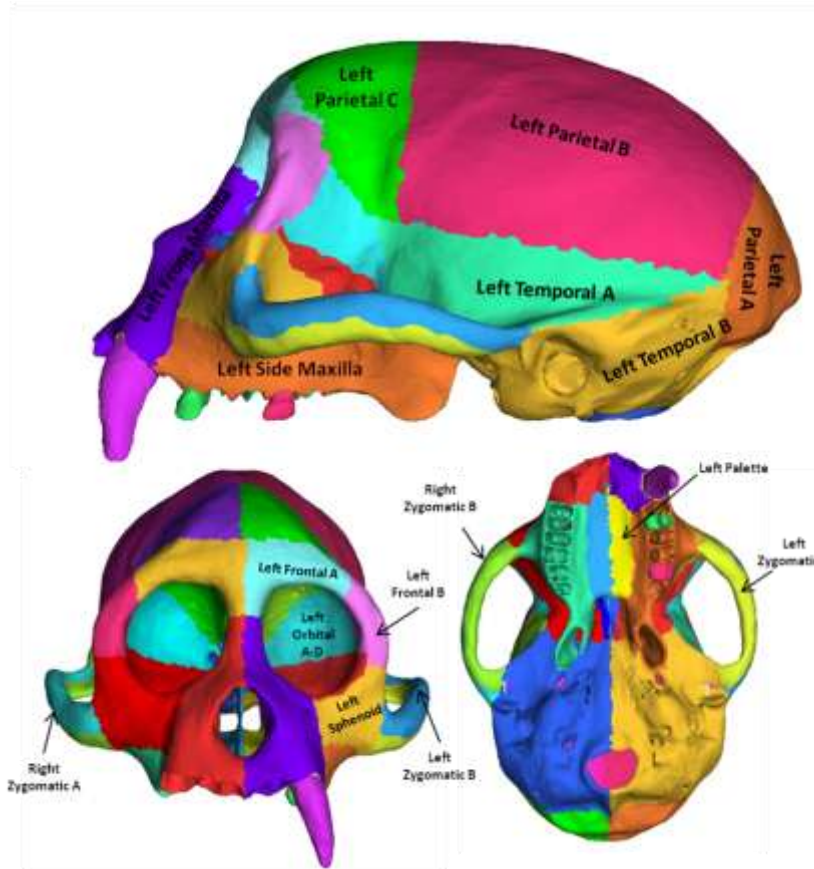
Figure 14: Anatomical Regions Segmented in Strand7

Table 5: Curly Orthotropic Material Property and Orientation data

Region	Site	Angle	E1	E2	E3	v12	v23	v13	G12	G23	G13
Parietal	1	149	4.575	6.627	12.144	0.5	0.407	0.055	2.11	3.881	2.41
Frontal	8	125.7	5.16	6.982	7.328	0.321	0.360	0.453	1.81	2.616	2.187
Temporal	9	35.4	8.534	14.612	14.624	0.42	0.262	0.332	2.764	5.813	2.468
Zygomatic	11	166	9.968	13.08	21.033	0.309	0.135	0.182	3.573	7.074	3.232
FMaxilla	17	110.7	8.029	7.871	13.586	0.5	0.313	0.302	2.617	3.99	3.272
SMaxilla	20	122	6.251	10.451	13.252	0.488	0.365	0.176	2.443	4.66	2.323
Orbital	25	85.3	7.263	10.428	12.749	0.345	0.342	0.436	2.435	4.124	2.903
Palette	27	140	9.894	10.391	17.244	0.5	0.302	0.335	2.969	5.328	3.757
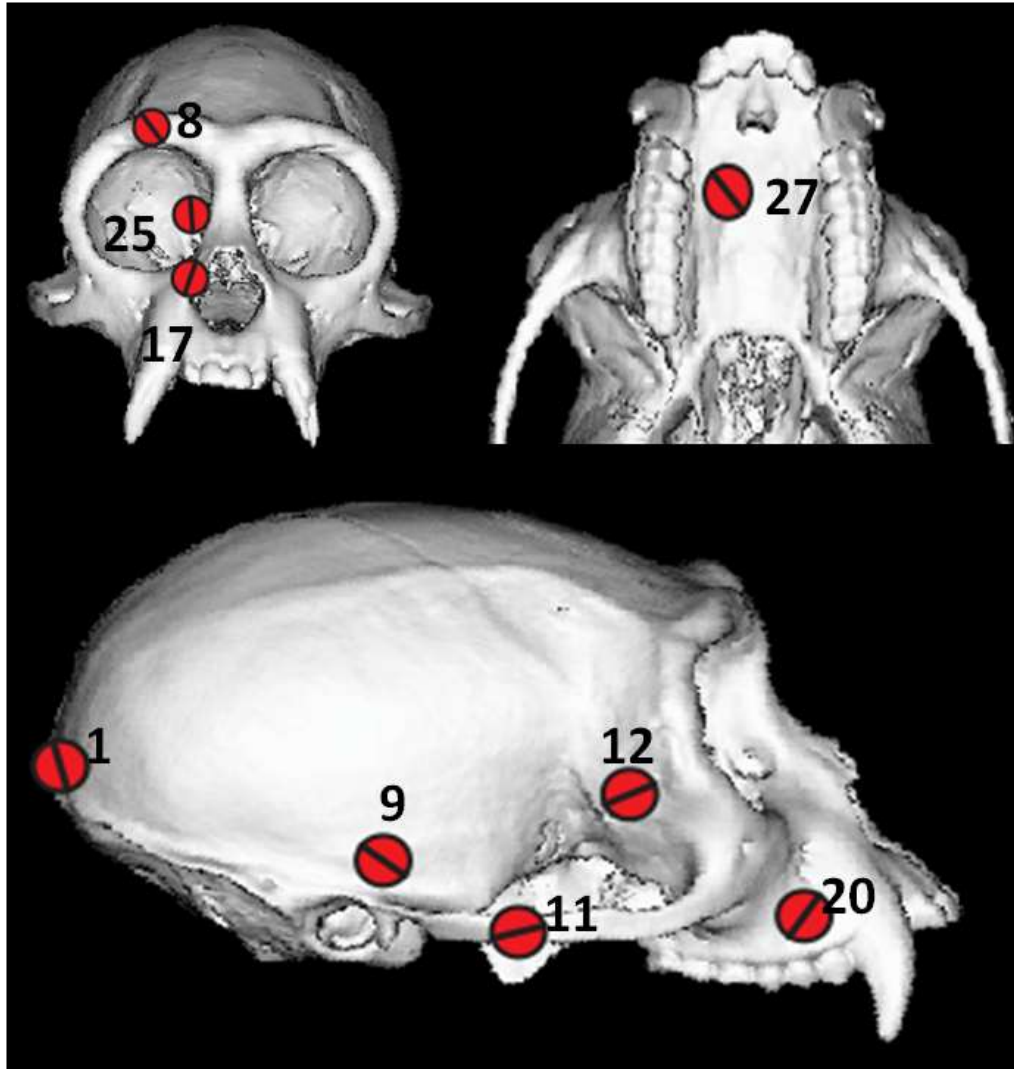
Figure 15 : Typical sample regions preformed in Professor Dechow's Lab

Once the 32 groups were defined the model was exported as a .cdb file in order to be compatible with ANSYS 14.0. The model was exported in Strand7 using a Blocked ANSYS CDB format due to the size of the model. The units assigned were consistent with the Strand7 model. The transfer between STRAND7 and ANSYS required some manual edits in the .cdb file using a text editor (Notepad). First of all, the bricks (solid elements) are automatically exported as SOLID62 elements. This element type is not supported by ANSYS so these elements were converted into SOLID185 elements. In

addition, the shell/plate elements were automatically assigned SHELL72 properties, so the plate elements were converted into SHELL181 elements. The last few lines of code listed the nodal forces and then deleted them all. This segment of code was eliminated to allow for a proper transfer of surface loads into ANSYS. Once edited, the .cdb file was read into ANSYS APDL using the 'read input from' command. The plates from the muscle force attachments were imported into ANSYS as one component, 'NASTRAN_IMPORT___COMBINED_NASTRA'. This component and the elements/nodes defining it were deleted using the CMSEL→CMDELE and ESLE, all → EDELE commands. Muscle force attachments were zipped to the underlying nodes on the solid brick elements and then defined as thin-membranes with a thickness of 1.0E-5 mm. This allowed the nodal force vectors to be directly applied to the solid elements of the ANSYS model. The particular region naming convention in ANSYS APDL defined all major groups and subgroups as components. In order to avoid confusion later on, the major regions (now categorized as components) and elements defining each major region were deleted using the same commands defined above. This completes the transfer of *Curly's* 32 region segmented crania from Strand7 to ANSYS APDL.

Unpublished specimen specific orthotropic material property and orientation data from Professor Paul Dechow's lab (Personal Correspondence) was used to define each anatomical region. The mean material property and orientation data for *Curly* are displayed in Table 5. An error occurred when assigning orthotropic material properties to the Sphenoid region. The data achieved through in-vitro sampling methods at Paul Dechow's lab (Personal Correspondence) did not result in a positive definite stress-strain matrix for this region. A positive definite stress-strain matrix is required for all real

materials. For an orthotropic material Equation (7) is a necessary but not sufficient condition for positive definiteness, and the values of elastic moduli and Poisson ratio for the Sphenoid region violated this condition.

$$1.0 - N_{12}^2\left(\frac{E_2}{E_1}\right) - N_{23}^2\left(\frac{E_3}{E_2}\right) - N_{13}^2\left(\frac{E_3}{E_1}\right) - 2(N_{12}^2 N_{23}^2 N_{31}^2)\left(\frac{E_3}{E_1}\right) > 0$$

(7)

where ν_{ij} is Poisson ratio for the i-j plane. In order to achieve a positive definite stress-strain matrix for the Sphenoid region, values within the lower and upper bounds for this data were investigated. The standard deviations that will be used in this study are taken from a population of *Cebus* skulls (n=5). It is important to state that we are assuming that the geometry of an individual does not influence the material property orientation. Furthermore it is assumed that the material property orientation of the skull is not developmentally driven but rather evolutionary driven. The population standard deviations are displayed in (Table 6). There were no recorded orthotropic material properties and orientations for trabecular bone, the septum, periodontal ligaments, and tooth enamel. Thus we decided to use isotropic material properties cited in ((Wood, S. A., et al., 2011)) shown in Table 1. Eight orthotropic material properties and four isotropic material properties were defined in the Material Property Directory of ANSYS APDL. In order to assign the proper material properties to anatomical location, the component (region) was selected using 'CMSEL' and then the material property number was changed using 'MPCHG' and the corresponding new material property number.

Table 6 : *Cebus* Population Standard Deviations (n=3-5 samples)

Site	Θ (°)	E12	E31	E23	V12	V31	V23	G12	G31	G23
1	77	4.08	4.69	4.29	0.2129	0.0776	0.1388	1.996	2.27	2.092
8	15	3.08	4.26	5.30	0.0671	0.0799	0.0374	1.065	0.896	1.672
9	26	1.105	2.33	2.79	0.0391	0.0412	0.0337	0.307	0.428	0.543
11	19	1.080	3.26	1.45	0.1018	0.00566	0.1361	0.453	0.631	1.359
17	10	2.34	4.35	2.48	0.1129	0.0873	0.0284	1.002	0.358	1.201
20	9	2.54	4.86	1.538	0.0986	0.1662	0.0208	0.730	0.660	0.894
23/25	13	0.676	4.15	2.92	0.0689	0.00742	0.0537	0.214	0.385	1.77
27	32	1.021	1.76	2.38	0.01561	0.0235	0.0242	0.299	0.680	0.806

The main goal of this study was to investigate how the maximum principal strain orientation alters with respect to a region's (and other region's) material stiffness orientation. In order to achieve parameterized orientations of principal material directions, two local coordinate systems were assigned to each anatomical region. The first local coordinate system (fixed CS) for every anatomical region was created using the 'CLocal, KCN, KCS, XL, YL, ZL, THXY, THYZ, THZX, PAR1, PAR2' command. This command was chosen over the numerous other Local Coordinate System commands because it creates a local coordinate system with respect to the active coordinate system. The fixed coordinate system is given a reference number (KCN = #) and assigned a Cartesian coordinate system type (KCS = 0). The origin is defined from a desired sample node coordinates (XL, YL, ZL) and the rotation (THXY, THYZ, THZX) of the fixed CS is such that the z-axis is normal the surface of the skull. The first time the fixed coordinate systems were assigned to each anatomical region the Graphical User Interface

(GUI) was used to achieve the origin coordinates and the rotation angles in a visual pleasing manner. This was done by selecting Workplane→Local Coordinate System→Create Local CS→By 3 Nodes, and then the values for each defined CS were exported using the CSLIST command. Selecting three surface nodes was rather difficult due to the fact that ANSYS only has a 'through-selecting' method. In order to avoid selecting a central node (rather than a surface node) only *exterior* nodes of a named component were generated using the 'NSEL, s, *EXT*, component name' command (Figure 16.A vs B). Once only the surface nodes were selected, the elements and nodes of a given component were plotted using GPLOT command. The outline of the surface elements and nodal intersections made for an easier time selecting the surface nodes. Finally the local coordinate system was created using the 'By 3 Nodes' method; node (1) defined the origin of the LCS, node (2) defined the direction of the x-axis, and node (3) defines the x-y plane (Figure 16.C). For each anatomical region it is important to make sure the z-axis (blue arrow) in the direction of outward normal (Figure 16.D). In order to apply a component's local coordinate system to all elements in that component (anatomical region) a component of interest was selected 'CMSEL,S, component name'. Then the working plane was assigned to the origin of the activated coordinate system ('wpave, 0, 0, 0'). Next, all the nodes attached to the elements of that component were selected('nsle, s'). Finally the CS of each element was modified to that of the activated CS ('emodif, all, esys, #'). The batch code we used to assign each coordinate system automatically assigned one anatomical region after another. In between assigning coordinate systems to each anatomical region, the activated coordinate system needs to be brought back to the Global CS ('CSys, 0; wpave, 0, 0, 0'.) This ensures that the

origins and rotations will be defined for each anatomical region with respect to the Global CS.
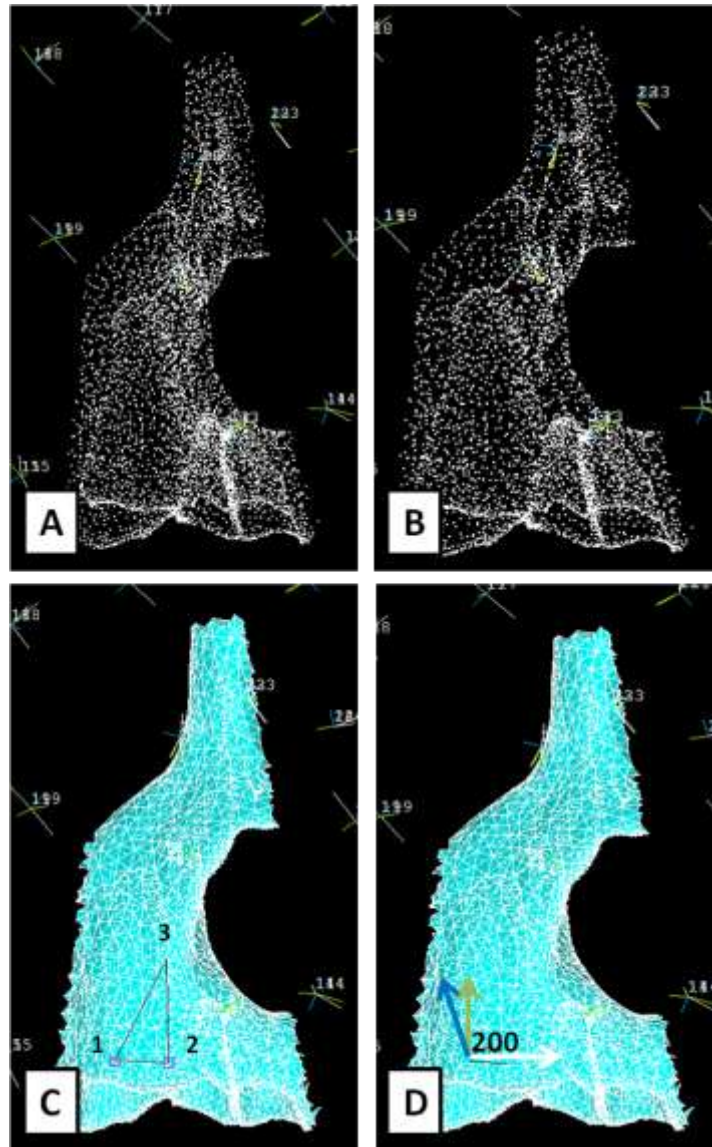
Figure 16 : Defining Local CS 200 (A) All nodes (B) Exterior nodes (C) Select 3 nodes (D) CS

The second local coordinate system (rotating-CS) was assigned to parameterize the orthotropic material property orientation at each anatomical region. These rotating-CS for each anatomical region, were created at the same origin as the corresponding fixed-CS. In order to ensure the same orientation (prior to rotation) the fixed-CS of the

45

anatomical region of interest was set as the active coordinate system using the 'CSYS, #' and 'WPAVE,0,0,0' commands. Defining the rotating-CS is similar to the process of the fixed-CS. However, now since the fixed-CS is the active coordinate system the origin of the rotating-CS will be (0, 0, 0). The only rotation we were concerned about was about the z-axis. A Cartesian (0) coordinate system was defined with a label (*100+fixed-CS*) using the 'CLOCAL, *111*, 0, 0, 0, 0, θ_z, 0, 0' command for each anatomical region. The variable θ_z was created to relate the fixed-CS $(X, Y)_f$ or $(XY_f$ plane) to the rotating-CS $(X, Y)_r$ or $(XY_r$ plane) by a rotation angle θ_z about the constant z-axis (Figure 17).
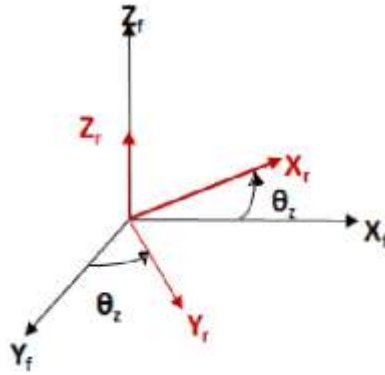
Figure 17: Rotation axes $(X,Y)_r$ are relative to Fixed axes $(X,Y)_f$ by angle of rotation θ_z

In this way the orientation of the rotating-CS was parameterized, and the rotating-CS corresponds to the material stiffness orientation axes. The x-axis of the rotating-CS was assigned the mean maximum material stiffness (E_3), defining the orientation of orthotropic material in that particular anatomical region. Each anatomical region had a different rotation angle defined in Figure 18. We were able to use eight input variable angles (θ_z) and then define the rest of the 25 angles based upon these. Some anatomical regions with significant surface curvature were subdivided into multiple material volumes so that unique orientations of principal material directions could be assigned to each sub-volume based on our rotating coordinate systems. The rotating CS for each of the

46

divided sections can be related to the original input variable easily through transformations. The anatomical regions on the left side of the skull were defined using a mirroring technique. As described above, the coordinate system of each element making up the component of interest (anatomical region) needs to be adjusted using the EMODIF and ESYS commands.

theta_	RFMAXILLA	=	20		
theta_	LFMAXILLA	=	180-	theta_	RFMAXILLA
theta_	RPALETTE	=	50		
theta_	LPALETTE	=	180-	theta_	RPALETTE
theta_	RSMAXILLA	=	122		
theta_	LSMAXILLA	=	180-	theta_	RSMAXILLA
theta_	RORBITALA	=	85.3		
theta_	RORBITALD	=	90+	theta_	RORBITALA
theta_	RORBITALB	=	theta_	RORBITALD	
theta_	RORBITALC	=	theta_	RORBITALA	
theta_	LORBITALD	=	180-	theta_	RORBITALD
theta_	LORBITALA	=	180-	theta_	RORBITALA
theta_	LORBITALC	=	180-	theta_	RORBITALB
theta_	LORBITALB	=	180-	theta_	RORBITALC
theta_	RPARIETALA	=	59		
theta_	RPARIETALB	=	theta_	RPARIETALA	
theta_	RPARIETALC	=	theta_	RPARIETALA	
theta_	LPARIETALA	=	90-	theta_	RPARIETALA
theta_	LPARIETALB	=	90-	theta_	RPARIETALA
theta_	LPARIETALC	=	90-	theta_	RPARIETALA
theta_	RFRONTALB	=	35.7		
theta_	RFRONTALA	=	theta_	RFRONTALB	
theta_	LFRONTALB	=	180-	theta_	RFRONTALB
theta_	LFRONTALA	=	180-	theta_	RFRONTALB
theta_	RTEMPORALA	=	35.4		
theta_	RTEMPORALB	=	theta_	RTEMPORALA	
theta_	LTEMPORALA	=	180-	theta_	RTEMPORALA
theta_	LTEMPORALB	=	180-	theta_	RTEMPORALA
theta_	LZYGOMATICB	=	26		
theta_	LZYGOMATICA	=	theta_	LZYGOMATICB	
theta_	RZYGOMATICA	=	90+	theta_	LZYGOMATICB
theta_	RZYGOMATICB	=	90+	theta_	LZYGOMATICB

Figure 18: Relationship for rotation angles (highlighted=input variables)

It is important to point out that the rotation angles defined in Figure 18 do not necessarily correspond with Dechow's material orientations displayed in Table 5. This is

because the fixed-coordinate systems were not all setup with the x-axis (θ_z) clockwise to the maximum stiffness axis (rotating-CS). It was impossible to have the coordinate systems on the left side always mirror the right side with respect to the x and y axes because the z-axis needed to remain outward normal from the surface. Depending on the fixed-CS setup the maximum stiffness axes (rotating-CS) may be counterclockwise or clockwise to the x-axis or y-axis of the fixed-CS (Figure 19).
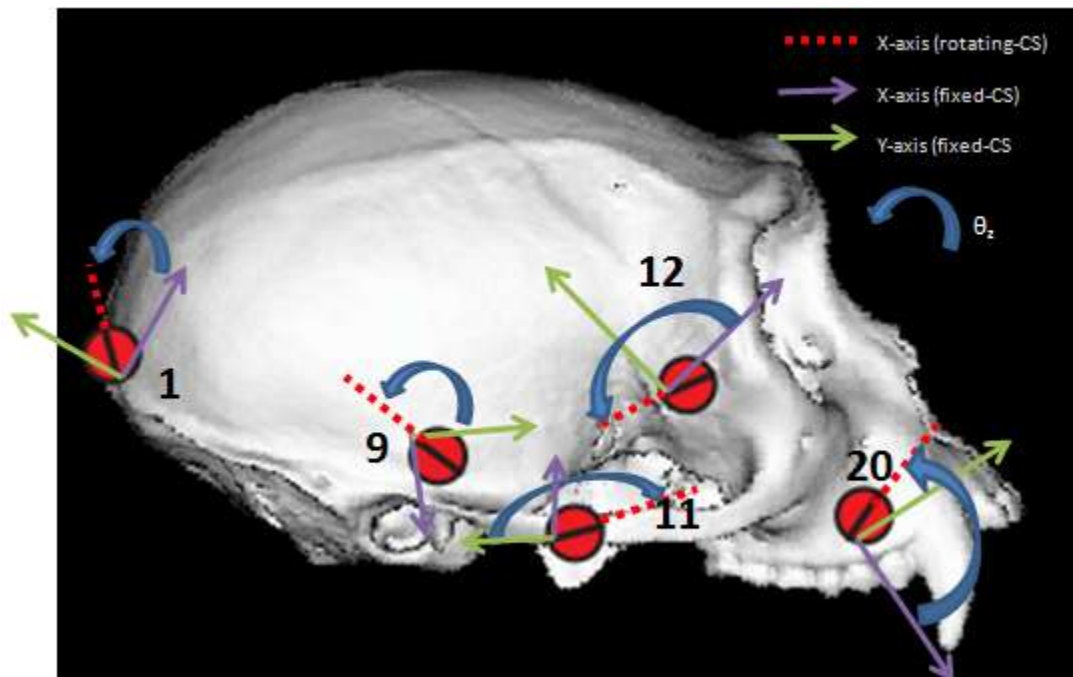
Figure 19: Orientation of Maximum Stiffness with respect to fixed-CS

As shown above coordinate systems 1, 12, and 20 have θ_z located counter clockwise from the x-axis (purple arrow). While, coordinate system 9 defines θ_z counter clockwise from the y-axis (green arrow). Finally coordinate system 11 defines θ_z clockwise from the y-axis. In **Error! Reference source not found.** there is a chart that gives each anatomical region and the relation of the rotating-CS to the fixed-CS (θ_z) with respect to the x-axis and y-axis using counterclockwise and clockwise angles. In

addition, **Error! Reference source not found.** contains a complete diagram of each anatomical region and relation of the fixed-CS to the mean rotating-CS to examine these labeling variations. The experimental setup we used defined a positive θ_z as rotating the x-axis of the rotating-CS counterclockwise from the x-axis of the fixed-CS. This is consistent throughout Figure 18; special care was taken when examining results with respect to these variations.

We investigated the relationship between the maximum strain orientations and randomness in stiffness orientations of material properties. Note that the effect of uncertainty in values of material properties defining orthotropic and isotropic material behavior has already been investigated by (Berthaume, M., et al., 2012*). To do this we used the Probabilistic Design module in ANSYS APDL. In a probabilistic approach the uncertainties in input variables are described using statistical distribution functions (Theory Reference for the Mechanical APDL and Mechanical Applications, 2009). Three components are required when using Probabilistic Design Modeling: a macro-code to drive ANSYS, list of input variables, and a list of output parameters. The macro code automatically executes multiple separate finite element analyses, with each analysis consisting of a unique set of input variable values obtained using a Truncated Gaussian (Normal) Distribution. The number of times the macro code is executed, N, is defined at the start and depends on the amount of random input variables. For an individual set of input variables, a deterministic simulation is run resulting in designated output parameters. The macro-code that was used in this study was based upon code used by (Berthaume, M., et al., 2010) in the Orthotropic Material section of their research. The random input values were determined using a Monte Carlo simulation with Latin

hypercube sampling. These techniques allow for a lower number of simulations to be run, saving computational time, while still obtaining an accurate statistical distribution. Monte Carlo simulation with Latin hypercube sampling is the most suitable probabilistic method for benchmarking and validation purposes (ANSYS Mechanical APDL Advanced Analysis Techniques Guide, 2011). Latin hypercube sampling uses a form of 'memory' to avoid the clustering of sample points. For more information on Latin hypercube sampling in a Monte Carlo simulation please see (Olsson, A., et al., 2002). The number of simulation loops required for a Monte Carlo simulation can only be determined by investigating the amount of scatter presented by the output parameters and the type of results expected to come from the analysis (ANSYS Mechanical APDL Advanced Analysis Techniques Guide, 2011). Some sources say that an appropriate number of simulations can be determined by subtractive one from the number of input variables (n-1)(ANSYS Mechanical APDL Advanced Analysis Techniques Guide, 2011). Since we were only working with eight true input variables we decided that a sample size of eight was too small. Since there were an additional 25 dependent variables based upon the input variables, we considered using a value of 31 (n-1=32-1). In order to make sure 30 simulations (rounding down from 33) were a proper amount we ran a small convergence study. Three probabilistic design experiments were executed, (1) 30 simulations, (2) 50 simulations, and (3) 100 simulations. Based upon the results of this convergence study we decided using 50 Monte Carlo simulations would provide results of sufficient accuracy while still minimizing computer time and memory usage.

When defining random input variables a statistical distribution is required. In our case we used the Truncated Gaussian distribution (Figure 20). for the orientations of principal material directions. The input variables we applied randomization to were the

angles of rotation θ_z of the rotating-CS around the fixed-CS highlighted in Figure 18. The Truncated Gaussian requires lower and upper bounds to run; we defined these using the mean θ_z (Table 5) and *Cebus* population standard deviations (Table 6) for each anatomical region. This allowed us to limit the rotation, θ_z, from $\pm$ three standard deviations with respect to the mean θ_z for each anatomical region (or from zero to 179.99 degrees if $\pm$ three standard deviations exceeded 180 degrees). In order to define input variables versus output variables special attention was needed when using the 'PDVAR' command. The 'PDVAR, name' command is followed by the name for which the input variable or output parameter is defined. The next part of the PDVAR command is the shorthand for the chosen statistical distribution, so in our case 'TGAU'. Finally the mean, standard deviation, lower bound, and upper bound were entered into the command 'PDVAR, RFMAXILLA_Ex, TGAU, Mean, SD, LB, UB' for each anatomical region (See APPENDIX B

CUSTOM WRITTEN C).

When defining output parameters the shorthand for response 'RESP' was used in the third command field after defining the name of the output parameter. The designated output parameters were the normal (x,y) and transverse (xy) strain components (ε_x, ε_y, and γ_{xy}), exported from nodal solutions at each of the 32 anatomical regions of the cranium. These output parameters were exported with respect to the fixed-CS. A visual interpretation of the Probabilistic Design method is outlined in (Figure 21). Note that the starting point in this chart is when the FE model is imported into ANSYS; however much work was done prior in Strand7 to segment the skull. The ending point in the chart is defined as post processing, discussed in greater detail below.

Once the data for each simulation was saved in a PDRS file, the data was imported as a delimitated text document into Microsoft Excel. From here we used Microsoft Excel functions to calculate the maximum, minimum, and shear principal strains along with the orientation of the maximum principal strain axis. Equations similar (3) to (4) and were used to calculate the principal maximum, minimum, and shear strains. An adjusted version of Equation (4), displayed below (8), was used to acquire the orientation of maximum principal strain (θ_P).
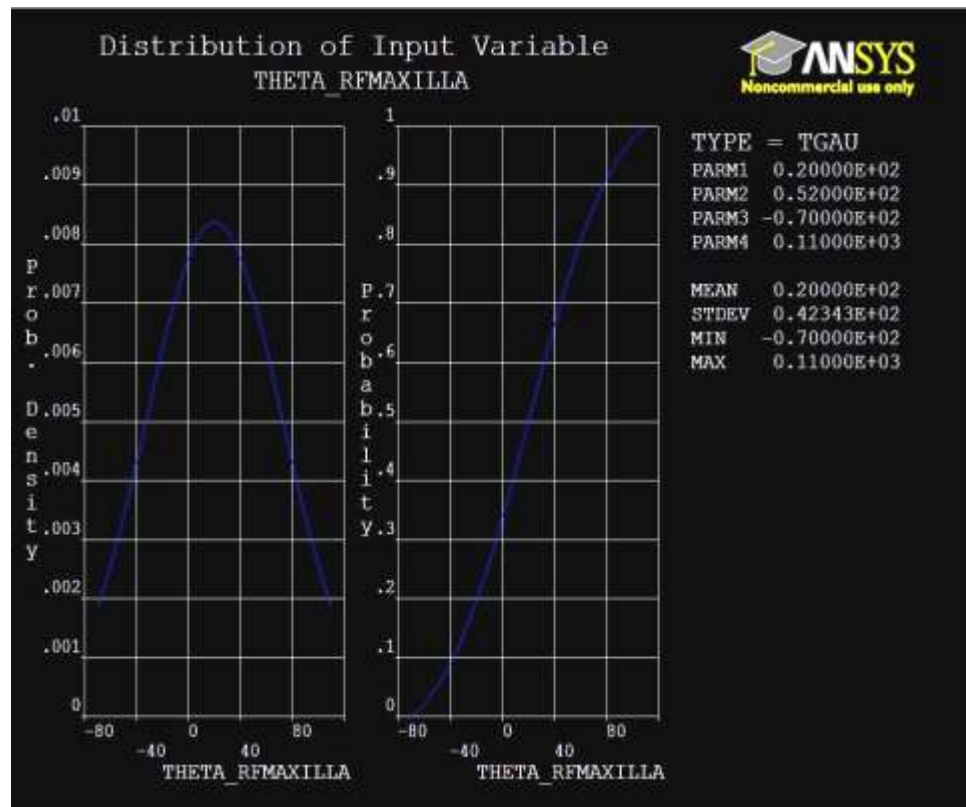
Figure 20 : Truncated Gaussian Distribution for RFMaxilla
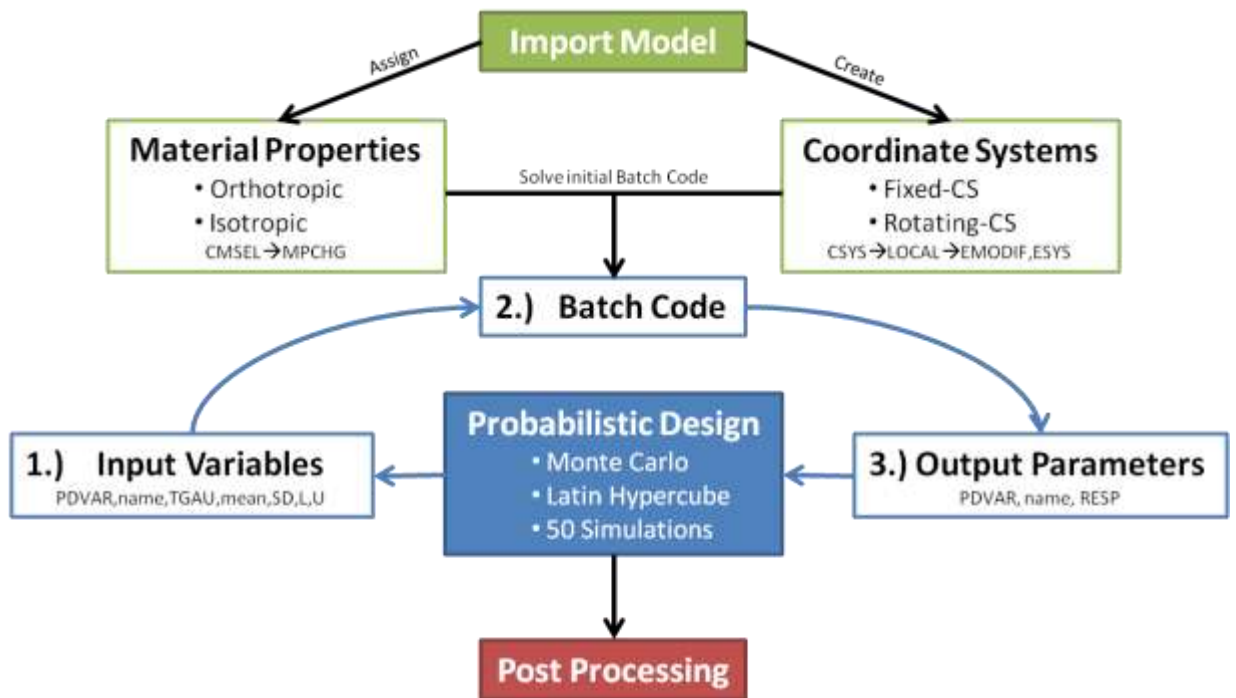
Figure 21 : Flow chart of ANSYS Probabilistic Design Method

$$\theta_P = \tan^{-1}\left(\frac{\gamma_{xy}}{\varepsilon_x - \varepsilon_y}\right)/2 = degrees\left(\frac{atan2\big((\varepsilon_x - \varepsilon_y), \gamma_{xy}\big)}{2}\right)$$

(8)

The 'atan2' function in Excel requires and input of x- and y- coordinates. As shown in Figure 22 the (x, y) coordinates that are used to determine the orientation of maximum principal strain (θ_P) with respect to the x-axis are (ε_x- ε_y, γ_{xy}). Since we defined all of the rotation angles (θ_z) with respect to the x-axis it was important to also define the orientation of maximum principal strain (θ_P) with respect to the x-axis. The original output of the 'atan2' function is in radians so we converted this value to degrees in order to make a comparison between the rotation angles (θ_z). A positive output angle is in the clockwise direction, and a negative output angle is in the counterclockwise

53

direction with respect to the positive x-axis. In order to make a comparison between θ_P and θ_z the maximum principal strain orientation needed the same sign configuration so θ_P was multiple by (-1). Since the maximum principal strain orientation angle ranged from 180 to -179.99 degrees it was easy to determine which quadrant the axis was in Figure 23. Depending on the anatomical region and the fixed-CS setup it was sometimes necessary to perform simple transformations to ensure the proper comparison between maximum principal strain orientations (θ_P) and the rotating-CS orientation (θ_z).
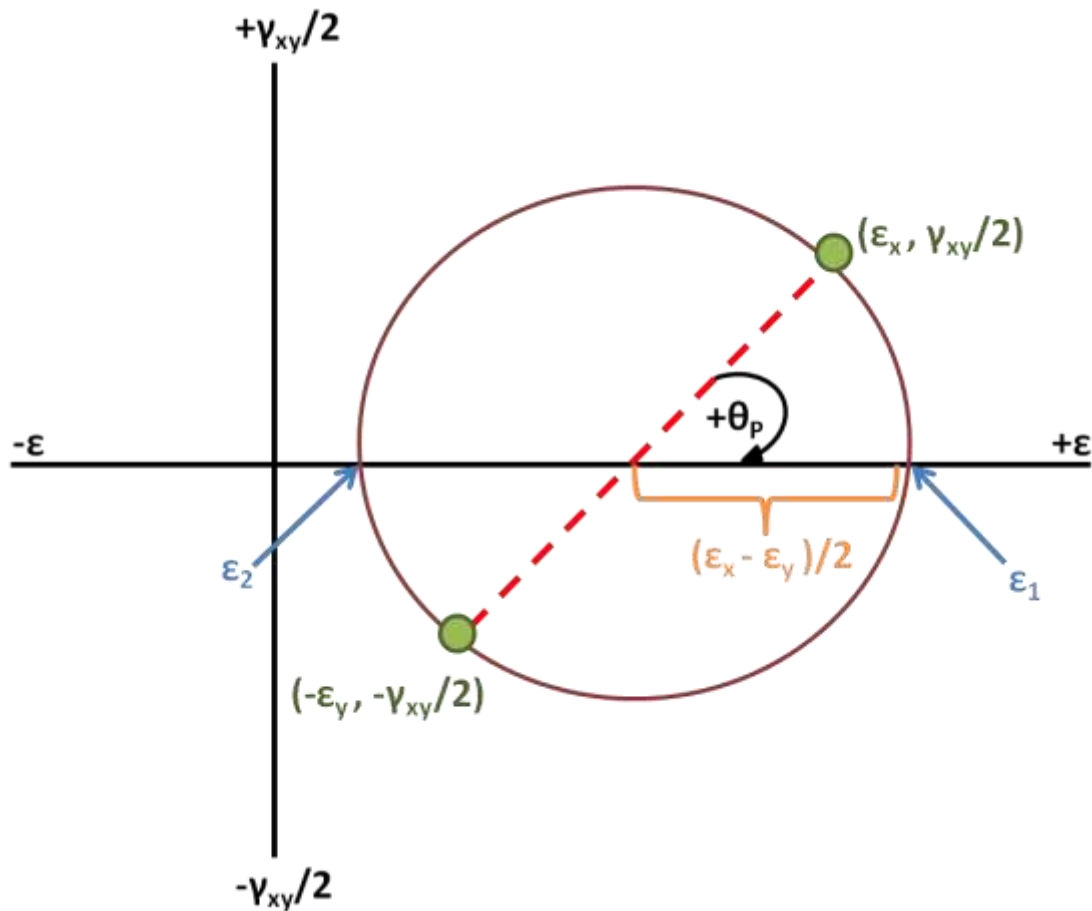
Figure 22 : Mohr's Circle configuration
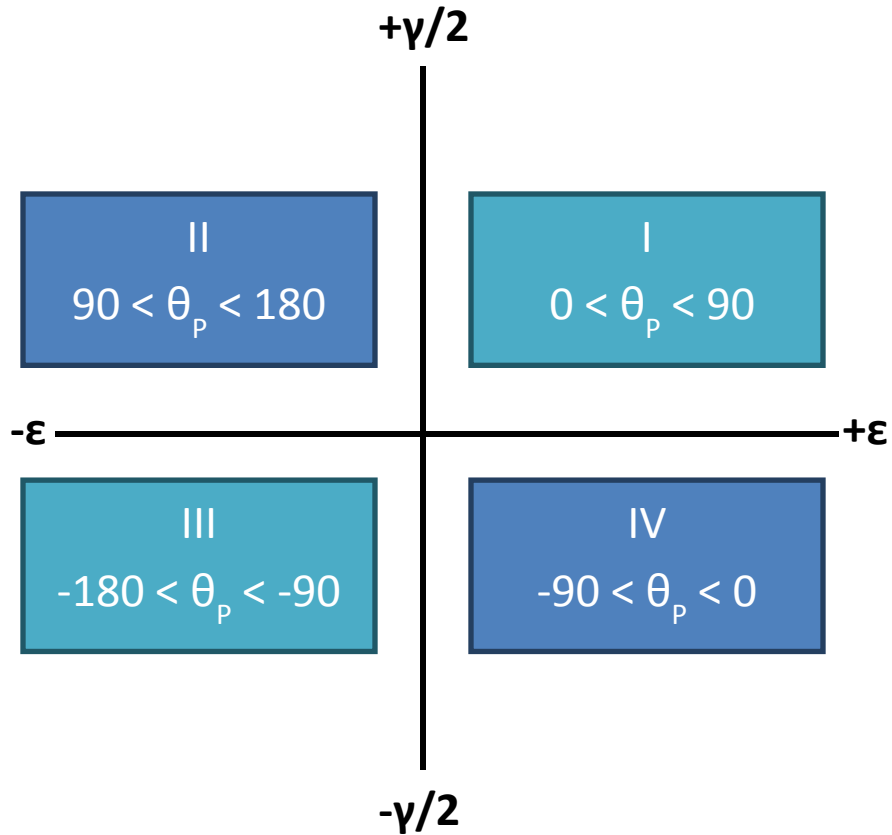
Figure 23: Quadrants

The Trend and Statistic post processing methods available in ANSYS APDL were not used for the purpose of this experiment. Instead we imported the data from the Probabilistic Design simulations into Microsoft Excel as delimited text. Then using different logarithms and correlation coefficient methods we were able to make accurate comparisons of the maximum stiffness orientation and maximum principal strain orientation in various cranial-facial regions. A correlation matrix was constructed to investigate the statistical correlation coefficients between individual input variables and output parameters of the Probabilistic Design method. This 32 x 32 matrix compared the orientation of maximum material stiffness of each anatomical region to the orientation of maximum principal strain of each anatomical region. This allowed for a comparison

within a certain anatomical region, along with comparisons across anatomical regions. Once constructed, the matrix was a bit overwhelming to look at and determine which anatomically regions are significantly correlated. A second 32 x 32 matrix was constructed and if there was a correlation that was significant the cell was filled with the correlation coefficient value and if there was not a significant correlation the cell was filled with '0'. This allowed for the significant correlations to be easily recognized. In order to figure out which correlation values were significant a "Critical Values of the Pearson Product-Moment Correlation Coefficient" Table was investigated. Our degree of freedom was 48 (n-2) for our 50 simulation trial, and we chose a level of significant (p) for a two-tailed test of 0.05 based on past research (Berthaume, M., et al., 2012*). A p-value of 0.280 was achieved using this table; thus any correlation above 0.280 indicated significance. All in all, this correlation matrix allows for the relationship between orientation of maximum principal strains in anatomical regions of the cranium and orientations of orthotropic material properties to be investigated, addressing the first hypothesis. In addition, the correlation matrix contains the correlation coefficients between input variables which can be used to devise a way of further simplifying the division of the skull into anatomical regions. If a high correlation exists between two adjoining areas of the skull, potentially a design parameter can be defined relating these regions. Thus, one of the correlated probabilistic design input variables can be eliminated further reducing computational time.

The second hypothesis was addressed by using a makeshift design optimization method. The main goal of this section was to find out if the material property stiffness orientations are such that the work expended by mastication is minimized. The objective

56

function we were minimizing was the total elastic strain energy of all the elements in the model. In order to extract the elastic strain energy from every element in the model and sum it up the ETable and SSUM functions were used. Once the model was solved the post processing command 'ETable, SE, SENE' was used to define a new scalar parameter "SE" which stands for elastic strain energy for every element in the model. Finally a new scalar parameter "StrainE" was defined using the '*Get, StrainE, SSUM,,ITEM,SE' command. This command takes the last SSUM output which was achieved by summing up the item "SE" and defines the solution as a new scalar parameter. Instead of running a separate Design Optimization file, we implemented 'Strain Energy' as an additional output parameter in the 50 trial Probabilistic Design.

CHAPTER 4

RESULTS: STUDY 1

A validation of a specimen specific model has yet to be done using *in vivo* feeding biomechanic data. The main goal of Study 1 is to validate a specimen specific model through use of specimen specific EMG signals, PCSA, material property, and principal strain data achieved through *in vivo* and *in vitro* methods. This section provides the *in silico* results from four permutations (Models A-D) of the isotropic finite element model of the specimen, *Curly.* In addition, the results from the orthotropic finite element Model A are also provided. Two sampling techniques, outlined in the Methods section, were used to extract the strain data at each strain gage location (right zygomatic arch, left anterior pillar, and right anterior pillar).

4.1 Isotropic Validation

The four models (A-D) were run with EMG-derived muscle loads simulating a left premolar chew of a Brazil nut. These models assess the differences in various modeling techniques, specifically the importance of key features in the maxilla region. The amount of detail necessary when modeling the maxilla region of the cranium depends on the location researchers are looking at when extracting results. As shown in the von Mises contour plots comparing the models (Figure 24 and Figure 26), there is little change in the overall stress distribution. This is especially true towards the back of the skull in the parietal and temporal regions. With respect to the alveolar process region, the stress distributions hardly change on the balancing side (right images in Figure 24). The same is true for the maximum principal strain vectors throughout the skull (Figure 25

and Figure 27).   However, there are obvious differences on the working side, above the left canine in the rostrum region and above the loaded premolar tooth when comparing empty sockets, capped off sockets, and fully modeled teeth.

Model B and D display the pronounced change in stress distribution in the left rostrum region. The left upper canine is modeled realistically using tooth enamel and elastic PDL properties in Model B, while in Model D the LUC is modeled using cortical bone. There is a 50-80% decrease in von Mises stress directly above the LUC when using improper material properties for the tooth and corresponding PDL. Comparing Model A (empty sockets) and Model B (teeth fused to sockets and modeled as cortical bone) artificially stiffens the local alveolus region but did not have affect the model globally, agreeing with (Wood, S. A., et al., 2011) findings. The differences between Model D (teeth fused as cortical bone) and Model C (simply capped off at gum line) prove to be insignificant. There are only minute changes in local stress distributions on the working alveolar region as well as the balancing side and the rest of the cranium. One main focus was to investigate the stress distribution around the loaded tooth. The results show that when the adjacent teeth are not modeled (Model A) there are higher stresses in the region of the working tooth. A 200-300% stress increase exists in the regions directly surrounding the tooth that comes in contact with the hard food item. However, when the adjacent teeth are filled and constructed to different extents (Models B-D) these elevated stresses subside.
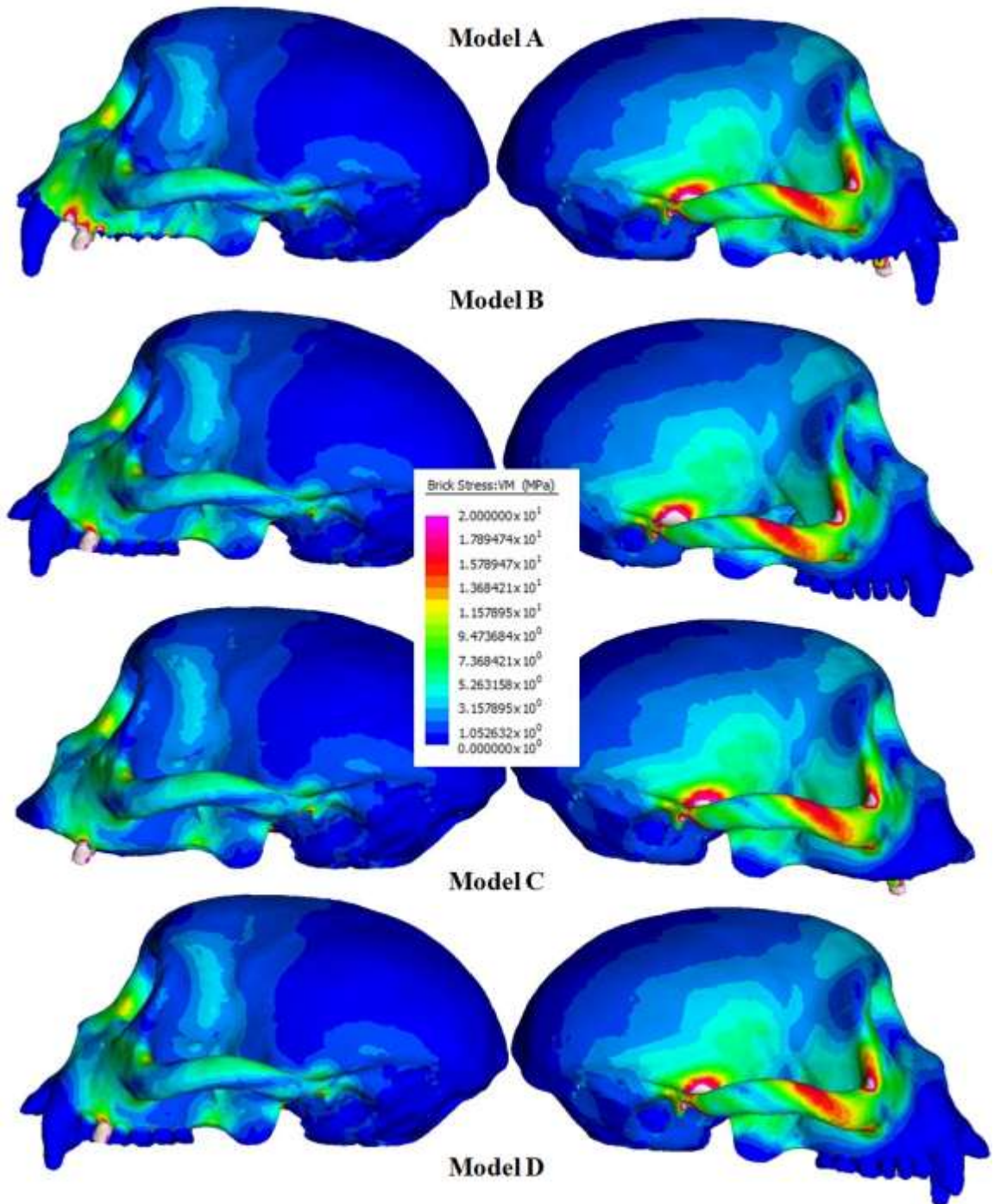
Figure 24: Von Mises Stress results for Models A-D, side view
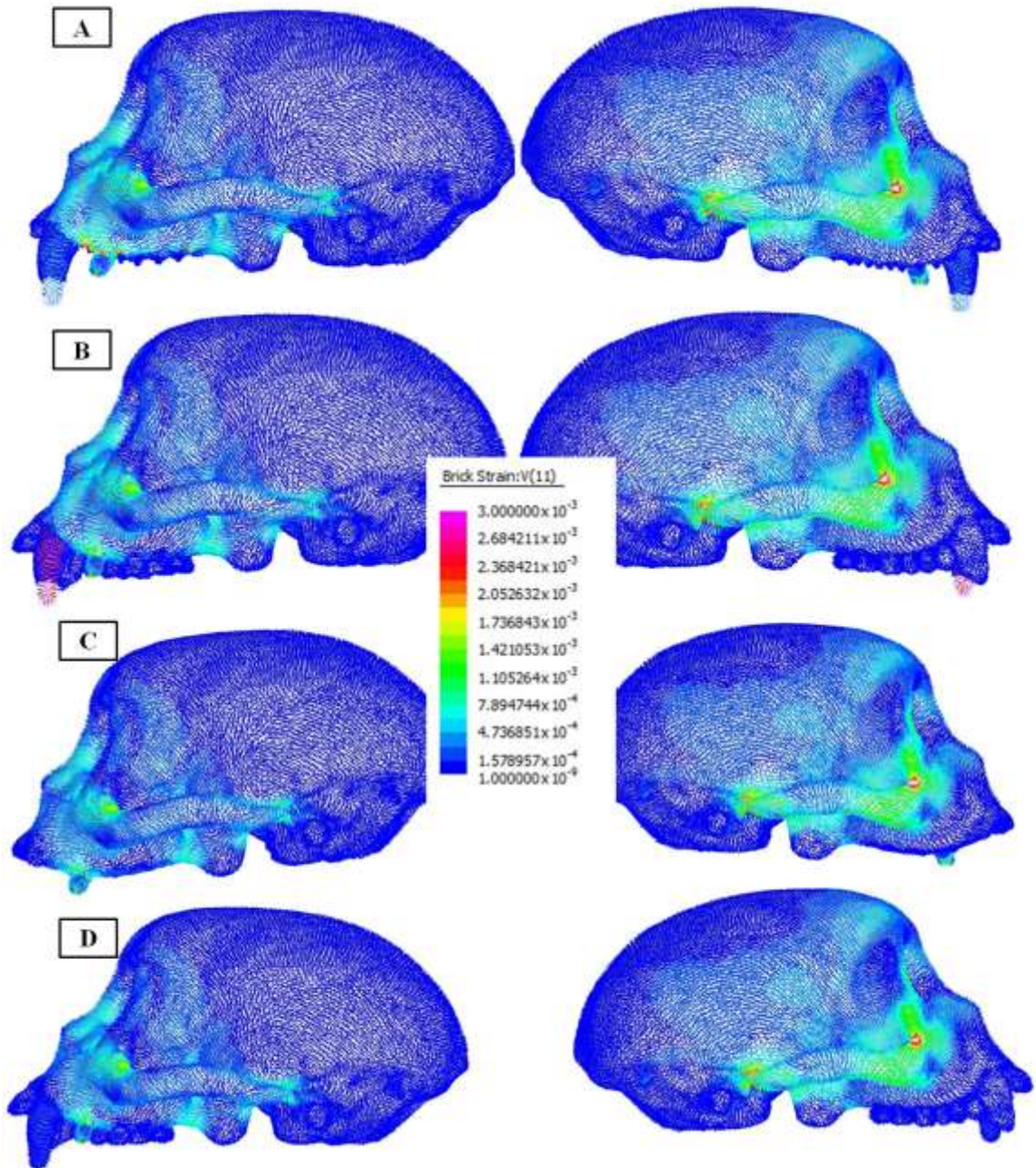
Figure 25: Max principal (11) Strain results for Models A-D, side view
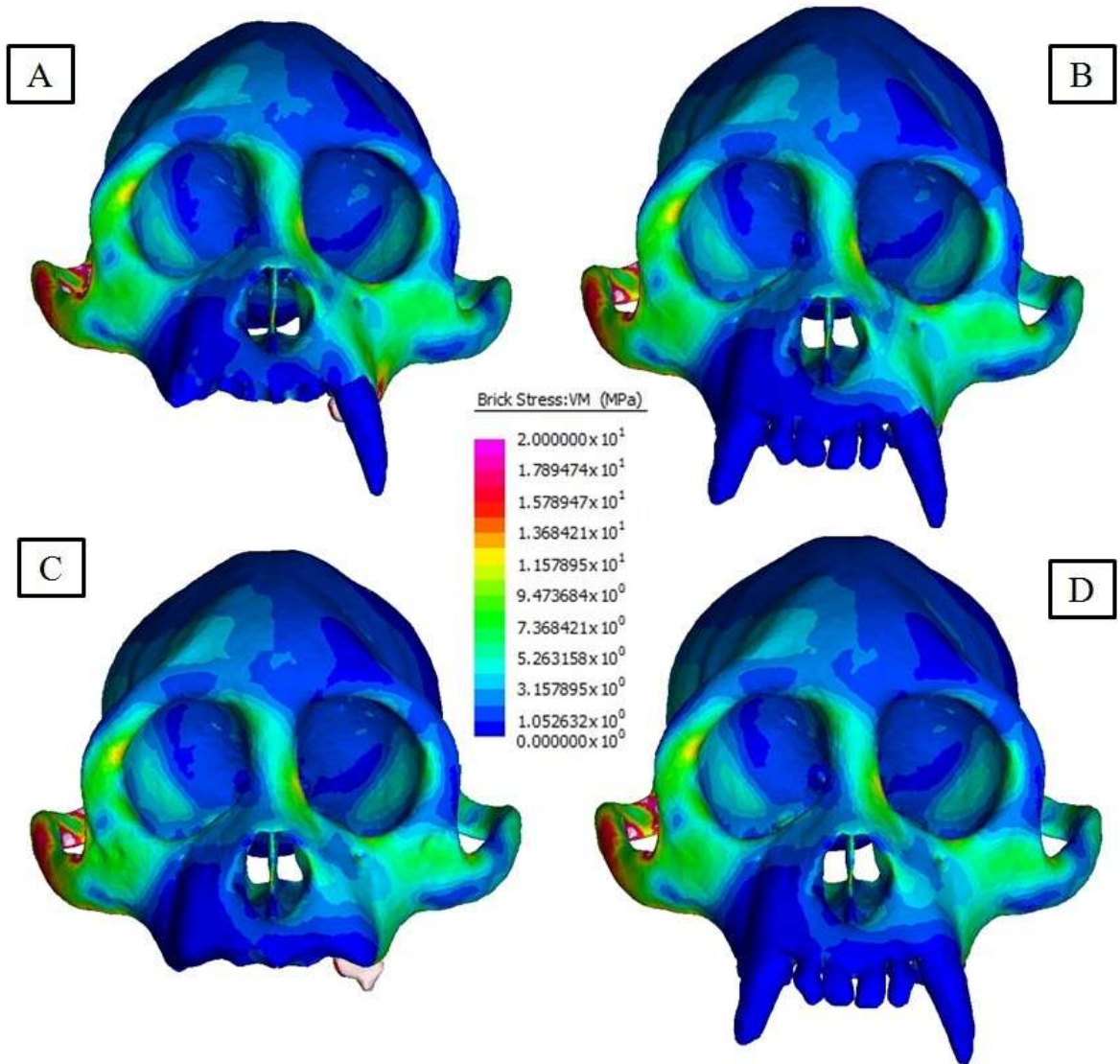
Figure 26: Von Mises Stress results for Models A-D, front view
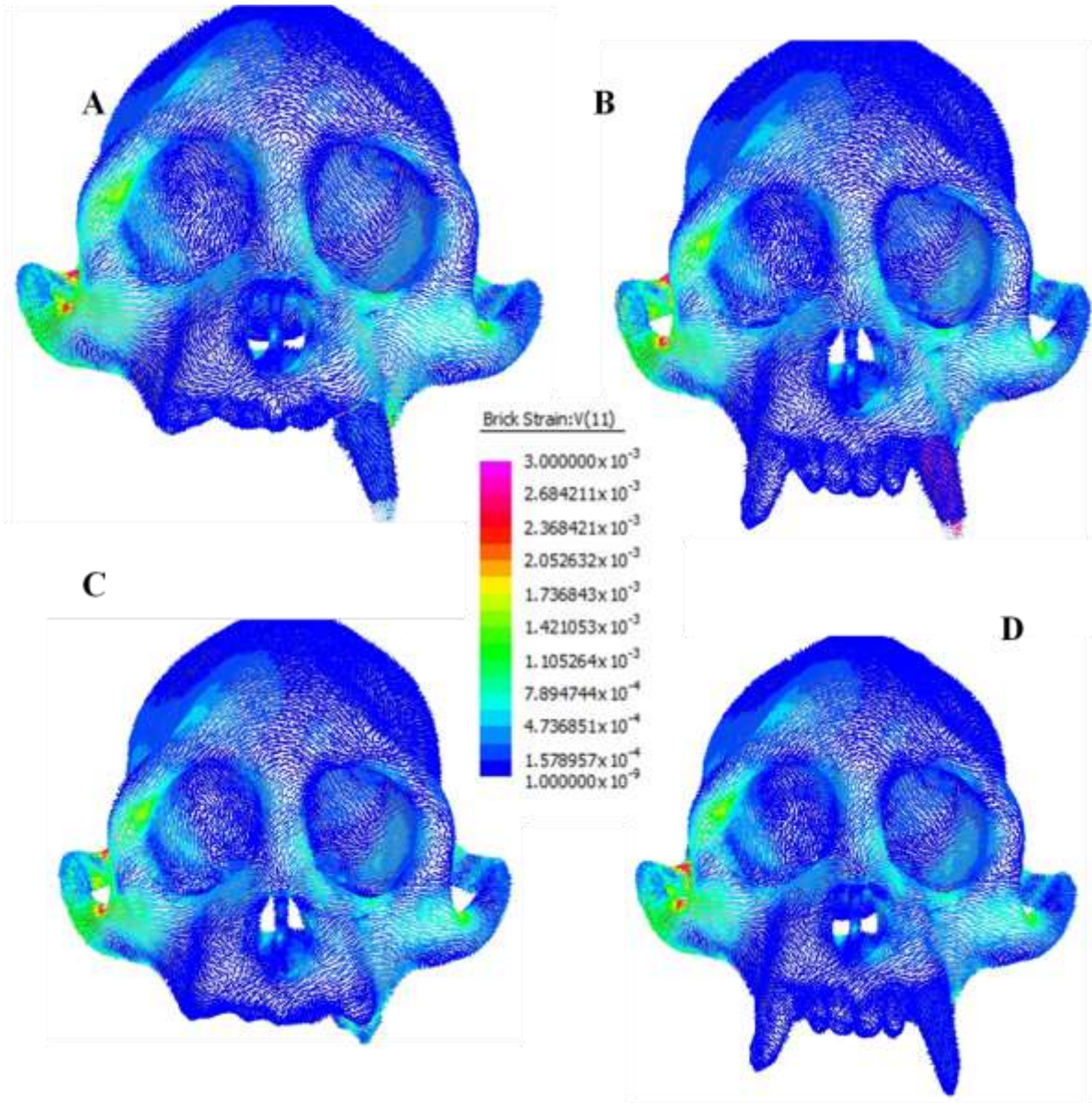
Figure 27: Max Principal (11) Strain results for Models A-D, front view

To validate the *in silico* models, three-dimensional component strain data were extracted using two sampling methods from the *in silico* models and compared to *in vivo* specimen-specific strain data. The two sampling methods are the *average* and *equilateral* methods presented in Chapter 3, pages 32-33. Using these methods the principal maximum, minimum, and shear strains were calculated along with the orientation of the

maximum principal strain. Percent differences between the *in silico* and *in vivo* data were calculated for each of the models (Table 7). The original principal strains, shear strain, and orientation data for each model are displayed in **Error! Reference source not found.**. To visualize the percent difference more clearly, the results were color coded with respect to how close the *in vivo* and *in silico* results are to each other. A green cell indicates a percent difference of about 25 percent of less, a yellow cell refers to percent differences between 25 and 50 percent, and a red cell represents a percent difference exceeding 50 percent.

Table 7: Fully activated EMG: Percent Difference between *in vivo* strain gage and *in silico* models (A-D) data

	%<25
	25<%<50
	%>50

Percent Difference Left Anterior Pillar (%)

Measurement		Model A		Model B		Model C		Model D	
		average	equilateral	average	equilateral	average	equilateral	average	equilateral
Max	(ε_1)	49.24	66.89	44.49	67.60	16.94	16.63	18.98	16.39
Min	(ε_3)	118.12	127.02	108.97	116.01	92.52	105.83	85.56	101.11
Shr	(γ_{max})	89.12	101.62	80.74	94.04	59.28	69.29	55.21	65.49
El_A	(θ_p)	22.06	22.92	19.29	15.30	17.61	14.43	11.84	15.19

Percent Difference Right Anterior Pillar (%)

Measurement		Model A		Model B		Model C		Model D	
		average	equilateral	average	equilateral	average	equilateral	average	equilateral
Max	(ε_1)	16.22	20.89	18.27	26.62	6.93	18.25	13.47	11.16
Min	(ε_3)	94.60	77.19	40.20	138.44	46.37	12.45	35.60	2.50
Shr	(γ_{max})	5.89	29.79	9.64	51.64	0.34	4.22	7.59	4.12
El_A	(θ_p)	41.12	32.60	24.44	12.10	23.24	48.50	22.49	43.47

Percent Difference Right Zygomatic Arch (%)

Measurement		Model A		Model B		Model C		Model D	
		average	equilateral	average	equilateral	average	equilateral	average	equilateral
Max	(ε_1)	68.16	85.83	70.25	75.66	63.37	82.73	64.84	76.26
Min	(ε_3)	20.56	36.44	14.67	67.15	24.57	46.03	12.42	64.16
Shr	(γ_{max})	47.58	45.02	46.88	29.15	46.04	40.12	42.43	30.33
El_A	(θ_p)	17.97	2.64	15.91	1.56	18.73	1.36	14.57	0.72

Percent differences were used to compare each Model to the *in vivo* data. Models C and D produced more realistic strains in the left and right anterior pillar regions. These regions are more localized to the alveolus process and the results suggest that it may be more important to have the adjacent sockets filled rather than modeling the adjacent teeth with realistic material properties (PDL and tooth enamel). The percent differences for the right zygomatic arch were more consistent throughout each model due to the fact that this location is a little further away from the alveolus process. Overall, the maximum *in silico* principal strains were significantly off when compared to the *in vivo* strains (about 70% across the board). Some of the inconsistencies comparing the *in silico* data to the *in vivo* data are better revealed in **Error! Reference source not found.**. Overall, Model A was selected to be the isotropic model that was converted to an orthotropic model in Study 2. This selection was made based upon prior results displaying that Model A had the lowest percent difference of strain and orientation results at the most sampled regions. With the new results displayed in this thesis it seems as if Model C or Model D should have been chosen to create a regional orthotropic model of *Curly*. In Study 2 only the *average* sampling method was used based upon the fact that this method achieved the lowest percent difference strains and orientations in Study 1.

We are not entirely convinced that Models C and D more accurately portrayed *Curly* based only upon these findings. A key assumption in processing the EMG signal data is that a 100% activation level is assumed to the maximum EMG peak for a given chew. So we decided to investigate a more realistic EMG activation level. Assume the muscle groups are all activated at some uniform level less than full activation and let α represent this fractional activation level, i.e. $0 \leq \alpha \leq 1$. Thus, all FEA strains will be proportional to

this unknown activation level α. We now seek to determine the value of α which minimizes the error in the model. Let Π represent the square of the error between FEA *in silico* and *in vivo* strain measurements of maximum and minimum principal strains at n sampling points.

$$\Pi = \sum_{i=1}^{n} \left(\alpha \varepsilon_{1fea} - \varepsilon_{1invivo} \right)_i^2 + \left(\alpha \varepsilon_{3fea} - \varepsilon_{3invivo} \right)_i^2 \tag{1}$$

We wanted the value of α that results in the least square error, i.e. minimizes Π. Thus

$$\frac{\partial \Pi}{\partial \alpha} = 0 = 2 \left(\sum_{i=1}^{n} \left(\varepsilon_{1fea} \left(\alpha \varepsilon_{1fea} - \varepsilon_{1invivo} \right) \right)_i + \left(\varepsilon_{3fea} \left(\alpha \varepsilon_{3fea} - \varepsilon_{3invivo} \right) \right)_i \right) \tag{2}$$

Solving for α yields

$$\alpha = \frac{\displaystyle\sum_{i=1}^{n} \left(\varepsilon_{1fea} \varepsilon_{1invivo} + \varepsilon_{3fea} \varepsilon_{3invivo} \right)_i}{\displaystyle\sum_{i=1}^{n} \left(\varepsilon_{1fea}^2 + \varepsilon_{3fea}^2 \right)_i} \tag{3}$$

Using the *in vivo* and *in silico* strains from Table 19, we achieve a different α-value for each model and for each strain sampling technique (Table 8).

Table 8: Calculated α values from RMS error

Model	Technique	α value
A	Average	0.45
A	Equilateral	0.37
B	Average	0.49
B	Equilateral	0.42
C	Average	0.57
C	Equilateral	0.47
D	Average	0.59
D	Equilateral	0.51

With these α-values we then scaled the *in silico* results from Table 17 to those shown in
Table 18 and again calculated the percent differences between in vivo and in silico strains
(Table 9).

Table 9: α scaled: Percent Difference between *in vivo* strain gage and *in silico* models (A-
D) data

%<25
25<%<50
%>50

		Percent Difference Left Anterior Pillar (%)							
Measurement		**Model A**		**Model B**		**Model C**		**Model D**	
		average	*equilateral*	*average*	*equilateral*	*average*	*equilateral*	*average*	*equilateral*
Max	(ε_1)	28.96	28.51	25.92	15.84	38.45	56.23	32.85	50.52
Min	(ε_3)	54.85	50.58	49.83	45.46	43.50	42.66	38.75	42.61
Shr	(γ_{max})	16.37	13.73	14.28	15.79	5.20	2.18	4.49	0.07
El_A	(θ_p)	22.06	22.92	19.29	15.30	17.61	14.43	11.84	15.19

		Percent Difference Right Anterior Pillar (%)							
Measurement		**Model A**		**Model B**		**Model C**		**Model D**	
		average	*equilateral*	*average*	*equilateral*	*average*	*equilateral*	*average*	*equilateral*
Max	(ε_1)	61.15	106.87	51.79	102.35	48.03	86.63	53.26	75.34
Min	(ε_3)	144.33	143.11	101.65	171.47	94.87	81.84	82.87	67.78
Shr	(γ_{max})	80.49	113.18	59.78	120.28	54.82	74.85	54.07	61.85
El_A	(θ_p)	41.12	32.60	24.44	12.10	23.24	48.50	22.49	43.47

		Percent Difference Right Zygomatic Arch (%)							
Measurement		**Model A**		**Model B**		**Model C**		**Model D**	
		average	*equilateral*	*average*	*equilateral*	*average*	*equilateral*	*average*	*equilateral*
Max	(ε_1)	8.43	6.51	2.07	6.62	9.71	13.52	15.05	12.23
Min	(ε_3)	57.16	117.74	55.15	130.60	30.97	108.35	39.24	117.38
Shr	(γ_{max})	30.68	51.30	23.44	55.39	9.03	33.47	9.10	37.07
El_A	(θ_p)	17.97	2.64	15.91	1.56	18.73	1.36	14.57	0.72

With this new method, we find that in general all the models are more accurate in the left anterior pillar, less accurate in the right anterior pillar, and roughly the same level of accuracy compared to the previous models that assumed the maximum peak activation level corresponds to 100% muscle activation. Between models we find that Model D still fits the *in vivo* data the best followed by Model C, Model B and finally Model A. The average method is more accurate than the equilateral method, confirming our prior results. There is a higher level of accuracy in predicting strain orientation than predicting any of the three stress components.

4.2 Orthotropic Validation

Model A was taken from Study 1 and modified using methods discussed above to include orthotropic material properties. *In vitro* measured orthotropic material properties were assigned to 32 regions of Model A and then the model was run under the same loading conditions used in Study 1. The strains and orientations achieved at each of the strain gage locations are listed in Table 19. The results are expressed in terms of percent differences (Table 10). We are assuming the lower the percent difference between the *in vivo* and *in silico* data, the more realistic the *in silico* model. The isotropic model produces more realistic (lower percent differences) maximum principal strains in the right anterior pillar and right zygomatic arch. However, we found that the orthotropic model improves the percent differences of the maximum principal strain orientation in all regions while producing similar maximum principal strain results in the right anterior pillar. Both isotropic and orthotropic models produce significantly higher maximum principal strains and lower minimum principal strains then what the *in vivo* results depict in the right zygomatic arch. Although the isotropic model produces poor tensile strain

results when compared to the *in vivo* data, the resulting compressive strain results in the right zygomatic arch are acceptable. The *in silico* compressive strains occurring in the left and right anterior pillars are significantly different than the *in vivo* results. These results do not produce a consistent trend claiming that modeling using orthotropic material properties results in more realistic strains when compared to *in vivo* specimen specific results. This may be a result of the overexposed EMG signal.

Table 10: Fully Activated EMG: Percent differences between *in vivo* specimen specific data and Orthotropic/Isotropic *in silico* Model A data

				Percent Difference (%)	
				Orthotropic	*Isotropic*
LPILL	Max	(ε_1)		15.12	49.24
	Min	(ε_3)		96.29	118.12
	Shr	(γ_{max})		61.42	89.12
	El_A	(θ_p)		9.70	22.06
RPILL	Max	(ε_1)		21.20	16.22
	Min	(ε_3)		25.59	-94.60
	Shr	(γ_{max})		34.43	-5.89
	El_A	(θ_p)		-22.62	-41.12
RZARCH	Max	(ε_1)		125.21	68.16
	Min	(ε_3)		127.77	20.56
	Shr	(γ_{max})		126.55	47.58
	El_A	(θ_p)		17.31	17.97

Legend:
- %<25
- 25<%<50
- %>50

Again we decided to apply the α-scaling method to the orthotropic and isotropic strain data. The α-value from Model A using the averaging technique (Table 8) was chosen for both isotropic and orthotropic models. This scaling factor was multiplied by the three stress components for the left/right pillars, and right zygomatic arch in Table 19 to achieve the strains in Table 20. Then the new percent differences were calculated

between *in vivo* specimen specific data and the orthotropic/isotropic *in silico* Model A data (Table 11). The percent differences decreased in the LPILL and RPILL when modeling the material properties using orthotropic data. However in the RZARCH the three stress components had lower percent differences when using isotropic material properties, while the orientation of maximum principal strain stayed consistent between the orthotropic and isotropic models.

Table 11: α scaled: Percent differences between *in vivo* specimen specific data and Orthotropic/Isotropic *in silico* Model A data

			α scaled	
%<25			**Percent Difference (%)**	
25<%<50			**Orthotropic**	**Isotropic**
%>50				
LPILL	Max	(ε_1)	17.47	-28.96
	Min	(ε_3)	25.41	54.85
	Shr	(γ_{max})	-15.93	16.37
	El_A	(θ_p)	9.70	22.06
RPILL	Max	(ε_1)	-56.56	-61.15
	Min	(ε_3)	-52.44	-144.33
	Shr	(γ_{max})	-43.93	-80.49
	El_A	(θ_p)	-22.62	-41.12
RZARCH	Max	(ε_1)	65.10	-8.43
	Min	(ε_3)	68.88	-57.16
	Shr	(γ_{max})	67.07	-30.68
	El_A	(θ_p)	17.31	17.97

The von Mises stress contour plots (Figure 28) are a little difficult to interpret due to the inconsistency of legend scaling. However, this was the only way to show the stress concentrations of each modeling technique. The back of the skull produces similar stress patterns when using both isotropic and orthotropic models. The stress concentrations on

both zygomatic arches are far greater towards the posterior of the arch if the cranium is

modeled with orthotropic properties (frontal view in Figure 28). It is also noted that the

increased stresses occurring around the loaded tooth in the isotropic model are reduced in

the orthotropic material model (side views in Figure 28). Above the LUC there is also a

large decrease in stress when modeling with orthotropic properties.
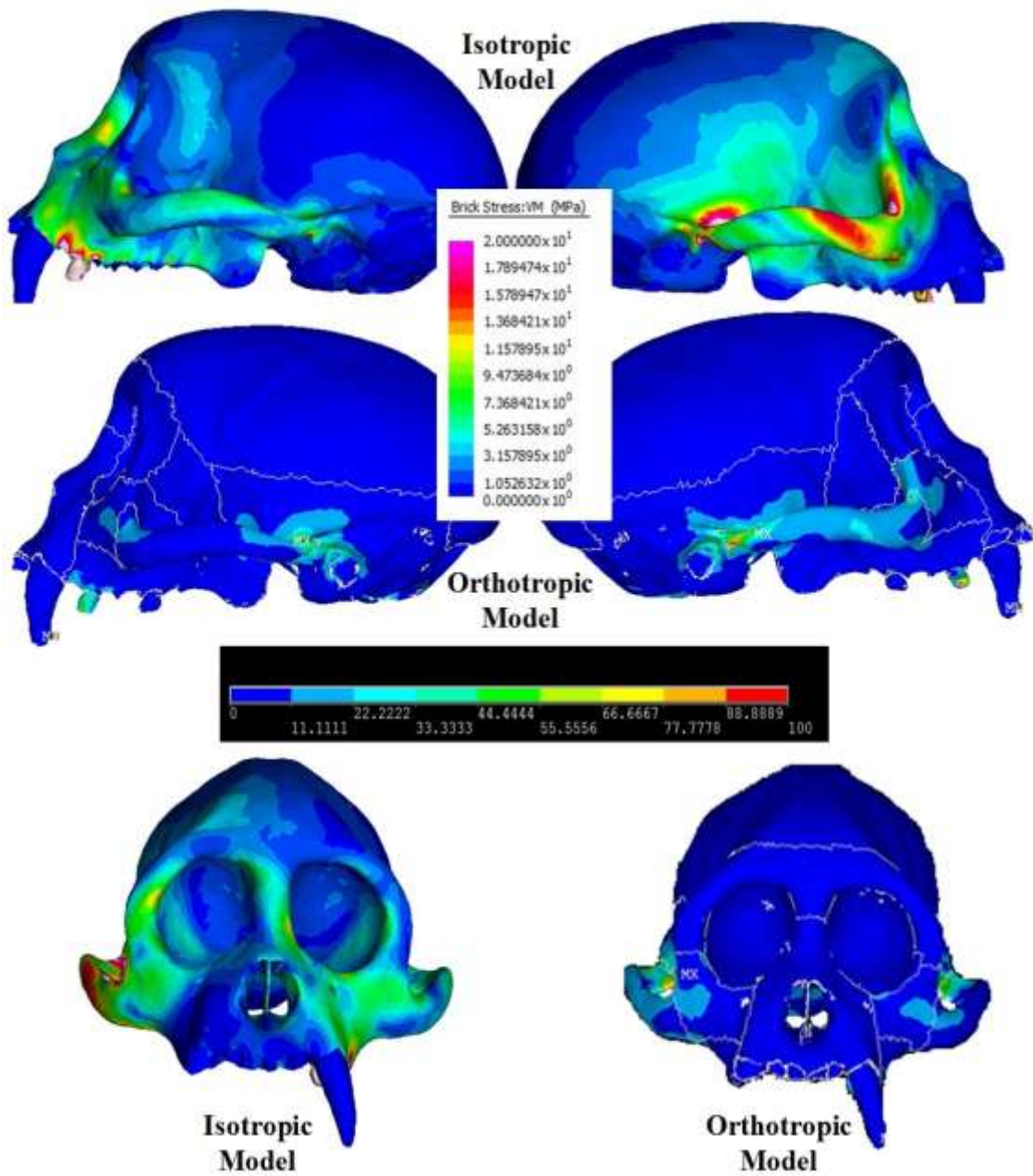
Figure 28: Comparing Von Mises stress (MPa) for Isotropic and Orthotropic Model A
add arrow to front isotropic view

CHAPTER 5

RESULTS: STUDY 2

The objective of the first hypothesis was to determine whether or not a relationship exists between the orientation of maximum principal strain and material property (stiffness) orientation within various anatomical regions of a skull under masticatory loading. We developed the Block Example portion of this study to validate the technique we used to define and control orientation angle. Then a Probabilistic Design method was used to acquire statistical trends between these orientations in the defined anatomical regions. To address the second hypothesis we developed a short design optimization method to find out if the global elastic strain energy is minimized with respect to orientations of material property stiffness.

5.1 Block Example

We examined a simple Probabilistic Design model to ensure extracting the strain component data from the fixed-CS was indeed the correct method. This model was a simple cube with the top half assigned with isotropic material property number one and the bottom half of the cube assigned with isotropic material property number two (Figure 29). Two fixed-CS were assigned to the cube; CS-11 on the top center of the cube and CS-12 on the bottom center of the cube. The z-axes of these components were outward normal, while the x-axes were mirrored and the y-axes were in the same direction. This was consistent with left and right components of the same anatomical region for *Curly's* model. Two rotating-CS were also assigned to the cube (Figure 30); CS-111 aligned with CS-11 and CS-112 aligned with CS-12.
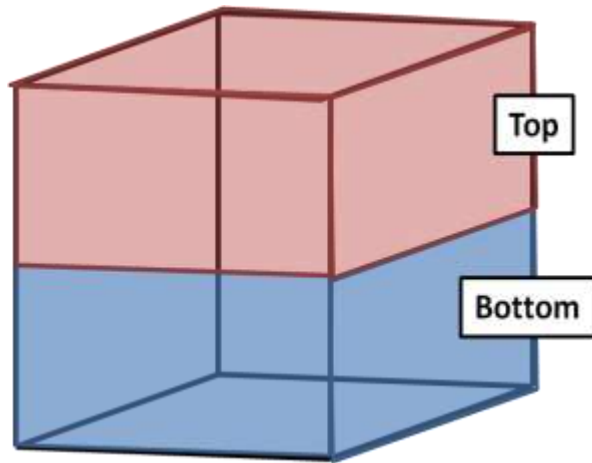
Figure 29 : Simple Block Model
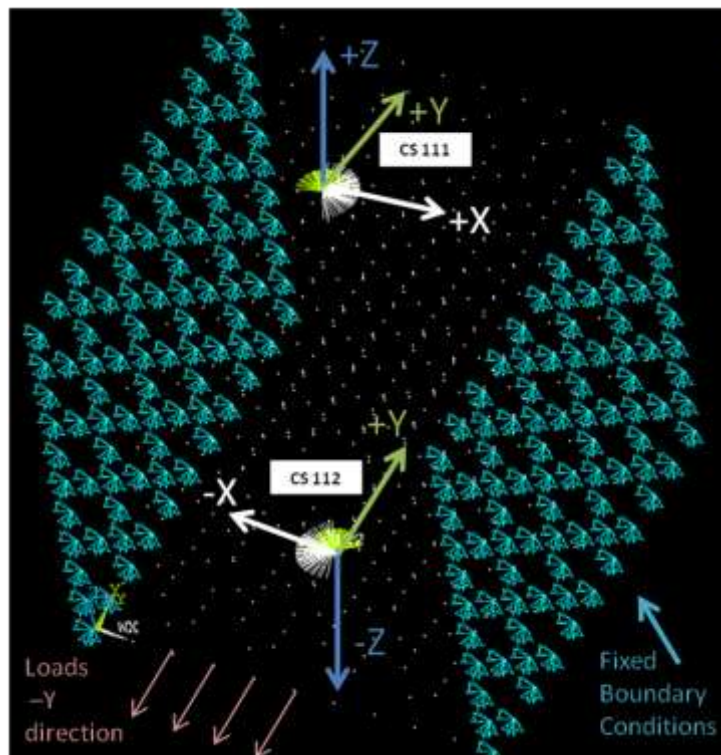
Figure 30 : Block Example displaying fixed and rotated coordinate systems

The same setup described in Chapter 3: Materials and Methods: Study 2 was used for writing the batch code, input variable file, and output parameter file was used for this model. In this case there was only one input variable (θ_z with respect to CS-11). The

angle which rotated CS-112 around CS-12 was defined to be equal and opposite of θ_z. One side of the cube perpendicular to the planes containing the defined coordinate system was fixed. The opposing side was simply loading in the negative z direction. The output parameters of interest were the strain components (ε_x, ε_y, and γ_{xy}) extracted two ways (1) with respect to the fixed-CS and (2) with respect to the rotated-CS. Once this data was extracted from the Probabilistic Design model a similar post processing method in Excel was used as defined in Chapter 3: Materials and Methods: Study 2. Scatter plots were created to compare the linear relationship of material property stiffness orientation (θ_z) to the orientation of maximum principal strain (θ_p) with respect to (1) the rotating axis and (2) the fixed axis.

We determined that the correct method was when the maximum principal strain orientation was defined relative to the stationary coordinate system. With regard to the Probabilistic Design of the Block Example, there was very little to no variation in maximum principal strain orientation with respect to a wide variety of material stiffness orientation inputs. This horizontal relationship shown in the scatter plots (Figure 31: *upper plots*) was expected due to the fact that we modeled the block with isotropic material properties. We determined that the method in which orientation was defined relative to a non-stationary coordinate system, which was the same coordinate system used to orient material direction, was incorrect and produced unrealistic results. What was actually being recorded was the change in orientation of the rotated-CS with respect to the fixed-CS giving a nearly perfect linear relationship (Figure 31: *lower plots*). This Block Example validated that the orientation of principal strain, as well as orientation of

material stiffness, need to be measured with respect to local fixed coordinate systems in Study 2.
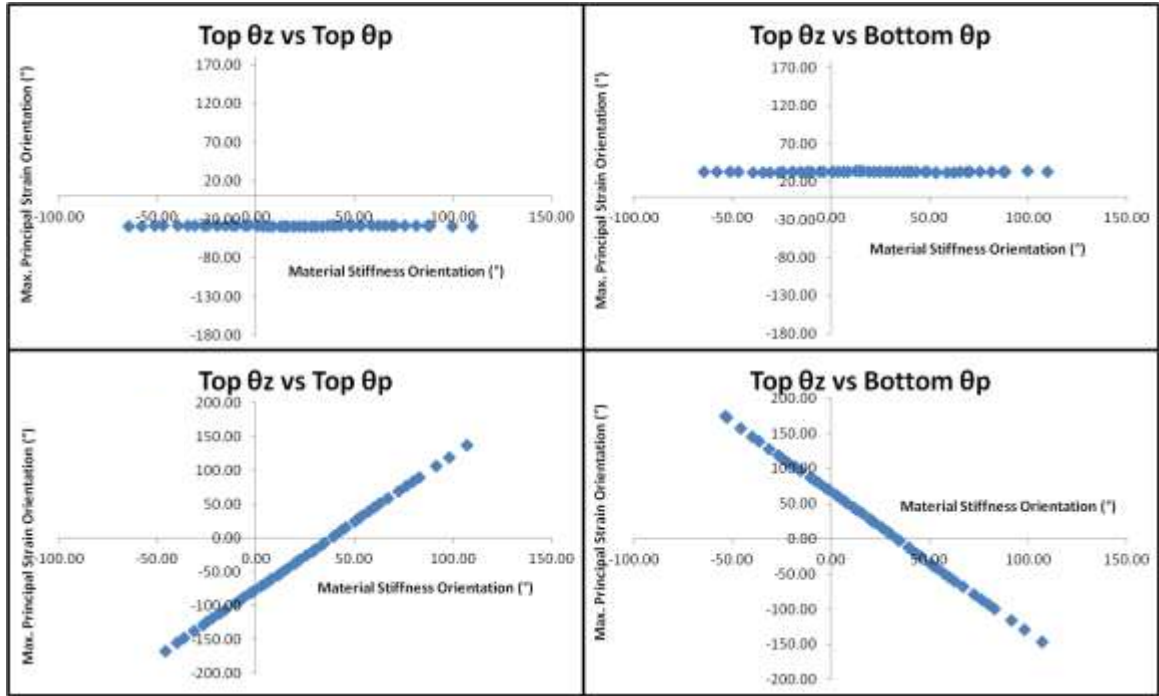
Figure 31 : Scatter plots examining the effect of material stiffness orientation of the top half of the block on the maximum principal strain orientations of the top half and bottom half of the block *(Upper plots) extracted from **fixed**-CS and (Lower plots) extracted from **rotated**-CS*

5.2 Probabilistic Design

We used a Probabilistic Design to determine whether there is a relationship between the material property stiffness orientation and the maximum principal strain orientation. A Probabilistic Design is one particular way of sampling parameter space by using a batch code, list of input variables, and list of output variables. The input variables for each finite element analysis were selected at random using a Latin Hypercube method and a Truncated Gaussian distribution defined using *Cebus apella* specimen specific mean orientations and population (n=5) specific standard deviations.

This orthotropic material stiffness data was measured by Paul Dechow's Lab (Baylor College of Dentistry, Dallas, unpublished). We defined the output parameters as the maximum and minimum principal strains, shear strain, and the orientation of maximum principal strain at each anatomical region. After the probabilistic design was run, in order to compare each anatomical region's maximum principal strain orientation with respect to the stiffness orientation at each anatomical region, a correlation matrix was developed (Table 13). The number shown in each of the cells is a Pearson's Correlation Coefficient which compares two arrays (stiffness orientation, strain orientation). For an experiment with 50 simulations and a desired p-value of 0.05 a Pearson's correlation coefficient of 0.280 or higher defines a significantly correlated data set. The white cells represent an insignificant correlation, the light green cells represent a moderately significant correlation, and the dark green cells represent a strong correlation.

Maximum principal strain orientation in the right and left zygomatic arches are both significantly correlated with material stiffness orientations of the temporal regions (A and B) on both the right and left sides of the skull (Figure 14). There is a stronger relationship at the underside of the zygomatic arches (right, left) with the temporal region (0.94 and 0.73) then compared to the upper side of the zygomatic arches (0.72 and 0.45). The way we defined the location of the temporal region is towards the posterior bottom of the cranium (Figure 14). Anatomically it makes sense that the maximum principal strain orientations of the lower zygomatic arch regions depend on the stiffness of the adjoining temporal region.

The material stiffness orientation of the temporal region also plays a significant role with respect to the maximum principal strain orientations of the entire left and right

maxilla regions (0.65-0.81). The correlation exists when we examined the same side of the cranium or compared opposing sides. The orbital and palette strain orientations closest to the loaded tooth (LPalette, LOrbitalB, C, D and ROrbitalC) have higher correlations with the stiffness orientation of the temporal region than the further away orbital and the right palette regions. Finally the working side temporal region (LTemporalB) has a great dependency on material stiffness orientations for all other temporal regions (LTemporalA, LTemporalB, RTemporalA, and RTemporalB).

Next, a significant relationship exists between the maximum principal strain orientation of the upper section of both zygomatic arches with respect to the material stiffness orientation of the zygomatic arches as a whole. Maximum principal strain orientations of the lower regions of the zygomatic arches did not show a significant relationship. This may indicate that the zygomatic arch does not need to be broken up into two sections but instead may be modeled with one stiffness direction though out the entire arch.

The next four significant correlations all have the highly derived brow region of the *Cebus* skull in common. The principal strain orientations resulting in the frontal regions outlining the brow and lateral orbital regions are highly correlated with each region's corresponding material stiffness orientation. At the brow ridge (left and right frontal_A regions) the strain orientations are greatly dependent on the material stiffness orientation, more so than the frontal regions (frontal_B) bordering the lateral portions of the orbital (Figure 14). The maximum principal strain orientations of the upper two orbital quadrants closest to the brow ridge (right orbital A and D, left orbital A and B) are also significantly correlated with the material stiffness orientations. Finally, both side

78

and frontal maxilla regions heavily on the material property stiffness orientations defined in left and right side-maxilla regions. The same is true for the left anterior parietal region (LParietalC). The fact that these regions are on the working side may play a role in their significant correlation coefficients.

Although there are many significant correlations between anatomical regions relating maximum principal strain and material stiffness orientations, the effects are small. The amount of variation in material stiffness orientation is dependent on the anatomical region (Table 12). We found that regions very close to the loaded tooth (palette, front maxilla, and side maxilla) all have small variations in resulting maximum principal strain orientation. The front maxilla and palette regions both have a range of 180 degrees of material stiffness orientation and only result in one to four degrees of variation in maximum principal strain orientation respectively. Anatomical regions further away from the loaded tooth, such as the parietal and temporal regions both have larger variations in maximum principal strain orientation (30-50 degrees) with similar ranges in material stiffness orientation. This decrease in maximum principal strain orientation variation moving from the skull's posterior to anterior became clear when we compared parietal regions A-C. Both left and right parietal regions are divided into: parietal_a in the back, parietal_b in the middle, and parietal_c in the front of the skull (Figure 14). For example, on the left side of the skull the variation in maximum principal strain orientation decreases from 42 degrees at parietal_a, to 42 degrees at parietal_b, and finally 9 degrees at parietal_c.

The scatter plots presented in **Error! Reference source not found.** demonstrate a variety of results. When we fit a line to a scatter plot that results in a horizontal line, no

variation exists in maximum principal strain orientation with respect to material stiffness orientation and thus no correlation (r = 0). Examples of scatter plots with no correlation include the left sphenoid, left orbital_C, and left zygomatic_a regions (Study 2: Probabilistic Design Scatter Plots). An example of a positively correlated scatter plot is shown in the right zygomatic A, as the orientation of material stiffness increases so does the orientation of maximum principal strain. While an example of a negatively correlated scatter plot is shown in (Study 2: Probabilistic Design Scatter Plots: Right Orbital D), as the orientation of material stiffness increases the orientation of maximum principal strain decreases.

Table 12 : Variation in Max. Principal Strain Orientation with respect to range material stiffness orientation input (defined as ± 3 Standard Deviation)

Anatomical Region	Material Stiffness Orientation Range (°)	Max. Principal Strain Orientation Range (°)
Front Maxilla	180	1-2
Side Maxilla	54	2-3
Palette	180	3-4
Orbital	78	7-169
Parietal	180	7-50
Frontal	90	5-14
Temporal	156	4-32
Zygomatic Arch	54	6-14

Table 13: Correlation Matrix comparing stiffness orientation and maximum principal strain orientation at various anatomical regions

Legend:
- r < 0.27
- 0.28 < r < 0.50
- r > 0.51

	RFMAXILLA θp	LFMAXILLA θp	RPALETTE θp	LPALETTE θp	RS MAXILLA θp	LSMAXILLA θp	RORBITALA θp	RORBITALB θp	RORBITALC θp	RORBITALD θp	LORBITALA θp	LORBITALB θp	LORBITALC θp	LORBITALD θp	RPARIETALA θp	RPARIETALB θp	RPARIETALC θp	LPARIETALA θp	LPARIETALB θp	LPARIETALC θp	RFRONTALA θp	RFRONTALB θp	LFRONTALA θp	LFRONTALB θp	RTEMPORALA θp	RTEMPORALB θp	LTEMPORALA θp	LTEMPORALB θp	RZYGOMATICA θp	RZYGOMATICB θp	LZYGOMATICA θp	LZYGOMATICB θp
RFMAXILLA θr	0.00	0.00	0.00	0.00	0.00	0.00	0.00	0.00	0.00	-0.34	0.00	0.00	0.00	0.00	0.00	0.00	0.00	0.00	0.00	0.00	0.00	0.00	0.00	0.00	0.00	0.00	0.00	0.00	0.00	0.00	0.00	0.00
LFMAXILLA θr	0.00	0.00	0.00	0.00	0.00	0.00	0.00	0.00	0.00	0.34	0.00	0.00	0.00	0.00	0.00	0.00	0.00	0.00	0.00	0.00	0.00	0.00	0.00	0.00	0.00	0.00	0.00	0.00	0.00	0.00	0.00	0.00
RPALETTE θr	0.00	0.00	0.00	0.00	0.00	0.00	0.00	0.00	0.00	0.00	0.00	0.00	0.00	0.00	0.00	0.00	0.00	0.00	0.00	0.00	0.00	0.00	0.00	0.00	0.00	0.00	0.00	0.00	0.00	0.00	0.00	0.00
LPALETTE θr	0.00	0.00	0.00	0.00	0.00	0.00	0.00	0.00	0.00	0.00	0.00	0.00	0.00	0.00	0.00	0.00	0.00	0.00	0.00	0.00	0.00	0.00	0.00	0.00	0.00	0.00	0.00	0.00	0.00	0.00	0.00	0.00
RSMAXILLA θr	-0.47	0.47	0.00	0.00	0.32	0.50	0.00	0.00	0.32	0.00	0.00	0.00	0.00	0.00	0.00	0.00	0.00	0.00	0.00	0.00	0.00	0.00	0.00	0.00	-0.41	0.00	-0.30	0.00	0.29	0.31	-0.39	0.35
LSMAXILLA θr	0.47	-0.47	0.00	0.00	-0.32	-0.50	0.00	0.00	-0.32	0.00	0.00	0.00	0.00	0.00	0.00	0.00	0.00	0.00	0.00	0.00	0.00	0.00	0.00	0.00	0.41	0.00	0.30	0.00	-0.29	-0.31	0.39	-0.35
RORBITALA θr	0.00	0.00	0.00	0.00	0.00	0.00	0.34	-0.38	0.00	-0.59	0.33	0.65	0.00	-0.35	0.00	0.00	0.00	0.00	0.00	0.00	0.00	0.00	0.00	0.00	0.00	0.00	0.00	0.00	0.00	0.00	0.00	0.00
RORBITALB θr	0.00	0.00	0.00	0.00	0.00	0.00	0.34	-0.38	0.00	-0.59	0.33	0.65	0.00	-0.35	0.00	0.00	0.00	0.00	0.00	0.00	0.00	0.00	0.00	0.00	0.00	0.00	0.00	0.00	0.00	0.00	0.00	0.00
RORBITALC θr	0.00	0.00	0.00	0.00	0.00	0.00	0.34	-0.38	0.00	-0.59	0.33	0.65	0.00	-0.35	0.00	0.00	0.00	0.00	0.00	0.00	0.00	0.00	0.00	0.00	0.00	0.00	0.00	0.00	0.00	0.00	0.00	0.00
RORBITALD θr	0.00	0.00	0.00	0.00	0.00	0.00	0.34	-0.38	0.00	-0.59	0.33	0.65	0.00	-0.35	0.00	0.00	0.00	0.00	0.00	0.00	0.00	0.00	0.00	0.00	0.00	0.00	0.00	0.00	0.00	0.00	0.00	0.00
LORBITALA θr	0.00	0.00	0.00	0.00	0.00	0.00	-0.34	0.38	0.00	0.59	-0.33	-0.65	0.00	0.35	0.00	0.00	0.00	0.00	0.00	0.00	0.00	0.00	0.00	0.00	0.00	0.00	0.00	0.00	0.00	0.00	0.00	0.00
LORBITALB θr	0.00	0.00	0.00	0.00	0.00	0.00	-0.34	0.38	0.00	0.59	-0.33	-0.65	0.00	0.35	0.00	0.00	0.00	0.00	0.00	0.00	0.00	0.00	0.00	0.00	0.00	0.00	0.00	0.00	0.00	0.00	0.00	0.00
LORBITALC θr	0.00	0.00	0.00	0.00	0.00	0.00	-0.34	0.38	0.00	0.59	-0.33	-0.65	0.00	0.35	0.00	0.00	0.00	0.00	0.00	0.00	0.00	0.00	0.00	0.00	0.00	0.00	0.00	0.00	0.00	0.00	0.00	0.00
LORBITALD θr	0.00	0.00	0.00	0.00	0.00	0.00	-0.34	0.38	0.00	0.59	-0.33	-0.65	0.00	0.35	0.00	0.00	0.00	0.00	0.00	0.00	0.00	0.00	0.00	0.00	0.00	0.00	0.00	0.00	0.00	0.00	0.00	0.00
RPARIETALA θr	0.00	0.00	0.00	0.00	0.00	0.00	0.00	0.00	0.00	0.00	0.00	0.00	0.00	0.00	0.28	-0.33	-0.51	0.00	0.00	0.45	0.00	0.00	0.00	0.00	0.32	0.00	0.00	0.00	0.00	0.00	0.00	0.00
RPARIETALB θr	0.00	0.00	0.00	0.00	0.00	0.00	0.00	0.00	0.00	0.00	0.00	0.00	0.00	0.00	0.28	-0.33	-0.51	0.00	0.00	0.45	0.00	0.00	0.00	0.00	0.32	0.00	0.00	0.00	0.00	0.00	0.00	0.00
RPARIETALC θr	0.00	0.00	0.00	0.00	0.00	0.00	0.00	0.00	0.00	0.00	0.00	0.00	0.00	0.00	0.28	-0.33	-0.51	0.00	0.00	0.45	0.00	0.00	0.00	0.00	0.32	0.00	0.00	0.00	0.00	0.00	0.00	0.00
LPARIETALA θr	0.00	0.00	0.00	0.00	0.00	0.00	0.00	0.00	0.00	0.00	0.00	0.00	0.00	0.00	-0.28	0.33	0.51	0.00	0.00	-0.45	0.00	0.00	0.00	0.00	-0.32	0.00	0.00	0.00	0.00	0.00	0.00	0.00
LPARIETALB θr	0.00	0.00	0.00	0.00	0.00	0.00	0.00	0.00	0.00	0.00	0.00	0.00	0.00	0.00	-0.28	0.33	0.51	0.00	0.00	-0.45	0.00	0.00	0.00	0.00	-0.32	0.00	0.00	0.00	0.00	0.00	0.00	0.00
LPARIETALC θr	0.00	0.00	0.00	0.00	0.00	0.00	0.00	0.00	0.00	0.00	0.00	0.00	0.00	0.00	-0.28	0.35	0.51	0.00	0.00	-0.45	0.00	0.00	0.00	0.00	-0.32	0.00	0.00	0.00	0.00	0.00	0.00	0.00
RFRONTALA θr	0.00	0.00	0.00	0.00	0.00	0.00	0.00	0.00	0.00	0.00	0.00	0.00	0.00	0.00	0.00	0.00	0.00	0.00	0.00	0.00	-0.88	0.58	-0.83	-0.41	0.00	0.00	0.00	0.00	0.00	0.00	0.00	0.00
RFRONTALB θr	0.00	0.00	0.00	0.00	0.00	0.00	0.00	0.00	0.00	0.00	0.00	0.00	0.00	0.00	0.00	0.00	0.00	0.00	0.00	0.00	-0.88	0.58	-0.83	-0.41	0.00	0.00	0.00	0.00	0.00	0.00	0.00	0.00
LFRONTALA θr	0.00	0.00	0.00	0.00	0.00	0.00	0.00	0.00	0.00	0.00	0.00	0.00	0.00	0.00	0.00	0.00	0.00	0.00	0.00	0.00	0.88	-0.58	0.83	0.41	0.00	0.00	0.00	0.00	0.00	0.00	0.00	0.00
LFRONTALB θr	0.00	0.00	0.00	0.00	0.00	0.00	0.00	0.00	0.00	0.00	0.00	0.00	0.00	0.00	0.00	0.00	0.00	0.00	0.00	0.00	0.88	-0.58	0.83	0.41	0.00	0.00	0.00	0.00	0.00	0.00	0.00	0.00
RTEMPORALA θr	0.74	-0.81	0.37	0.66	-0.74	-0.65	-0.47	0.50	0.53	0.00	-0.44	-0.59	-0.75	0.67	0.00	0.00	0.00	0.42	0.00	0.00	0.00	-0.31	0.00	0.42	-0.29	0.46	0.00	0.64	-0.72	0.94	-0.73	0.45
RTEMPORALB θr	0.74	-0.81	0.37	0.66	-0.74	-0.65	-0.47	0.50	-0.53	0.00	-0.44	-0.59	-0.75	0.67	0.00	0.00	0.00	0.42	0.00	0.00	0.00	-0.31	0.00	0.42	-0.29	0.46	0.00	0.64	-0.72	0.94	0.00	0.45
LTEMPORALA θr	-0.74	0.81	-0.37	-0.66	0.74	0.65	0.47	-0.50	0.53	0.00	0.44	0.59	0.75	-0.67	0.00	0.00	0.00	-0.42	0.00	0.00	0.00	0.31	0.00	-0.42	0.29	-0.46	0.00	0.64	0.72	-0.94	0.73	-0.45
LTEMPORALB θr	-0.74	0.81	-0.37	-0.66	0.74	0.65	0.47	-0.50	0.53	0.00	0.44	0.59	0.75	-0.67	0.00	0.00	0.00	-0.42	0.00	0.00	0.00	0.31	0.00	-0.42	0.29	-0.46	0.00	0.64	0.72	-0.94	0.73	-0.45
RZYGOMATICA θr	0.00	0.00	0.00	0.00	0.36	0.29	0.00	-0.30	0.00	0.00	0.31	0.00	0.00	0.00	0.00	0.00	0.00	0.00	0.00	0.00	0.00	0.00	0.00	0.00	0.39	0.00	0.00	0.00	0.78	0.00	0.00	0.50
RZYGOMATICB θr	0.00	0.00	0.00	0.00	0.36	0.29	0.00	-0.30	0.00	0.00	0.31	0.00	0.00	0.00	0.00	0.00	0.00	0.00	0.00	0.00	0.00	0.00	0.00	0.00	0.39	0.00	0.00	0.00	0.78	0.00	0.00	0.50
LZYGOMATICA θr	0.00	0.00	0.00	0.00	0.36	0.29	0.00	-0.30	0.00	0.00	0.31	0.00	0.00	0.00	0.00	0.00	0.00	0.00	0.00	0.00	0.00	0.00	0.00	0.00	0.39	0.00	0.00	0.00	0.78	0.00	0.00	0.50
LZYGOMATICB θr	0.00	0.00	0.00	0.00	0.36	0.29	0.00	-0.30	0.00	0.00	0.31	0.00	0.00	0.00	0.00	0.00	0.00	0.00	0.00	0.00	0.00	0.00	0.00	0.00	0.39	0.00	0.00	0.00	0.78	0.00	0.00	0.50

5.3 Design Optimization

The goal of the second hypothesis was to determine whether or not the material stiffness orientations present in various anatomical regions of the skull are such that the work expended by mastication is minimized. We set up a simple design optimization that allowed for the total elastic strain energy of the skull to be measured for various permutations of material stiffness orientations. A total elastic strain energy of 355.38 Joules was obtained when we ran the model using material stiffness orientations outlined in Table 5. However, when we investigated the total elastic strain energy measured from each of the 50 simulations run in the Probabilistic Design (Table 14), there were some configurations that resulted in less elastic strain energy. The difference in elastic strain energy was not substantial when examining the values achieved in the probabilistic design simulations. A range of 308.33 to 377.15 J was present when using the population standard deviations of the stiffness orientations for the eight input variables (Table 6). This suggests that there is a more optimal design (configuration of material stiffness orientations) if in fact the skull is designed to minimize elastic strain energy during chewing (feeding biomechanics). We examined how individual design variables (32 anatomical regions) affect the overall elastic strain energy. The right and left temporal regions were the only anatomical regions which had a significant correlation of material stiffness orientation to resulting elastic strain energy. These regions are two of the largest anatomical regions we defined (other than the parietal regions). The correlations of the left and right temporal regions (right: Figure 32) were opposite in sign because of the mirror effect of the rotation angles. The absolute values of the correlation coefficients were the same (r = 0.9406). The correlation of determination (R^2=0.8849) implies that

the strain energy is strongly and significantly correlated to principal material stiffness

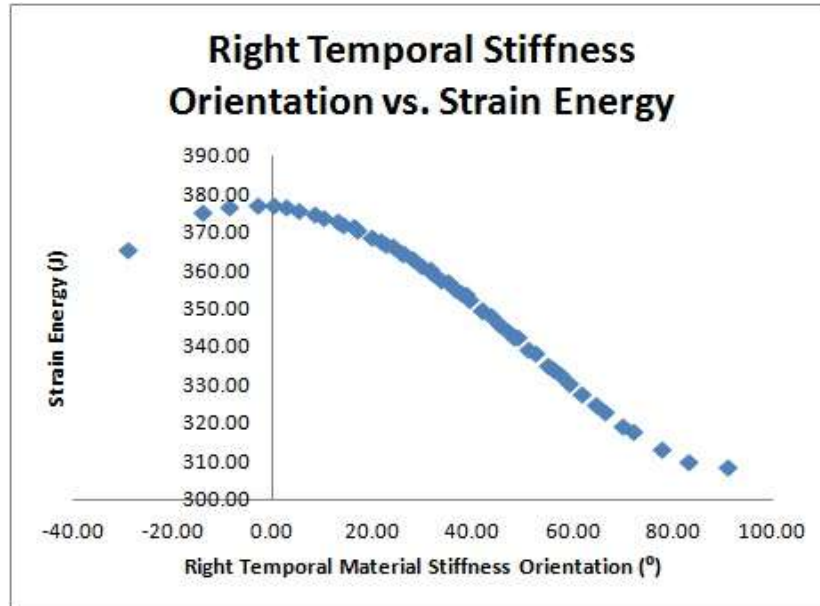orientation in the left and right temporal regions.

Figure 32: The effect of temporal stiffness orientation on elastic strain energy

Table 14 : Design Optimization (Design Variables: Stiffness Orientations-Degrees) and (Objective Function: Strain Energy-Joules)

THETA_RFMAXILLA	THETA_RPALETTE	THETA_RSMAXILLA	THETA_RORBITALA	THETA_RPARIETALA	THETA_RFRONTALB	THETA_RTEMPORALA	THETA_LZYGOMATICB	STRAINE
66.54	82.05	115.60	78.37	-0.95	53.08	91.21	17.84	308.33
-7.01	34.00	120.75	65.39	66.31	32.72	83.32	4.85	310.18
-60.25	-34.50	122.09	90.99	40.19	45.42	77.79	26.14	313.21
15.82	92.80	118.05	59.29	-10.75	14.40	72.06	5.99	317.69
-32.59	29.97	116.73	79.54	-21.68	28.79	70.13	31.30	319.37
65.12	27.47	117.46	89.28	100.50	69.04	66.38	10.80	323.23
86.24	71.51	119.03	97.46	52.37	25.48	64.69	28.64	324.78
-36.33	13.13	108.28	86.24	3.60	11.60	62.06	17.65	327.65
-43.22	43.42	117.11	64.63	115.03	5.06	59.53	25.14	330.35
-10.19	95.82	113.84	108.19	14.34	37.31	57.57	10.08	332.71
-41.04	22.98	119.59	83.77	81.55	45.27	56.06	14.32	334.31
3.50	15.51	121.75	94.24	-3.85	20.92	55.00	20.73	335.30
23.70	47.27	126.13	85.08	28.39	54.50	52.56	8.80	338.28
-25.57	54.03	122.56	107.82	137.98	32.13	51.31	8.38	339.52
55.48	48.31	105.11	118.18	33.85	48.92	49.02	23.02	342.41
25.65	31.86	137.66	67.52	74.19	38.22	48.50	27.99	342.73
38.75	57.35	112.73	69.14	92.84	58.26	47.40	13.21	344.14
35.02	58.42	114.74	75.93	131.05	49.79	45.44	27.17	346.06
59.28	100.75	110.29	103.56	142.87	47.22	43.63	34.12	348.14
30.95	45.73	118.42	76.18	91.83	19.97	42.06	18.98	349.67
27.86	68.34	123.53	82.12	103.58	34.37	41.92	23.45	349.81
10.03	79.88	133.51	49.57	45.80	35.99	39.39	16.40	352.30
92.08	107.40	101.72	98.31	78.09	23.28	38.61	38.32	353.69
48.43	64.14	107.50	72.81	36.72	18.75	37.77	21.34	354.14
95.41	110.98	121.16	74.03	84.52	27.54	36.44	24.50	355.38
19.91	26.78	135.26	71.11	5.69	35.68	35.09	40.55	356.85
71.54	-17.01	126.75	96.05	-12.70	43.21	33.79	13.82	357.74
52.53	1.84	129.15	100.84	58.21	25.01	31.97	17.10	359.43
33.85	121.75	113.20	77.66	22.22	47.93	31.44	15.63	360.15
-3.49	63.12	125.15	92.11	73.00	33.60	29.83	14.76	361.38
-12.04	17.52	120.31	91.63	87.03	31.28	27.90	25.37	363.08
13.06	87.78	143.25	90.10	64.05	30.88	26.13	33.49	364.60
-15.55	60.39	131.64	78.51	30.91	36.49	25.80	26.52	364.71
-68.39	37.05	119.83	81.60	111.55	41.36	-28.80	15.88	365.51
0.87	-6.33	110.95	80.51	25.37	62.85	24.06	20.45	366.21
-26.22	7.73	124.55	84.26	-16.69	30.06	22.58	2.08	367.08
43.75	68.13	130.32	83.12	120.88	16.08	21.52	29.23	367.77
-21.81	-0.62	125.54	72.32	148.15	42.36	19.71	21.51	368.84
-0.27	8.84	127.81	80.79	49.15	61.41	17.16	19.76	370.62
22.01	82.97	128.57	99.37	117.17	51.05	16.35	35.74	371.32
6.54	53.42	137.07	74.90	128.65	43.69	14.11	12.52	372.18
57.76	21.33	111.64	102.24	54.90	17.24	13.00	12.06	372.90
81.41	89.28	124.16	95.30	-27.36	28.44	10.08	29.93	374.06
-19.06	-12.83	131.87	86.97	96.00	22.38	8.56	22.81	374.72
-53.30	51.80	133.28	89.05	60.38	40.40	-13.95	18.43	375.09
45.83	72.94	116.20	97.11	11.22	26.45	5.40	24.01	375.85
109.47	38.46	126.21	87.59	42.98	7.90	2.61	27.83	376.44
77.10	124.59	129.96	92.90	69.51	38.90	-8.55	19.45	376.61
40.11	75.61	127.38	85.32	108.19	40.09	0.13	32.14	377.01
10.97	41.50	123.31	88.03	17.78	55.55	-2.88	21.99	377.15

84

CHAPTER 6

DISCUSSION & CONCLUSIONS

6.1 Study 1

The objective of Study 1 was to construct a specimen specific model of *Cebus apella, Curly*, and use *in vivo* experimental data to validate the FEM process. Only one other finite element model of a vertebrate species (*Macaca fascicularis,* another primate) has been properly validated using *in vivo* bone strain data. However the *Macaca* was not validated with individual-specific information. To our knowledge, this thesis presents the first and only complete in-vivo validation data set of a finite element model of a primate cranium. The results from Study 1 show that we are on the right track in validating the specimen specific model of *Curly.* The *in silico* results at three strain gage locations (right zygomatic arch, left anterior pillar, and right anterior pillar) prove to be in reasonable range of the *in vivo* data considering likelihood of error in a study of this magnitude. The isotropic and orthotropic models are both suitable within the expected error of such a complex model. This study has not only better validated the FEM process of a specimen specific primate crania, but has also validated the simplification methods used when modeling the alveolus region (Wood, S. A., et al., 2011). In addition, researchers can now be more confident in the FEM process and rely more heavily on the resulting stresses and strain present at a given instance during the mastication process. And furthermore, use the validated model to test hypotheses regarding the evolution of the skull due to mechanical adaptation.

Our orthotropic vs. isotropic modeling results are in agreement with (Strait, D. S., et al., 2005; Strait, D., et al., 2008) for the left and right anterior pillars. We believe that the *in silico* component strains were over estimated due to the use of overexposed EMG signals, improper segmentation of anatomical features, and assignment of orthotropic orientations. In the Materials and Methods section it was discussed that for each muscle in the craniofacial region the highest recorded strain was assigned a value of 1 and the rest of the resulting EMG signals were normalized with respect to that maximum value. EMG signals play a huge role when defining muscle forces used in feeding biomechanics. It is important to make sure that the in vivo data retrieved from EMG and strain gages are not over recorded. It is rare for a muscle to be fully activated (100%) during a normal activity such as feeding. Muscles are usually excited fully during extremely intense activities, or during unexpected moments of shock. We tried to make up for the over exposure of EMG signal by scaling down by an α-value discussed in the Results section above. This allowed for better agreement in the LPILL and RPILL regions for the orthotropic model. However, the RZARCH was still in favor of the isotropic model which may be due to improper segmentation and orthotropic material property assignment. Future work may include letting the α-values vary with each muscle group using an iterative method to minimize least square error and repeat the process until convergence.

Results from the isotropic and orthotropic models of Study 1 confirm conclusions made by (Wood, S. A., et al., 2011), indicating that the alveoli and periodontal ligaments have only local effects in craniofacial FEMs. Furthermore, modeling using isotropic versus orthotropic material properties does not significantly change the stress and strain

global patterns. Expanding on the conclusions of (Wood, S. A., et al., 2011), if the research goal is to understand global patterns of stress and strain, isotropic material properties will suffice. However if the research question is more localized, especially in the alveolus region, then it is recommended to use orthotropic material properties. Take note that orthotropic properties assigned were assumed to be homogeneous within each anatomical region with the principal material directions constant. In reality, principal material directions are constantly changing spatially as well as values of orthotropic material constants. The individual brick element strain results examined in Study 1 indicates that the strain results are very sensitive with regard to sampling location. This stresses the importance of properly documenting the location of implanted strain gage during *in vivo* and *in vitro* experiments. Better methods of superimposing this location onto an *in silico* specimen specific model are needed. In addition, more strain gage locations are needed in order to fully validate the skull. The material property data needs to be sampled in as many anatomical locations as possible. Due to the intense curvature of the skull these orientations change drastically from region to region so the more the skull can be split up the better. It seems that in regions of high curvature there needs to be more segmentation when assigning orthotropic material properties in order to get the outward normal vector correct. If a region of high curvature does not have enough data to be broken up in a reasonable amount of anatomical groups then it may be better to assign isotropic material properties to the skull in entirety. This is shown in Study 2, the areas with high curvature but not enough anatomical segmentation detail (RZARCH) resulted in the lower percent differences using the isotropic model. However for regions with well documented orthotropic data (LPILL and RPILL) and high curvature the results

show that using the orthotropic model will provide more accurate *in silico* results. Our lab is currently working on a piece of software that adjusts the orientations based upon the changing curvature of the skull. Computational time is an issue right now. If Study 2 is carried out again we suggest that when applying fixed and rotating coordinate systems make sure the right and left sides are fully mirrored to each other. Even if the z-axis is not outward normal (if it is pointing inwards) the E_{zz} will still be in the same direction and this will make the post processing far less complicated.

6.2 Study 2

From a global standpoint, the craniofacial results produced in Study 2 do not express a consistent trend between the material property stiffness orientation and maximum principal strain orientation that can be applied for every anatomical region, disagreeing with Hypothesis 1. Overall, the scatter plots for each anatomical region show very little change in maximum principal strain orientation with respect to stiffness orientation. The subtle variability tells us that the maximum principal strain orientations are not highly dependent on the stiffness orientations. Thus, it is believed that loading conditions and the geometry of the skull have a greater impact on the orientation of maximum principal strains rather than the stiffness orientations of orthotropic material. The strong correlations existing between maximum principal strains and material stiffness orientations in the highly defined brow region of the *Cebus apella* support this. The minute variations in maximum principal strain orientations with respect to substantial changes in material stiffness orientation are in disagreement with (Peterson, J., et al., 2003) and their hypothesis that grain in the cortical bone (material stiffness orientation) aligns in the direction of maximum stress. However, we observed several

dependencies of certain anatomical region's maximum principal strain orientations with respect to another region's material stiffness orientation. It turns out that moving from the posterior end of the cranium towards the anterior the variation in maximum principal strain orientation becomes more subtle. Thus, the location where results are being extracted will influence the necessary material property orientation precision of the model. Bright et al (2011) make note of the importance of sensitivity analyses and state "If the assumptions used to build the models are inaccurate, then the results will be inaccurate also". According to our results, the maximum principal strain orientations in posterior regions of the cranium are far more sensitive to variations in material stiffness orientation when compared to anterior regions closer to the loaded tooth. The decrease in variation of maximum principal strain orientation in the anterior portion of the cranium indicates that the precise of modeling material stiffness orientations is less important than we initially thought. However, the wide variations of maximum principal orientations in posterior regions of the skull suggest that it is more essential to model these regions with precise material stiffness orientations.

The results obtained in the design optimization portion of this thesis disagree with Hypothesis 2. It turns out that the work expended from mastication does not appear to be minimized with respect to a specimen's material stiffness orientations of the skull for the single masticating load scenario considered, i.e., left pre-molar biting. From the results uncovered in Study 2, there is potential for other orientations of material stiffness in various anatomical regions which produces lower total elastic strain energy. This poses the question, what is the optimality of the cranium? Are the material property orientations of various anatomical regions such that work expended during a bite with a

canine, perhaps for defense, is minimized? Investigating other biting situations and locations is essential for a proper design optimization of the cranium. We have only looked at one situation, unilateral chew using left upper premolar. Certain anatomical regions have more of an effect on total elastic strain energy than others. The material stiffness orientations of the temporal regions are significantly correlated with the resulting total elastic strain energy of the cranium during a LP3 chew. The material stiffness orientations of the temporal regions are parallel with the global force vector present during unilateral LP3 chewing. This suggests that the temporal regions were developed in the same orientation as a typical masticatory load. The strains present in the temporal regions are lower due to the load direction being parallel to the direction of maximum material stiffness (E1).

6.3 Conclusions

Validating a finite element model is essential in order to obtain precise and accurate results. The complexity and detail of a model is based upon the question the researcher wants to answer. In Study 1 we went through a series of validations to explore the necessary modeling features one needs to pay close attention to in a specimen specific model. Depending on the desired results (global versus local), it may be acceptable to model an orthotropic biological structure with isotropic material properties. The evolution of a species' anatomical features is reliant on many factors. With a properly validated model these factors can be investigated confidently through various finite element analyses. In Study 2 we uncovered that the relationship between material stiffness and maximum principal strain orientations is more localized and does not have a consistent global trend. Our results suggest that the maximum principal strain

orientations are more dependent on the geometry and location in the skull rather than the material stiffness orientation of a region. Furthermore, in Study 2 we discovered that the material stiffness orientations are not setup in a way that is optimal for feeding biomechanics from a minimization of strain energy perspective. Overall, many more biting/chewing situation will need to be investigated to fully understand the co-evolution of bone morphology and material properties in the facial skeleton.

APPENDIX A

DOCUMENTATION

A.I   University of Chicago Paperwork

Experiment Data Sheet
Callum Ross, Organismal Biology and Anatomy
University of Chicago

Date: ~~█~~ Revision Date: 2/9/8
Principal Investigator: Callum Ross
Assistants: ~~█~~
Experiment #: ~~█~~ 137
Species/ID: Cebus Apella ~~█~~ 911713

[3] - STRAIN GAGE

name of calibration file: c/17cal.b
Calibration switch: A/B 7

Gage type: delta
Number of gages: 1 2 3

Gage location:			Wire length:		
Element #	Bridge/Amp Channel		Channel	IGOR channel	
1	0	0		
2	1	1		
3	2	2		

Gage location:			Wire length:		
Element #	Bridge/Amp Channel		Channel	IGOR channel	
1	3	3		
2	4	4		
3	5	5		

Gage location:			Wire length:		
Element #	Bridge/Amp Channel		Channel	IGOR channel	
1	6	6		
2	7	7		
3	8	8		

Gage is OFF

Bridge Amp Settings:

SEQUENCES: 1-
Excitation: 2
Gain: 2 × 100
Filter: 1k

SEQUENCES:
Excitation
Gain
Filter

SEQUENCES:
Excitation
Gain
Filter

SEQUENCES:
Excitation
Gain
Filter

SEQUENCES:
Excitation
Gain
Filter

SEQUENCES:
Excitation
Gain
Filter

[ ] - EMG ELECTRODES

Plug Channel	Muscle	Grass Channel	Vicon Channel	Igor Channel
1 / 2		1	7	
3 / 4		2	8	
5 / 6		3	9	
7 / 8		4	10	
9 / 10		5	11	
11 / 12		6	12	
13 / 14		7	13	
15 / 16		8	14	
17		iso-gnd		
1 / 2		9	15	
3 / 4		10	16	
5 / 6		11	17	
7 / 8		12	18	
9 / 10		13	19	
11 / 12		14	20	
13 / 14		15	21	
15 / 16		16	22	
17		iso-gnd		

Muscle Stimulator Settings:

Train rate: 9.5x1 [tps]
Train duration: 5x1k [ms]
Stim rate: 5.5x10 [pps]
[ ] red switch [x] black switch

Delay: 0x0 [ms]
Duration: 10x10[ms]
Volts: 2.2x10 [v]

Link15 Settings:

SEQUENCES: 1-
Amp: 200   Range: 10k
Filters - Low: 30   High: 6k
Line: in / out

SEQUENCES:
Amp: Range:
Filters - Low: High:
Line: in / out

SEQUENCES:
Amp: Range:
Filters - Low: High:
Line: in / out

SEQUENCES:
Amp: Range:
Filters - Low: High:
Line: in out

SEQUENCES:
Amp: Range:
Filters - Low: High:
Line: in / out

SEQUENCES:
Amp: Range:
Filters - Low: High:
Line: in out

[X] – RADIOGRAPH

Fluoro:
Technique:
Sequence: 1-
MAS: KVP:
Sequence:
MAS: KVP:
Sequence:
MAS: KVP:

Sequence:
MAS: KVP:
Sequence:
MAS: KVP:
Sequence:
MAS: KVP:

Time of exposure: _____ [h:m:s]

Video sample rate:
Movie sample rate:
Analog data sample rate (Hz):

Experiment #: 737

VICON Seq#	Food	Pieces	Δ EMG settings	Δ page settings	Comments
1		1			
2		1			
3					
4		1			
5					
6		3			
7					
8		1			
9		1			
10					
11					
12					
13					
14					
15					
16					
17					
18					
19					
20					
21					
22					
23					
24					
25					
26					
27					
28					
29					
30					
31					
32					
33					
34					
35					
36					
37					
38					

93

Experiment Data Sheet
Callum Ross, Organismal Biology and Anatomy
University of Chicago

Date: 10/27/8
Principal Investigator: Callum Ross
Assistants: Jonathan Stopek, Jose Iriarte
Experiment #: 155
Species/ID: Curly

[3] - STRAIN GAGE

name of calibration file: _____
Calibration switch: A / B

Gage type: delta
Number of gages: 1 (2) 3

Gage location: left ant pillar			Wire length:
Element #	Bridge/Amp Channel	Vicon Channel	IGOR channel
1	b		
2	1		
3	2		

Gage location: right pillar			Wire length:
Element #	Bridge/Amp Channel	Vicon Channel	IGOR channel
1	3		
2	4		
3	5		

Gage location:			Wire length:
Element #	Bridge/Amp Channel	Vicon Channel	IGOR channel
1			
2			
3			

Bridge Amp Settings:

SEQUENCES: 1 -
Excitation: 2
Gain: 1x1k
Filter: 1k

SEQUENCES:
Excitation:
Gain:
Filter:

SEQUENCES:
Excitation:
Gain:
Filter:

SEQUENCES:
Excitation:
Gain:
Filter:

SEQUENCES:
Excitation:
Gain:
Filter:

SEQUENCES:
Excitation:
Gain:
Filter:

[yes] - EMG ELECTRODES

Plug Channel	Muscle	Grass Channel	Vicon Channel	Igor Channel
1/2	LSM	1	7	7
3/4	LAT	2	8	
5/6	LMPT	3	9	
7/8	L.DIG	4	10	15
9/10		5	11	
11/12		6	12	
13/14		7	13	
15/16		8	14	
17		iso-gnd		
1/2	RSM	9	15	
3/4	RAT	10	16	
5/6	RMPT	11	17	
7/8	R.DIG	12	18	
9/10		13	19	
11/12		14	20	
13/14		15	21	
15/16		16	22	
17		iso-gnd		

Muscle Stimulator Settings:

Train rate: 9.5x1 [tps]
Train duration: 5x1k [ms]
Stim rate: 5.5x10 [pps]
[ ] red switch [x] black switch

Delay: 0x0 [ms]
Duration: 10x10 [ms]
Volts: 2.2x10 [v]

94

Link15 Settings:

SEQUENCES: 1- *17*
Amp: ~~200~~ *10*   Range: 10k
Filters - Low: 30   High: 6k
Line: **in** / out

SEQUENCES: *18 –*
Amp: *5*   Range: *10k*
Filters - Low: *30*   High: *6k*
Line: in / out

SEQUENCES:
Amp: Range:
Filters - Low: High:
Line: in / out

[X] – RADIOGRAPH

Fluoro:
Technique:
Sequence: 1-
MAS: KVP: MAS:
Sequence:
MAS: KVP: MAS:
Sequence:
MAS: KVP: MAS:

Time of exposure: _____ [h:m:s]

Video sample rate: **50** ~~200~~ Hz
Movie sample rate: n/a
Analog data sample rate (Hz): ~~1000 Hz~~ **500**

Static:
Technique:
MAS:

Experiment #: 128

VICON Seq #	Food	Pieces	Δ EMG settings	Δ gage settings	Comments
1	hazelnut	1	0		break only
2	hazelnut	1	0		continues #1 break
3	hazelnut	1	0		break
4	walnut	1	ok		
5	apricot	1			
6	brazil nut	1	ok		break, chew
7	brazil nut	1	ok		
8	brazil nut	1	ok		continues #7 brazil nut
9	brazil nut	1	ok		left bits
10	brazil nut	1	ok		continues #9 a, b
11	pecan				left hand
12	pecan				right hand
13	prune pit(a)				
14	prune pit (a)				
15					
16					
17	apple				
18	dried mango				
19	gummi bear				
20	gummi bear				
21	pineapple				
22	hazelnut				crack
23	hazelnut				
24	walnut				
25					
26					
27					
28					
29					
30					
31					
32					
33					
34					
35					
36					
37					
38					

Experiment Data Sheet
Callum Ross, Organismal Biology and Anatomy
University of Chicago

Date: ...
Principal Investigator: Callum Ross
...
Experiment #: 30
Species: ...

[1] - STRAIN GAGE

Gage Type: ...
Number of gages: 3

Gage location:		Wire length (mm):	
Element #	Bridge/Amp Channel	Vicon Channel	IGOR channel
1	11	11	
2	12	12	
3	13	13	

Gage location:		wire length (mm):	
Element #	Bridge/Amp Channel	Vicon Channel	IGOR channel
1	21	14	
2	22	15	
3	23	16	

Gage location:		wire length (mm):	
Element #	Bridge/Amp Channel	Vicon Channel	IGOR channel
1	31	17	
2	32	18	
3	33	19	

Gage location:		wire length (mm):	
Element #	Bridge/Amp Channel	Vicon Channel	IGOR channel
1			
2			
3			

Bridge Amp Settings:

SEQUENCES: 1-
Excitation: 2
Gain: 1x1k
Filter: 1k

SEQUENCES:
Excitation:
Gain:
Filter:

SEQUENCES:
Excitation:
Gain:
Filter:

SEQUENCES:
Excitation:
Gain:
Filter:

SEQUENCES:
Excitation:
Gain:
Filter:

SEQUENCES:
Excitation:
Gain:
Filter:

[yes] - EMG ELECTRODES

Plug Channel	Muscle	Grass Channel	ADC Channel	Igor Channel
1 / 2	RSM, ANT.	1	1	
3 / 4	RDM	2	2	
5 / 6	RAT	15	3	
7 / 8	RPT	4	4	
9 / 10	RMPt	16	5	
11 / 12	RDig	6		
13 / 14		7		
15 / 16		8		
17		iso-gnd		
1 / 2	LSM - ANT	9	6	
3 / 4	RDM	10	7	
5 / 6	LAT	11	8	
7 / 8	LPT	12	9	
9 / 10	LMPt	13	10	
11 / 12	LDig	14		
13 / 14		15		
15 / 16		16		
17		iso-gnd		

Muscle Stimulator Settings:

Train rate: 9.5x1 [tps]
Train duration: 5x1k [ms]
Stim rate: 5.5x10 [pps]
10x10

Delay: 0x0 [ms]
Duration: 10x10[ms] 1x.1 ms
Volts: 2.2x10 [v]

Link15 Settings:

SEQUENCES: 1-ALL
Amp: 200 Range: 100
Filters - Low: 30 High: 6k
Line: **in** / out

SEQUENCES:
Amp: Range:
Filters - Low: High:
Line: in / out

SEQUENCES:
Amp: Range:
Filters - Low: High:
Line: in / out

SEQUENCES:
Amp: Range:
Filters - Low: High:
Line: in / out

SEQUENCES:
Amp: Range:
Filters - Low: High:
Line: in / out

SEQUENCES:
Amp: Range:
Filters - Low: High:
Line: in / out

[yes] – Kinematics:

Video sample rate: Hz
Movie sample rate: Hz
Analog data sample rate (Hz): Hz

[yes] – RADIOGRAPH

Technique:
MAS: KVP:

VICON Seq#	Food	Pieces	Δ EMG settings	Δ gage settings	Comments
1	Apple				
2	Almond shell				
3		1			
4	Walnut				
5	Almond shell	1			
6	Apricot				
7	Apple	1			
8	Hazelnut	1			
9	Brazil nut	1			NO GO
10	Walnut	1			
11	Almond shell	1			
12	Pecan	1			
13	Brazil nut	1			NO GO
14	Walnut				
15	Almond shell	1			
16		1			
17	Apricot	1			
18	Peach	1			
19	Date	1			
20	Brazil nut	1			NO GO
21	Almond shell	1			
22	Apricot	1			
23	Hazelnut	1			
24	Raisin	1			
25	Walnut	1			
26	Almond shell	1			NO GO
27	Carrot	1			
28		1			
29	Walnut	1			NO GO
30	Hazelnut	1			
31		1			
32	NO GO				NO GO
33					
34					

97

A.II   Specimen (Curly) Radiographs

Figure 33: Experiment 137, Curly Right Side Profile

Figure 34 : Experiment 137, Curly frontal profile

Figure 35: Experiment 155, Curly Left Side Profile

Figure 36: Experiment 155, Curly front profile

CUSTOM WRITTEN CODE

B.I   Igor batch code

```
**Experiment 201 IGOR Batch Code
**
**1. Import .txt or .cwg files or simply copy and paste data and column names
**2. Import calib_wave
**-->Data
**        -->Load waves
**                        -->Igor binary
**
**3.  Sort and Scale Strain and EMG data

Raw2UStrain6 ("strain1","strain2","strain3", "strain1","strain2","strain3")

Rename ch1_UStrain, rarch1; Rename ch2_UStrain, rarch2; ;DelayUpdate
Rename ch3_UStrain, rarch3;
killwaves ch4_UStrain;
killwaves ch5_UStrain
killwaves ch6_Ustrain


SetScale x, 0, numpnts(rarch1)/2000, rarch1
SetScale x, 0, numpnts(rarch1)/2000, rarch2
SetScale x, 0, numpnts(rarch1)/2000, rarch3

SetScale x, 0, numpnts(rarch1)/2000, RSM1
SetScale x, 0, numpnts(rarch1)/2000, RDMP2
SetScale x, 0, numpnts(rarch1)/2000, RAT7
SetScale x, 0, numpnts(rarch1)/2000, RPT8
SetScale x, 0, numpnts(rarch1)/2000, RMPT9
SetScale x, 0, numpnts(rarch1)/2000, RDIG10

SetScale x, 0, numpnts(rarch1)/2000, LSMA11
SetScale x, 0, numpnts(rarch1)/2000, LDMP12
SetScale x, 0, numpnts(rarch1)/2000, LAT13
SetScale x, 0, numpnts(rarch1)/2000, LPT14
SetScale x, 0, numpnts(rarch1)/2000, LMPT15
SetScale x, 0, numpnts(rarch1)/2000, LDIG16

ButtLow("rarch1",40,15)
SetScale x, numpnts(rarch1)/2000, 0, rarch1
ButtLow("rarch1",40,15)
SetScale x, 0, numpnts(rarch1)/2000, rarch1

ButtLow("rarch2",40,15)
SetScale x, numpnts(rarch2)/2000, 0, rarch2
ButtLow("rarch2",40,15)
SetScale x, 0, numpnts(rarch2)/2000, rarch2

ButtLow("rarch3",40,15)
SetScale x, numpnts(rarch3)/2000, 0, rarch3
ButtLow("rarch3",40,15)
```

SetScale x, 0, numpnts(rarch3)/2000, rarch3

**4. DECIMATE STRAINS

Decimate("rarch1","rarch2","rarch3","rarch1d","rarch2d","rarch3d",5)

**5. CALCULATE PRINCIPAL STRAINS, creating a new wave "RARCH", do this for each strain gauge

Display rarch1, rarch2, rarch3
Principal_Strain_ToolsD()

** 6. PREPROCESS EMG SIGNALS, make sure sampling frequency in macro corresponds to paperwork

PreProcessAll4("RSM1","RDMP2","RAT7","RPT8")
PreProcessAll4("RMPT9","RDIG10","LSMA11","LDMP12")
PreProcessAll4("LAT13","LPT14","LMPT15","LDIG16")

**7. MAKE DEF WAVES, by selecting PStart and Pend in drop down menus, once you have recorded enough chews/bites click "finish"

Display Max_StrainRARCH,Max_StrainRARCH; AppendToGraph/R
RSM1P,RDMP2P,RAT7P,RPT8P,RMPT9P,LSMA11P,LDMP12P,LAT13P,LPT14P,LMPT15P
ModifyGraph rgb(Max_StrainRARCH)=(0,12800,52224),rgb(Max_StrainRARCH)=(0,0,0)
DefPowStrokes()

**7. EXTRACT DATA: shear, min/max strain, and strain orientation.   In addition to EMG peak values and positions.

EX7ptsStrain("Shr_StrainRARCH","Max_StrainRARCH","Min_StrainRARCH","ElA_to_PmaxRARCH",
"Pstart","Pend")
EX7ptsEMG("RSM1P","RDMP2P","RAT7P","RPT8P","Pstart","Pend")
EX7ptsEMG("RMPT9P","RDIG10P","LSMA11P","LDMP12P","Pstart","Pend")
EX7ptsEMG("LAT13P","LPT14P","LMPT15P","LDIG16P","Pstart","Pend")

** CREATE DATA TABLES

AppendToTable Shr_StrainRARCHpkpos75u,Shr_StrainRARCHpkpos;DelayUpdate
AppendToTable Shr_StrainRARCHpkpos75d,Shr_StrainRARCHpkpos50d;DelayUpdate
AppendToTable Shr_StrainRARCHpkpos25d,Max_StrainRARCHpkval;DelayUpdate
AppendToTable Max_StrainRARCHpkpos25u,Max_StrainRARCHpkpos50u;DelayUpdate
AppendToTable Max_StrainRARCHpkpos75u,Max_StrainRARCHpkpos;DelayUpdate
AppendToTable Max_StrainRARCHpkpos75d,Max_StrainRARCHpkpos50d;DelayUpdate
AppendToTable Max_StrainRARCHpkpos25d,Min_StrainRARCHpkval;DelayUpdate
AppendToTable Min_StrainRARCHpkpos25u,Min_StrainRARCHpkpos50u;DelayUpdate
AppendToTable Min_StrainRARCHpkpos75u,Min_StrainRARCHpkpos;DelayUpdate
AppendToTable Min_StrainRARCHpkpos75d,Min_StrainRARCHpkpos50d;DelayUpdate
AppendToTable
Min_StrainRARCHpkpos25d,ElA_to_PmaxRARCHsh25u,ElA_to_PmaxRARCHsh50u;DelayUpdate
AppendToTable
ElA_to_PmaxRARCHsh75u,ElA_to_PmaxRARCHangpk,ElA_to_PmaxRARCHsh75d;DelayUpdate
AppendToTable ElA_to_PmaxRARCHsh50d,ElA_to_PmaxRARCHsh25d,RSM1Ppkval;DelayUpdate
AppendToTable
'RSM1Ppkpos@25u','RSM1Ppkpos@50u','RSM1Ppkpos@75u',RSM1Ppkpos;DelayUpdate
AppendToTable
'RSM1Ppkpos@75d','RSM1Ppkpos@50d','RSM1Ppkpos@25d',RDMP2Ppkval;DelayUpdate

```
AppendToTable
'RDMP2Ppkpos@25u','RDMP2Ppkpos@50u','RDMP2Ppkpos@75u',RDMP2Ppkpos;DelayUpdate
AppendToTable
'RDMP2Ppkpos@75d','RDMP2Ppkpos@50d','RDMP2Ppkpos@25d',RAT7Ppkval;DelayUpdate
AppendToTable
'RAT7Ppkpos@25u','RAT7Ppkpos@50u','RAT7Ppkpos@75u',RAT7Ppkpos;DelayUpdate
AppendToTable 'RAT7Ppkpos@75d','RAT7Ppkpos@50d','RAT7Ppkpos@25d',RPT8Ppkval;DelayUpdate
AppendToTable 'RPT8Ppkpos@25u','RPT8Ppkpos@50u','RPT8Ppkpos@75u',RPT8Ppkpos;DelayUpdate
AppendToTable
'RPT8Ppkpos@75d','RPT8Ppkpos@50d','RPT8Ppkpos@25d',RMPT9Ppkval;DelayUpdate
AppendToTable
'RMPT9Ppkpos@25u','RMPT9Ppkpos@50u','RMPT9Ppkpos@75u',RMPT9Ppkpos;DelayUpdate
AppendToTable
'RMPT9Ppkpos@75d','RMPT9Ppkpos@50d','RMPT9Ppkpos@25d',RDIG10Ppkval;DelayUpdate
AppendToTable 'RDIG10Ppkpos@25u','RDIG10Ppkpos@50u','RDIG10Ppkpos@75u';DelayUpdate
AppendToTable RDIG10Ppkpos,'RDIG10Ppkpos@75d','RDIG10Ppkpos@50d';DelayUpdate
AppendToTable 'RDIG10Ppkpos@25d',LSMA11Ppkval,'LSMA11Ppkpos@25u';DelayUpdate
AppendToTable 'LSMA11Ppkpos@50u','LSMA11Ppkpos@75u',LSMA11Ppkpos;DelayUpdate
AppendToTable 'LSMA11Ppkpos@75d','LSMA11Ppkpos@50d','LSMA11Ppkpos@25d';DelayUpdate
AppendToTable LDMP12Ppkval,'LDMP12Ppkpos@25u','LDMP12Ppkpos@50u';DelayUpdate
AppendToTable 'LDMP12Ppkpos@75u',LDMP12Ppkpos,'LDMP12Ppkpos@75d';DelayUpdate
AppendToTable
'LDMP12Ppkpos@50d','LDMP12Ppkpos@25d',LAT13Ppkval,'LAT13Ppkpos@25u';DelayUpdate
AppendToTable
'LAT13Ppkpos@50u','LAT13Ppkpos@75u',LAT13Ppkpos,'LAT13Ppkpos@75d';DelayUpdate
AppendToTable
'LAT13Ppkpos@50d','LAT13Ppkpos@25d',LPT14Ppkval,'LPT14Ppkpos@25u';DelayUpdate
AppendToTable
'LPT14Ppkpos@50u','LPT14Ppkpos@75u',LPT14Ppkpos,'LPT14Ppkpos@75d';DelayUpdate
AppendToTable
'LPT14Ppkpos@50d','LPT14Ppkpos@25d',LMPT15Ppkval,'LMPT15Ppkpos@25u';DelayUpdate
AppendToTable 'LMPT15Ppkpos@50u','LMPT15Ppkpos@75u',LMPT15Ppkpos;DelayUpdate
AppendToTable 'LMPT15Ppkpos@75d','LMPT15Ppkpos@50d','LMPT15Ppkpos@25d';DelayUpdate
AppendToTable LDIG16Ppkval,'LDIG16Ppkpos@25u','LDIG16Ppkpos@50u';DelayUpdate
AppendToTable 'LDIG16Ppkpos@75u',LDIG16Ppkpos,'LDIG16Ppkpos@75d';DelayUpdate
AppendToTable 'LDIG16Ppkpos@50d','LDIG16Ppkpos@25d'
```

B.II   APDL Probabilistic Design batch code

```
resume
/prep7

cmsel,all
nsle,s

!sets the material property axis to Paul's data

theta_LFMAXILLA=180-theta_RFMAXILLA
theta_LPALETTE=180-theta_RPALETTE
theta_LSMAXILLA=180-theta_RSMAXILLA
theta_RORBITALD=90+theta_RORBITALA
theta_RORBITALB=theta_RORBITALD
theta_RORBITALC=theta_RORBITALA

theta_LORBITALD=180-theta_RORBITALD
theta_LORBITALA=180-theta_RORBITALA
theta_LORBITALC=180-theta_RORBITALB
theta_LORBITALB=180-theta_RORBITALC
theta_RPARIETALB=theta_RPARIETALA
theta_RPARIETALC=theta_RPARIETALA
theta_LPARIETALA=90-theta_RPARIETALA
theta_LPARIETALB=90-theta_RPARIETALA
theta_LPARIETALC=90-theta_RPARIETALA
theta_RFRONTALA=theta_RFRONTALB
theta_LFRONTALB=180-theta_RFRONTALB
theta_LFRONTALA=180-theta_RFRONTALB
theta_RTEMPORALB=theta_RTEMPORALA
```

theta_LTEMPORALA=180-
theta_RTEMPORALA
theta_LTEMPORALB=180-
theta_RTEMPORALA
theta_LSPHENOID=180-theta_RSPHENOID
theta_LZYGOMATICA=theta_LZYGOMATIC
B
theta_RZYGOMATICA=90+theta_LZYGOMA
TICB
theta_RZYGOMATICB=90+theta_LZYGOMA
TICB

!assigns rotating coordinate systems
CSys,11
wpave,0,0,0
Clocal,111,0,0,0,0,theta_RFMAXILLA,0,0
CMSEL,S,RFMAXILLA
CSys,111
wpave,0,0,0
nsle,s
emodif,all,esys,111

CSys,12
wpave,0,0,0
Clocal,112,0,0,0,0,theta_LFMAXILLA,0,0
CMSEL,S,LFMAXILLA
CSys,112
wpave,0,0,0
nsle,s
emodif,all,esys,112

CSys,13
wpave,0,0,0
Clocal,113,0,0,0,0,theta_RPALETTE,0,0
CMSEL,S,RPALETTE
CSys,113
wpave,0,0,0
nsle,s
emodif,all,esys,113

CSys,14
wpave,0,0,0
Clocal,114,0,0,0,0,theta_LPALETTE,0,0
CMSEL,S,LPALETTE
CSys,114
wpave,0,0,0
nsle,s
emodif,all,esys,114

CSys,15
wpave,0,0,0
Clocal,115,0,0,0,0,theta_RSMAXILLA,0,0
CMSEL,S,RSMAXILLA
CSys,115
wpave,0,0,0
nsle,s

emodif,all,esys,115

CSys,16
wpave,0,0,0
Clocal,116,0,0,0,0,theta_LSMAXILLA,0,0
CMSEL,S,LSMAXILLA
CSys,116
wpave,0,0,0
nsle,s
emodif,all,esys,116

CSys,17
wpave,0,0,0
Clocal,117,0,0,0,0,theta_RORBITALD,0,0
CMSEL,S,RORBITALD
CSys,117
wpave,0,0,0
nsle,s
emodif,all,esys,117

CSys,18
wpave,0,0,0
Clocal,118,0,0,0,0,theta_RORBITALA,0,0
CMSEL,S,RORBITALA
CSys,118
wpave,0,0,0
nsle,s
emodif,all,esys,118

CSys,19
wpave,0,0,0
Clocal,119,0,0,0,0,theta_RORBITALB,0,0
CMSEL,S,RORBITALB
CSys,119
wpave,0,0,0
nsle,s
emodif,all,esys,119

CSys,20
wpave,0,0,0
Clocal,120,0,0,0,0,theta_RORBITALC,0,0
CMSEL,S,RORBITALC
CSys,120
wpave,0,0,0
nsle,s
emodif,all,esys,120

CSys,21
wpave,0,0,0
Clocal,121,0,0,0,0,theta_LORBITALD,0,0
CMSEL,S,LORBITALD
CSys,121
wpave,0,0,0
nsle,s
emodif,all,esys,121

```
CSys,22
wpave,0,0,0
Clocal,122,0,0,0,0,theta_LORBITALA,0,0
CMSEL,S,LORBITALA
CSys,122
wpave,0,0,0
nsle,s
emodif,all,esys,122

CSys,23
wpave,0,0,0
Clocal,123,0,0,0,0,theta_LORBITALC,0,0
CMSEL,S,LORBITALC
CSys,123
wpave,0,0,0
nsle,s
emodif,all,esys,123

CSys,24
wpave,0,0,0
Clocal,124,0,0,0,0,theta_LORBITALB,0,0
CMSEL,S,LORBITALB
CSys,124
wpave,0,0,0
nsle,s
emodif,all,esys,124

CSys,25
wpave,0,0,0
Clocal,125,0,0,0,0,theta_RPARIETALA,0,0
CMSEL,S,RPARIETALA
CSys,125
wpave,0,0,0
nsle,s
emodif,all,esys,125

CSys,26
wpave,0,0,0
Clocal,126,0,0,0,0,theta_RPARIETALB,0,0
CMSEL,S,RPARIETALB
CSys,126
wpave,0,0,0
nsle,s
emodif,all,esys,126

CSys,27
wpave,0,0,0
Clocal,127,0,0,0,0,theta_RPARIETALC,0,0
CMSEL,S,RPARIETALC
CSys,127
wpave,0,0,0
nsle,s
emodif,all,esys,127

CSys,28
wpave,0,0,0

Clocal,128,0,0,0,0,theta_LPARIETALA,0,0
CMSEL,S,LPARIETALA
CSys,128
wpave,0,0,0
nsle,s
emodif,all,esys,128

CSys,29
wpave,0,0,0
Clocal,129,0,0,0,0,theta_LPARIETALB,0,0
CMSEL,S,LPARIETALB
CSys,129
wpave,0,0,0
nsle,s
emodif,all,esys,129

CSys,30
wpave,0,0,0
Clocal,130,0,0,0,0,theta_LPARIETALC,0,0
CMSEL,S,LPARIETALC
CSys,130
wpave,0,0,0
nsle,s
emodif,all,esys,130

CSys,31
wpave,0,0,0
Clocal,131,0,0,0,0,theta_RFRONTALB,0,0
CMSEL,S,RFRONTALB
CSys,131
wpave,0,0,0
nsle,s
emodif,all,esys,131

CSys,32
wpave,0,0,0
Clocal,132,0,0,0,0,theta_RFRONTALA,0,0
CMSEL,S,RFRONTALA
CSys,132
wpave,0,0,0
nsle,s
emodif,all,esys,132

CSys,33
wpave,0,0,0
Clocal,133,0,0,0,0,theta_LFRONTALB,0,0
CMSEL,S,LFRONTALB
CSys,133
wpave,0,0,0
nsle,s
emodif,all,esys,133

CSys,34
wpave,0,0,0
Clocal,134,0,0,0,0,theta_LFRONTALA,0,0
CMSEL,S,LFRONTALA
```

```
CSys,134
wpave,0,0,0
nsle,s
emodif,all,esys,134

CSys,35
wpave,0,0,0
Clocal,135,0,0,0,0,theta_RTEMPORALA,0,0
CMSEL,S,RTEMPORALA
CSys,135
wpave,0,0,0
nsle,s
emodif,all,esys,135

CSys,36
wpave,0,0,0
Clocal,136,0,0,0,0,theta_RTEMPORALB,0,0
CMSEL,S,RTEMPORALB
CSys,136
wpave,0,0,0
nsle,s
emodif,all,esys,136

CSys,37
wpave,0,0,0
Clocal,137,0,0,0,0,theta_LTEMPORALA,0,0
CMSEL,S,LTEMPORALA
CSys,137
wpave,0,0,0
nsle,s
emodif,all,esys,137

CSys,38
wpave,0,0,0
Clocal,138,0,0,0,0,theta_LTEMPORALB,0,0
CMSEL,S,LTEMPORALB
CSys,138
wpave,0,0,0
nsle,s
emodif,all,esys,138

CSys,39
wpave,0,0,0
Clocal,139,0,0,0,0,theta_RSPHENOID,0,0
CMSEL,S,RSPHENOID
CSys,139
wpave,0,0,0
nsle,s
emodif,all,esys,139

CSys,40
wpave,0,0,0
Clocal,140,0,0,0,0,theta_LSPHENOID,0,0
CMSEL,S,LSPHENOID
CSys,140
wpave,0,0,0
```

```
nsle,s
emodif,all,esys,140

CSys,41
wpave,0,0,0
Clocal,141,0,0,0,0,theta_RZYGOMATICA,0,0
CMSEL,S,RZYGOMATICA
CSys,141
wpave,0,0,0
nsle,s
emodif,all,esys,141

CSys,42
wpave,0,0,0
Clocal,142,0,0,0,0,theta_RZYGOMATICB,0,0
CMSEL,S,RZYGOMATICB
CSys,142
wpave,0,0,0
nsle,s
emodif,all,esys,142

CSys,43
wpave,0,0,0
Clocal,143,0,0,0,0,theta_LZYGOMATICB,0,0
CMSEL,S,LZYGOMATICB
CSys,143
wpave,0,0,0
nsle,s
emodif,all,esys,143

CSys,44
wpave,0,0,0
Clocal,144,0,0,0,0,theta_LZYGOMATICA,0,0
CMSEL,S,LZYGOMATICA
CSys,144
wpave,0,0,0
nsle,s
emodif,all,esys,144

!defines results CS for rzyg arch
CSys,41
wpave,0,0,0
Clocal,145,0,0,0,0,161,0,0

CSys,0
wpave,0,0,0
cmsel,all
nsle,s
finish

!solves the model with respect to input variables

/solu
solve
finish
```

```
!retrieves results

/post1
set,last

rsys,11
*Get,RFMAXILLA_Emax,node,146920,epto,1
*Get,RFMAXILLA_Emin,node,146920,epto,3
*Get,RFMAXILLA_Ex,node,146920,epto,x
*Get,RFMAXILLA_Ey,node,146920,epto,y
*Get,RFMAXILLA_Exy,node,146920,epto,xy
*Get,RFMAXILLA_Smax,node,146920,s,1
*Get,RFMAXILLA_Smin,node,146920,s,3
*Get,RFMAXILLA_Sx,node,146920,s,x
*Get,RFMAXILLA_Sy,node,146920,s,y
*Get,RFMAXILLA_Sxy,node,146920,s,xy


rsys,12
*Get,LFMAXILLA_Emax,node,63273,epto,1
*Get,LFMAXILLA_Emin,node,63273,epto,3
*Get,LFMAXILLA_Ex,node,63273,epto,x
*Get,LFMAXILLA_Ey,node,63273,epto,y
*Get,LFMAXILLA_Exy,node,63273,epto,xy
*Get,LFMAXILLA_Smax,node,63273,s,1
*Get,LFMAXILLA_Smin,node,63273,s,3
*Get,LFMAXILLA_Sx,node,63273,s,x
*Get,LFMAXILLA_Sy,node,63273,s,y
*Get,LFMAXILLA_Sxy,node,63273,s,xy


rsys,13
*Get,RPALETTE_Emax,node,85857,epto,1
*Get,RPALETTE_Emin,node,85857,epto,3
*Get,RPALETTE_Ex,node,85857,epto,x
*Get,RPALETTE_Ey,node,85857,epto,y
*Get,RPALETTE_Exy,node,85857,epto,xy
*Get,RPALETTE_Smax,node,85857,s,1
*Get,RPALETTE_Smin,node,85857,s,3
*Get,RPALETTE_Sx,node,85857,s,x
*Get,RPALETTE_Sy,node,85857,s,y
*Get,RPALETTE_Sxy,node,85857,s,xy


rsys,14
*Get,LPALETTE_Emax,node,108908,epto,1
*Get,LPALETTE_Emin,node,108908,epto,3
*Get,LPALETTE_Ex,node,108908,epto,x
*Get,LPALETTE_Ey,node,108908,epto,y
*Get,LPALETTE_Exy,node,108908,epto,xy
*Get,LPALETTE_Smax,node,108908,s,1
*Get,LPALETTE_Smin,node,108908,s,3
*Get,LPALETTE_Sx,node,108908,s,x
*Get,LPALETTE_Sy,node,108908,s,y
*Get,LPALETTE_Sxy,node,108908,s,xy


rsys,15
*Get,RSMAXILLA_Emax,node,53131,epto,1
*Get,RSMAXILLA_Emin,node,53131,epto,3

*Get,RSMAXILLA_Ex,node,53131,epto,x
*Get,RSMAXILLA_Ey,node,53131,epto,y
*Get,RSMAXILLA_Exy,node,53131,epto,xy
*Get,RSMAXILLA_Smax,node,53131,s,1
*Get,RSMAXILLA_Smin,node,53131,s,3
*Get,RSMAXILLA_Sx,node,53131,s,x
*Get,RSMAXILLA_Sy,node,53131,s,y
*Get,RSMAXILLA_Sxy,node,53131,s,xy


rsys,16
*Get,LSMAXILLA_Emax,node,68447,epto,1
*Get,LSMAXILLA_Emin,node,68447,epto,3
*Get,LSMAXILLA_Ex,node,68447,epto,x
*Get,LSMAXILLA_Ey,node,68447,epto,y
*Get,LSMAXILLA_Exy,node,68447,epto,xy
*Get,LSMAXILLA_Smax,node,68447,s,1
*Get,LSMAXILLA_Smin,node,68447,s,3
*Get,LSMAXILLA_Sx,node,68447,s,x
*Get,LSMAXILLA_Sy,node,68447,s,y
*Get,LSMAXILLA_Sxy,node,68447,s,xy


rsys,17
*Get,RORBITALD_Emax,node,50946,epto,1
*Get,RORBITALD_Emin,node,50946,epto,3
*Get,RORBITALD_Ex,node,50946,epto,x
*Get,RORBITALD_Ey,node,50946,epto,y
*Get,RORBITALD_Exy,node,50946,epto,xy
*Get,RORBITALD_Smax,node,50946,s,1
*Get,RORBITALD_Smin,node,50946,s,3
*Get,RORBITALD_Sx,node,50946,s,x
*Get,RORBITALD_Sy,node,50946,s,y
*Get,RORBITALD_Sxy,node,50946,s,xy


rsys,18
*Get,RORBITALA_Emax,node,83112,epto,1
*Get,RORBITALA_Emin,node,83112,epto,3
*Get,RORBITALA_Ex,node,83112,epto,x
*Get,RORBITALA_Ey,node,83112,epto,y
*Get,RORBITALA_Exy,node,83112,epto,xy
*Get,RORBITALA_Smax,node,83112,s,1
*Get,RORBITALA_Smin,node,83112,s,3
*Get,RORBITALA_Sx,node,83112,s,x
*Get,RORBITALA_Sy,node,83112,s,y
*Get,RORBITALA_Sxy,node,83112,s,xy


rsys,19
*Get,RORBITALB_Emax,node,125687,epto,1
*Get,RORBITALB_Emin,node,125687,epto,3
*Get,RORBITALB_Ex,node,125687,epto,x
*Get,RORBITALB_Ey,node,125687,epto,y
*Get,RORBITALB_Exy,node,125687,epto,xy
*Get,RORBITALB_Smax,node,125687,s,1
*Get,RORBITALB_Smin,node,125687,s,3
*Get,RORBITALB_Sx,node,125687,s,x
*Get,RORBITALB_Sy,node,125687,s,y
*Get,RORBITALB_Sxy,node,125687,s,xy
```

```
rsys,20
*Get,RORBITALC_Emax,node,23122,epto,1
*Get,RORBITALC_Emin,node,23122,epto,3
*Get,RORBITALC_Ex,node,23122,epto,x
*Get,RORBITALC_Ey,node,23122,epto,y
*Get,RORBITALC_Exy,node,23122,epto,xy
*Get,RORBITALC_Smax,node,23122,s,1
*Get,RORBITALC_Smin,node,23122,s,3
*Get,RORBITALC_Sx,node,23122,s,x
*Get,RORBITALC_Sy,node,23122,s,y
*Get,RORBITALC_Sxy,node,23122,s,xy

rsys,21
*Get,LORBITALD_Emax,node,65556,epto,1
*Get,LORBITALD_Emin,node,65556,epto,3
*Get,LORBITALD_Ex,node,65556,epto,x
*Get,LORBITALD_Ey,node,65556,epto,y
*Get,LORBITALD_Exy,node,65556,epto,xy
*Get,LORBITALD_Smax,node,65556,s,1
*Get,LORBITALD_Smin,node,65556,s,3
*Get,LORBITALD_Sx,node,65556,s,x
*Get,LORBITALD_Sy,node,65556,s,y
*Get,LORBITALD_Sxy,node,65556,s,xy

rsys,22
*Get,LORBITALA_Emax,node,148319,epto,1
*Get,LORBITALA_Emin,node,148319,epto,3
*Get,LORBITALA_Ex,node,148319,epto,x
*Get,LORBITALA_Ey,node,148319,epto,y
*Get,LORBITALA_Exy,node,148319,epto,xy
*Get,LORBITALA_Smax,node,148319,s,1
*Get,LORBITALA_Smin,node,148319,s,3
*Get,LORBITALA_Sx,node,148319,s,x
*Get,LORBITALA_Sy,node,148319,s,y
*Get,LORBITALA_Sxy,node,148319,s,xy

rsys,23
*Get,LORBITALC_Emax,node,123573,epto,1
*Get,LORBITALC_Emin,node,123573,epto,3
*Get,LORBITALC_Ex,node,123573,epto,x
*Get,LORBITALC_Ey,node,123573,epto,y
*Get,LORBITALC_Exy,node,123573,epto,xy
*Get,LORBITALC_Smax,node,123573,s,1
*Get,LORBITALC_Smin,node,123573,s,3
*Get,LORBITALC_Sx,node,123573,s,x
*Get,LORBITALC_Sy,node,123573,s,y
*Get,LORBITALC_Sxy,node,123573,s,xy

rsys,24
*Get,LORBITALB_Emax,node,75480,epto,1
*Get,LORBITALB_Emin,node,75480,epto,3
*Get,LORBITALB_Ex,node,75480,epto,x
*Get,LORBITALB_Ey,node,75480,epto,y
*Get,LORBITALB_Exy,node,75480,epto,xy
*Get,LORBITALB_Smax,node,75480,s,1
```

```
*Get,LORBITALB_Smin,node,75480,s,3
*Get,LORBITALB_Sx,node,75480,s,x
*Get,LORBITALB_Sy,node,75480,s,y
*Get,LORBITALB_Sxy,node,75480,s,xy

rsys,25
*Get,RPARIETALA_Emax,node,5311,epto,1
*Get,RPARIETALA_Emin,node,5311,epto,3
*Get,RPARIETALA_Ex,node,5311,epto,x
*Get,RPARIETALA_Ey,node,5311,epto,y
*Get,RPARIETALA_Exy,node,5311,epto,xy
*Get,RPARIETALA_Smax,node,5311,s,1
*Get,RPARIETALA_Smin,node,5311,s,3
*Get,RPARIETALA_Sx,node,5311,s,x
*Get,RPARIETALA_Sy,node,5311,s,y
*Get,RPARIETALA_Sxy,node,5311,s,xy

rsys,26
*Get,RPARIETALB_Emax,node,10262,epto,1
*Get,RPARIETALB_Emin,node,10262,epto,3
*Get,RPARIETALB_Ex,node,10262,epto,x
*Get,RPARIETALB_Ey,node,10262,epto,y
*Get,RPARIETALB_Exy,node,10262,epto,xy
*Get,RPARIETALB_Smax,node,10262,s,1
*Get,RPARIETALB_Smin,node,10262,s,3
*Get,RPARIETALB_Sx,node,10262,s,x
*Get,RPARIETALB_Sy,node,10262,s,y
*Get,RPARIETALB_Sxy,node,10262,s,xy

rsys,27
*Get,RPARIETALC_Emax,node,98668,epto,1
*Get,RPARIETALC_Emin,node,98668,epto,3
*Get,RPARIETALC_Ex,node,98668,epto,x
*Get,RPARIETALC_Ey,node,98668,epto,y
*Get,RPARIETALC_Exy,node,98668,epto,xy
*Get,RPARIETALC_Smax,node,98668,s,1
*Get,RPARIETALC_Smin,node,98668,s,3
*Get,RPARIETALC_Sx,node,98668,s,x
*Get,RPARIETALC_Sy,node,98668,s,y
*Get,RPARIETALC_Sxy,node,98668,s,xy

rsys,28
*Get,LPARIETALA_Emax,node,4633,epto,1
*Get,LPARIETALA_Emin,node,4633,epto,3
*Get,LPARIETALA_Ex,node,4633,epto,x
*Get,LPARIETALA_Ey,node,4633,epto,y
*Get,LPARIETALA_Exy,node,4633,epto,xy
*Get,LPARIETALA_Smax,node,4633,s,1
*Get,LPARIETALA_Smin,node,4633,s,3
*Get,LPARIETALA_Sx,node,4633,s,x
*Get,LPARIETALA_Sy,node,4633,s,y
*Get,LPARIETALA_Sxy,node,4633,s,xy

rsys,29
*Get,LPARIETALB_Emax,node,2195,epto,1
*Get,LPARIETALB_Emin,node,2195,epto,3
```

*Get,LPARIETALB_Ex,node,2195,epto,x
*Get,LPARIETALB_Ey,node,2195,epto,y
*Get,LPARIETALB_Exy,node,2195,epto,xy
*Get,LPARIETALB_Smax,node,2195,s,1
*Get,LPARIETALB_Smin,node,2195,s,3
*Get,LPARIETALB_Sx,node,2195,s,x
*Get,LPARIETALB_Sy,node,2195,s,y
*Get,LPARIETALB_Sxy,node,2195,s,xy

rsys,30
*Get,LPARIETALC_Emax,node,5352,epto,1
*Get,LPARIETALC_Emin,node,5352,epto,3
*Get,LPARIETALC_Ex,node,5352,epto,x
*Get,LPARIETALC_Ey,node,5352,epto,y
*Get,LPARIETALC_Exy,node,5352,epto,xy
*Get,LPARIETALC_Smax,node,5352,s,1
*Get,LPARIETALC_Smin,node,5352,s,3
*Get,LPARIETALC_Sx,node,5352,s,x
*Get,LPARIETALC_Sy,node,5352,s,y
*Get,LPARIETALC_Sxy,node,5352,s,xy

rsys,31
*Get,RFRONTALB_Emax,node,109782,epto,1
*Get,RFRONTALB_Emin,node,109782,epto,3
*Get,RFRONTALB_Ex,node,109782,epto,x
*Get,RFRONTALB_Ey,node,109782,epto,y
*Get,RFRONTALB_Exy,node,109782,epto,xy
*Get,RFRONTALB_Smax,node,109782,s,1
*Get,RFRONTALB_Smin,node,109782,s,3
*Get,RFRONTALB_Sx,node,109782,s,x
*Get,RFRONTALB_Sy,node,109782,s,y
*Get,RFRONTALB_Sxy,node,109782,s,xy

rsys,32
*Get,RFRONTALA_Emax,node,28432,epto,1
*Get,RFRONTALA_Emin,node,28432,epto,3
*Get,RFRONTALA_Ex,node,28432,epto,x
*Get,RFRONTALA_Ey,node,28432,epto,y
*Get,RFRONTALA_Exy,node,28432,epto,xy
*Get,RFRONTALA_Smax,node,28432,s,1
*Get,RFRONTALA_Smin,node,28432,s,3
*Get,RFRONTALA_Sx,node,28432,s,x
*Get,RFRONTALA_Sy,node,28432,s,y
*Get,RFRONTALA_Sxy,node,28432,s,xy

rsys,33
*Get,LFRONTALB_Emax,node,149645,epto,1
*Get,LFRONTALB_Emin,node,149645,epto,3
*Get,LFRONTALB_Ex,node,149645,epto,x
*Get,LFRONTALB_Ey,node,149645,epto,y
*Get,LFRONTALB_Exy,node,149645,epto,xy
*Get,LFRONTALB_Smax,node,149645,s,1
*Get,LFRONTALB_Smin,node,149645,s,3
*Get,LFRONTALB_Sx,node,149645,s,x
*Get,LFRONTALB_Sy,node,149645,s,y
*Get,LFRONTALB_Sxy,node,149645,s,xy

rsys,34
*Get,LFRONTALA_Emax,node,85814,epto,1
*Get,LFRONTALA_Emin,node,85814,epto,3
*Get,LFRONTALA_Ex,node,85814,epto,x
*Get,LFRONTALA_Ey,node,85814,epto,y
*Get,LFRONTALA_Exy,node,85814,epto,xy
*Get,LFRONTALA_Smax,node,85814,s,1
*Get,LFRONTALA_Smin,node,85814,s,3
*Get,LFRONTALA_Sx,node,85814,s,x
*Get,LFRONTALA_Sy,node,85814,s,y
*Get,LFRONTALA_Sxy,node,85814,s,xy

rsys,35
*Get,RTEMPORALA_Emax,node,3264,epto,1
*Get,RTEMPORALA_Emin,node,3264,epto,3
*Get,RTEMPORALA_Ex,node,3264,epto,x
*Get,RTEMPORALA_Ey,node,3264,epto,y
*Get,RTEMPORALA_Exy,node,3264,epto,xy
*Get,RTEMPORALA_Smax,node,3264,s,1
*Get,RTEMPORALA_Smin,node,3264,s,3
*Get,RTEMPORALA_Sx,node,3264,s,x
*Get,RTEMPORALA_Sy,node,3264,s,y
*Get,RTEMPORALA_Sxy,node,3264,s,xy

rsys,36
*Get,RTEMPORALB_Emax,node,59535,epto,1
*Get,RTEMPORALB_Emin,node,59535,epto,3
*Get,RTEMPORALB_Ex,node,59535,epto,x
*Get,RTEMPORALB_Ey,node,59535,epto,y
*Get,RTEMPORALB_Exy,node,59535,epto,xy
*Get,RTEMPORALB_Smax,node,59535,s,1
*Get,RTEMPORALB_Smin,node,59535,s,3
*Get,RTEMPORALB_Sx,node,59535,s,x
*Get,RTEMPORALB_Sy,node,59535,s,y
*Get,RTEMPORALB_Sxy,node,59535,s,xy

rsys,37
*Get,LTEMPORALA_Emax,node,9948,epto,1
*Get,LTEMPORALA_Emin,node,9948,epto,3
*Get,LTEMPORALA_Ex,node,9948,epto,x
*Get,LTEMPORALA_Ey,node,9948,epto,y
*Get,LTEMPORALA_Exy,node,9948,epto,xy
*Get,LTEMPORALA_Smax,node,9948,s,1
*Get,LTEMPORALA_Smin,node,9948,s,3
*Get,LTEMPORALA_Sx,node,9948,s,x
*Get,LTEMPORALA_Sy,node,9948,s,y
*Get,LTEMPORALA_Sxy,node,9948,s,xy

rsys,38
*Get,LTEMPORALB_Emax,node,144454,epto,1
*Get,LTEMPORALB_Emin,node,144454,epto,3
*Get,LTEMPORALB_Ex,node,144454,epto,x
*Get,LTEMPORALB_Ey,node,144454,epto,y
*Get,LTEMPORALB_Exy,node,144454,epto,xy

```
*Get,LTEMPORALB_Smax,node,144454,s,1
*Get,LTEMPORALB_Smin,node,144454,s,3
*Get,LTEMPORALB_Sx,node,144454,s,x
*Get,LTEMPORALB_Sy,node,144454,s,y
*Get,LTEMPORALB_Sxy,node,144454,s,xy


rsys,39
*Get,RSPHENOID_Emax,node,118238,epto,1
*Get,RSPHENOID_Emin,node,118238,epto,3
*Get,RSPHENOID_Ex,node,118238,epto,x
*Get,RSPHENOID_Ey,node,118238,epto,y
*Get,RSPHENOID_Exy,node,118238,epto,xy
*Get,RSPHENOID_Smax,node,118238,s,1
*Get,RSPHENOID_Smin,node,118238,s,3
*Get,RSPHENOID_Sx,node,118238,s,x
*Get,RSPHENOID_Sy,node,118238,s,y
*Get,RSPHENOID_Sxy,node,118238,s,xy


rsys,40
*Get,LSPHENOID_Emax,node,161522,epto,1
*Get,LSPHENOID_Emin,node,161522,epto,3
*Get,LSPHENOID_Ex,node,161522,epto,x
*Get,LSPHENOID_Ey,node,161522,epto,y
*Get,LSPHENOID_Exy,node,161522,epto,xy
*Get,LSPHENOID_Smax,node,161522,s,1
*Get,LSPHENOID_Smin,node,161522,s,3
*Get,LSPHENOID_Sx,node,161522,s,x
*Get,LSPHENOID_Sy,node,161522,s,y
*Get,LSPHENOID_Sxy,node,161522,s,xy


rsys,41
*Get,RZYGOMATICA_Emax,node,142960,epto,1
*Get,RZYGOMATICA_Emin,node,142960,epto,3
*Get,RZYGOMATICA_Ex,node,142960,epto,x
*Get,RZYGOMATICA_Ey,node,142960,epto,y
*Get,RZYGOMATICA_Exy,node,142960,epto,xy
*Get,RZYGOMATICA_Smax,node,142960,s,1
*Get,RZYGOMATICA_Smin,node,142960,s,3
*Get,RZYGOMATICA_Sx,node,142960,s,x
*Get,RZYGOMATICA_Sy,node,142960,s,y
*Get,RZYGOMATICA_Sxy,node,142960,s,xy


rsys,42
*Get,RZYGOMATICB_Emax,node,7197,epto,1
*Get,RZYGOMATICB_Emin,node,7197,epto,3
*Get,RZYGOMATICB_Ex,node,7197,epto,x
*Get,RZYGOMATICB_Ey,node,7197,epto,y
*Get,RZYGOMATICB_Exy,node,7197,epto,xy
*Get,RZYGOMATICB_Smax,node,7197,s,1
*Get,RZYGOMATICB_Smin,node,7197,s,3
*Get,RZYGOMATICB_Sx,node,7197,s,x
*Get,RZYGOMATICB_Sy,node,7197,s,y
*Get,RZYGOMATICB_Sxy,node,7197,s,xy


rsys,43
*Get,LZYGOMATICB_Emax,node,109456,epto,1
*Get,LZYGOMATICB_Emin,node,109456,epto,3
*Get,LZYGOMATICB_Ex,node,109456,epto,x
*Get,LZYGOMATICB_Ey,node,109456,epto,y
*Get,LZYGOMATICB_Exy,node,109456,epto,xy
*Get,LZYGOMATICB_Smax,node,109456,s,1
*Get,LZYGOMATICB_Smin,node,109456,s,3
*Get,LZYGOMATICB_Sx,node,109456,s,x
*Get,LZYGOMATICB_Sy,node,109456,s,y
*Get,LZYGOMATICB_Sxy,node,109456,s,xy


rsys,44
*Get,LZYGOMATICA_Emax,node,5778,epto,1
*Get,LZYGOMATICA_Emin,node,5778,epto,3
*Get,LZYGOMATICA_Ex,node,5778,epto,x
*Get,LZYGOMATICA_Ey,node,5778,epto,y
*Get,LZYGOMATICA_Exy,node,5778,epto,xy
*Get,LZYGOMATICA_Smax,node,5778,s,1
*Get,LZYGOMATICA_Smin,node,5778,s,3
*Get,LZYGOMATICA_Sx,node,5778,s,x
*Get,LZYGOMATICA_Sy,node,5778,s,y
*Get,LZYGOMATICA_Sxy,node,5778,s,xy


!brings the active coordinate back to the global
CS


CSys,0
wpave,0,0,0


etable,SE,SENE
SSUM
*GET, StrainE, SSUM,,ITEM,SE


finish
```
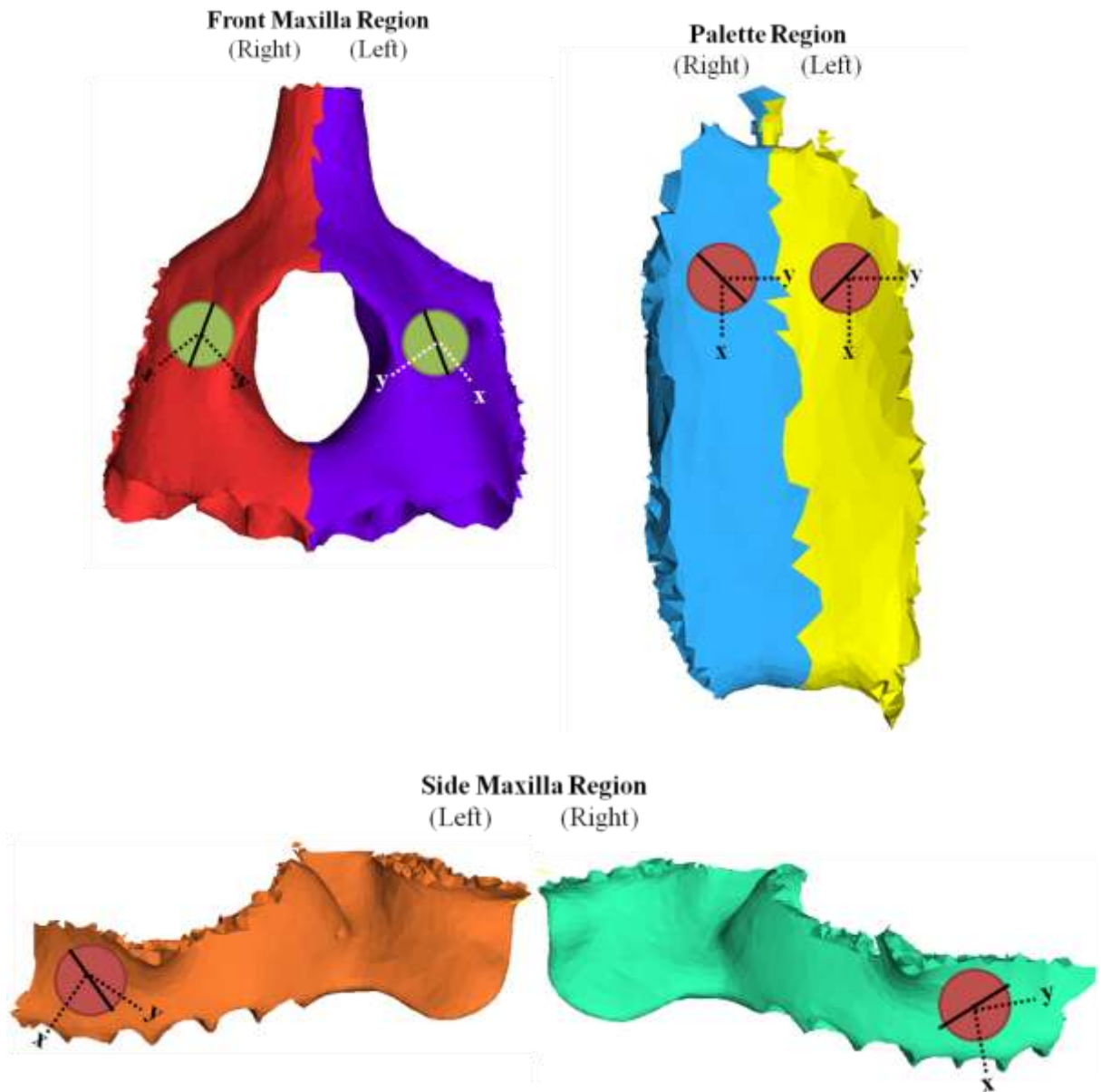
DATA AND INPUT FILES

C.I PCSA Data

Table 15: PCSA Data from Dr. Andrea Taylor's Lab: SM = superficial masseter; DM = deep masseter; MPt = medial pterygoid; TEMP = temporalis, WT = muscle mass in gm, LF = fiber length (mm); PINN = pinnation angle (in degrees); PCSA = physiologic cross-sectional area (cm2)

Specimen#	ABTCFR4	ABTCFR5	ABTCFR6	ABTCFR7
Genus	Cebus	Cebus	Cebus	Cebus
Species	apella	apella	apella	apella
Name	Maris	Shemp	Moe	Curley
Sex	F	M	M	M
SMWT	4.38	10.64	6.59	9.81
DMWT	1.25	0.00	1.68	3.32
MPtWT	1.66	#N/A	2.55	3.67
TEMPWT	12.34	43.59	17.33	28.83
AntTempWT	4.27	12.89	7.38	8.20
MidTempWT	4.75	20.37	6.88	12.92
PostTempWT	3.91	9.14	3.48	6.63
SMLF	9.00	10.35	8.48	11.74
SMPINN	21.08	29.97	24.58	23.73
SMPCSA	4.30	8.43	6.70	7.24
DMLF	8.66	7.36	10.64	10.10
DMPCSA	1.53	6.17	1.49	3.11
TMLF	11.39	17.91	13.52	18.40
TMPINN	16.74	22.59	18.75	17.77
TMPCSA	9.82	21.27	11.48	14.13
MPTLF	5.38	#N/A	7.84	6.17
MPTPINN	24.41	#N/A	35.33	34.93
MPTPCSA	4.36	#N/A	6.83	5.39

C.II   Setup of fixed coordinate systems on each anatomical Region

The maximum principal strain orientations presented in the circle elements below are all relative to the data from Table 5 and Figure 15.

Front Maxilla Region
(Right)   (Left)

Palette Region
(Right)   (Left)

Side Maxilla Region
(Left)   (Right)

Orbital Region
(Right)   (Left)
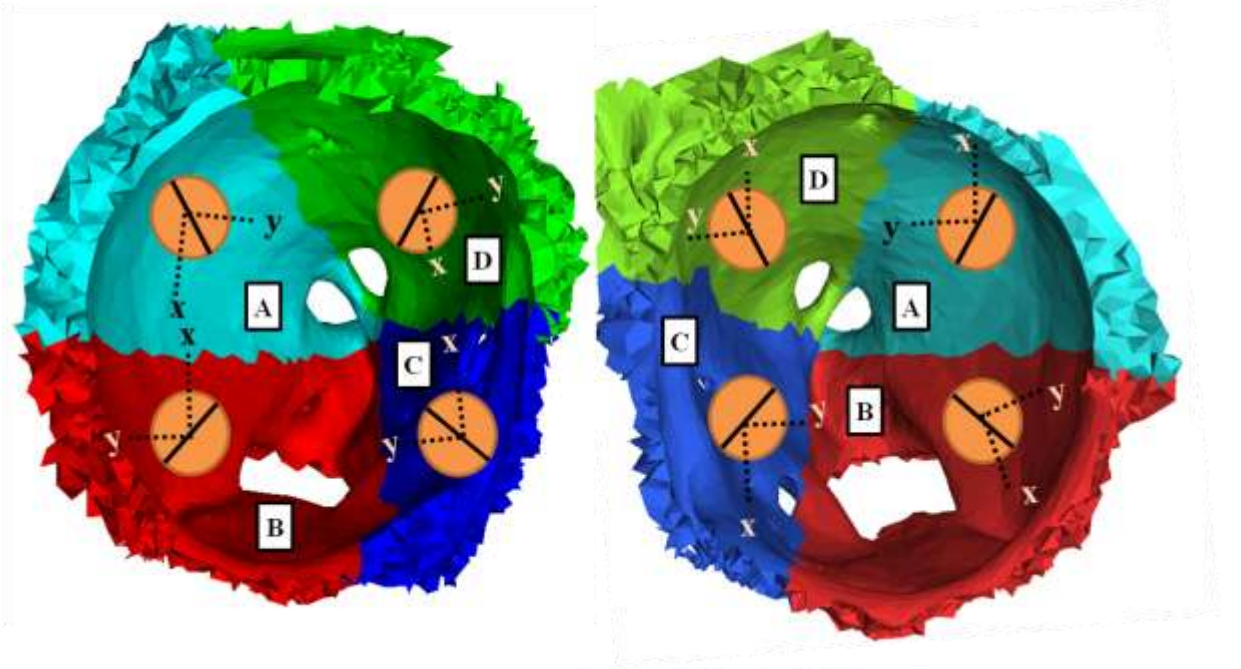
Parietal Region
(Right)   (Left)

Frontal Region

(Right)   (Left)

Temporal Regions

(Right)   (Left)

113
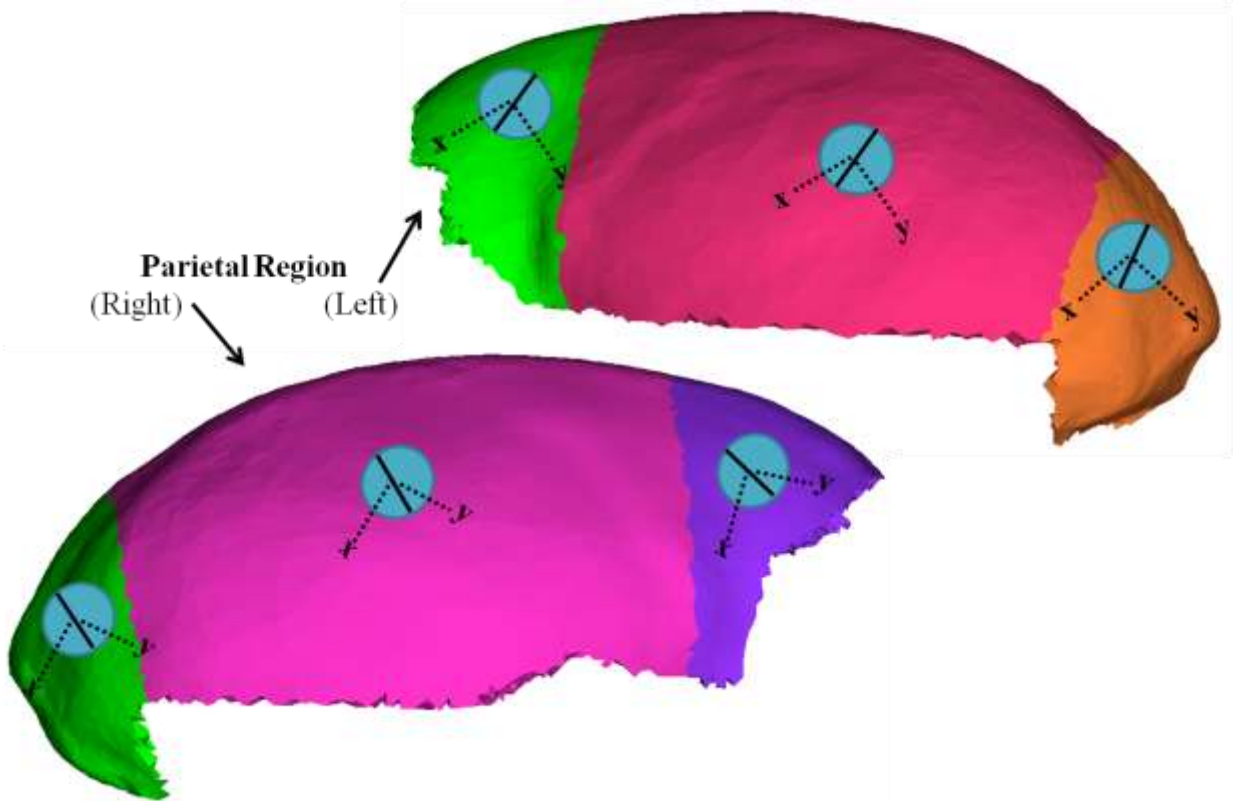
Sphenoid Region

(Right)　　　　　(Left)

Zygomatic Arch Region

(Left)

(Right)

C.III Relation of fixed-CS to rotated-CS at each anatomical region
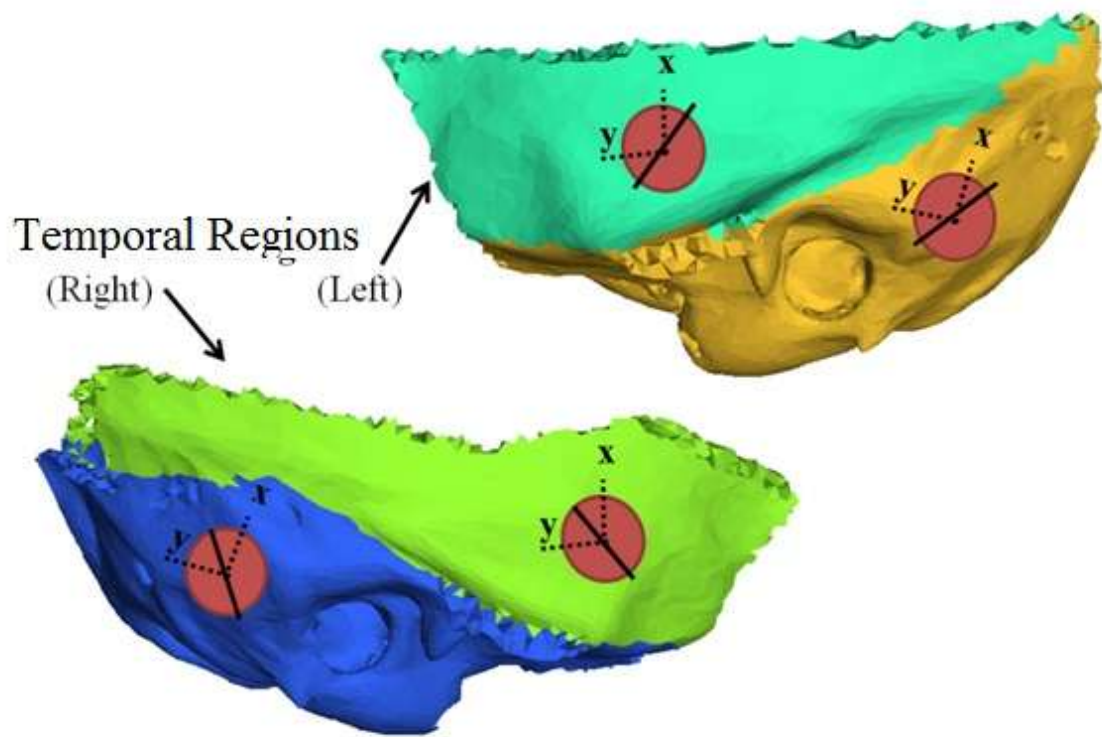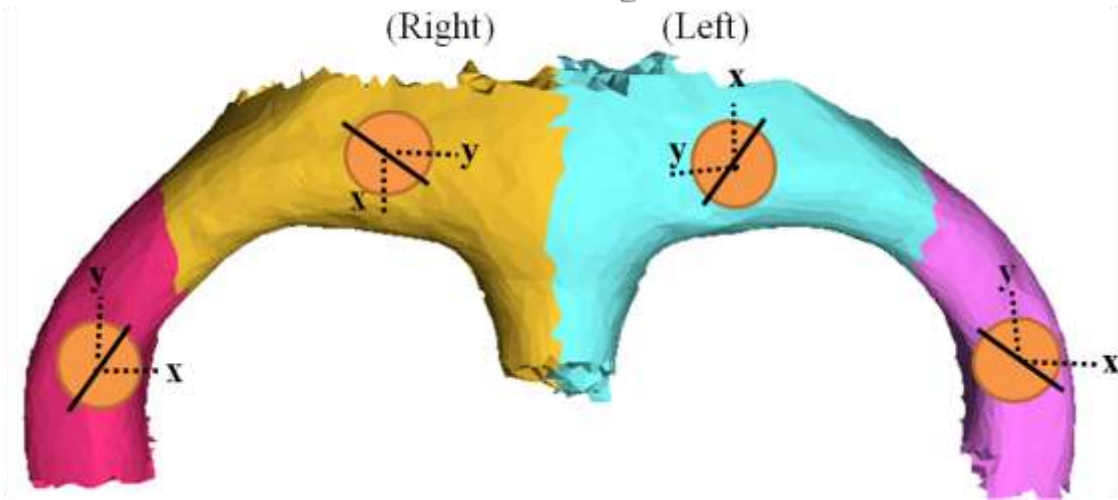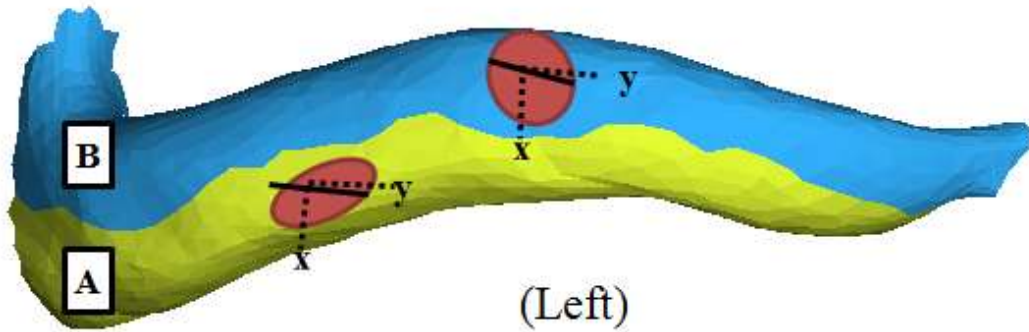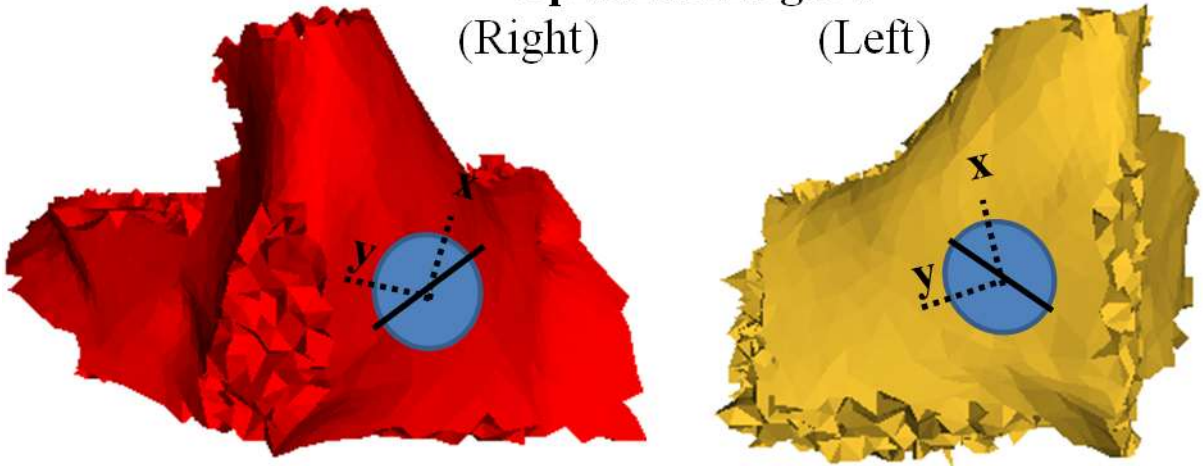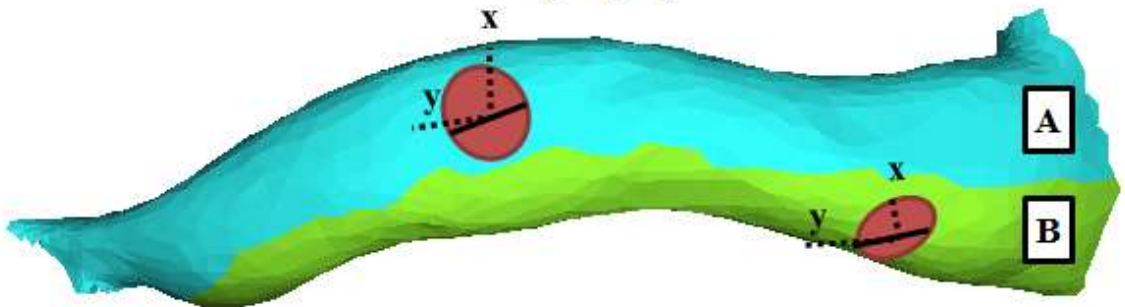
Table 16 : Relation of fixed-CS to rotated-CS with respect to x-axis and y-axis in terms of counter clockwise and clockwise angles

COMPONENT	Side	Curly Test matpr #	Curly Test cs #	cs #	Orientation of E3 (CC from y-axis)	Orientation of E3 (CC from x-axis)	Orientation of E3 (C from y-axis)	Orientation of E3 (C from x-axis)	origin center x	origin center y	origin center z
LCANINE	left	24	0	0	na						
LCANINE_PDL	left	28	0	0	na						
LM2	left	24	0	0	na						
LM2_PDL	left	28	0	0	na						
LP3	left	24	0	0	na						
LP3_PDL	left	28	0	0	na						
SEPTUM	both	27	0	0	na						
TRABECULAR_BONE	both	26	0	0	na						
RFMAXILLA	right	20	18996	11	110	20	70	160	76.146	70.806	733.542
LFMAXILLA	left	20	18997	12	70	160	110	20	76.362	59.74	733.598
RPALETTE	right	23	18998	13	140	50	40	130	60.676	67.698	728.784
LPALETTE	left	23	18999	14	40	130	140	50	61.297	61.454	729.228
RSMAXILLA	right	21	19000	15	32	122	148	58	59.166	81.282	728.691
LSMAXILLA	left	21	19001	16	148	58	32	122	61.943	47.209	731.764
RORBITALD	right	22	19002	17	85.3	175.3	94.7	4.7	79.029	68.073	705.519
RORBITALA	right	22	19003	18	175.3	85.3	4.7	94.7	75.331	75.081	703.164
RORBITALB	right	22	19004	19	85.3	175.3	94.7	4.7	67.116	75.84	712.25
RORBITALC	right	22	19005	20	175.3	85.3	4.7	94.7	68.98	65.608	708.739
LORBITALD	left	22	19006	21	94.7	4.7	85.3	175.3	76.818	56.404	704.205
LORBITALA	left	22	19007	22	4.7	94.7	175.3	85.3	74.852	49.909	705.391
LORBITALC	left	22	19008	23	94.7	4.7	85.3	175.3	69.367	60.617	705.15
LORBITALB	left	22	19009	24	4.7	94.7	175.3	85.3	65.431	54.724	703.702
RPARIETALA	right	15	19010	25	149	59	31	121	66.315	66.663	648.233
RPARIETALB	right	15	19011	26	149	59	31	121	86.468	78.368	671.608
RPARIETALC	right	15	19012	27	149	59	31	121	97.226	68.279	699.67
LPARIETALA	left	15	19013	28	121	31	59	149	66.297	47.79	650.491
LPARIETALB	left	15	19014	29	121	31	59	149	87.585	41.263	677.669
LPARIETALC	left	15	19015	30	121	31	59	149	95.649	50.935	706.442
RFRONTALB	right	16	19016	31	125.7	35.7	54.3	144.3	94.706	74.325	716.006
RFRONTALA	right	16	19017	32	125.7	35.7	54.3	144.3	84.157	87.85	714.778
LFRONTALB	left	16	19018	33	54.3	144.3	125.7	35.7	94.813	53.859	718.609
LFRONTALA	left	16	19019	34	54.3	144.3	125.7	35.7	82.709	40.854	720.728
RTEMPORALA	right	17	19020	35	125.4	35.4	54.6	144.6	64.781	86.999	687.082
RTEMPORALB	right	17	19021	36	125.4	35.4	54.6	144.6	54.123	75.356	669.611
LTEMPORALA	left	17	19022	37	54.6	144.6	125.4	35.4	66.99	35.562	691.466
LTEMPORALB	left	17	19023	38	54.6	144.6	125.4	35.4	51.419	36.733	675.128
RSPHENOID	right	19	19024	39	63.9	153.9	116.1	26.1	67.35	84.958	725.879
LSPHENOID	left	19	19025	40	116.1	26.1	63.9	153.9	69.212	48.191	723.721
RZYGOMATICA	right	18	19026	41	14	104	166	76	60.94	97.573	708.118
RZYGOMATICB	right	18	19027	42	14	104	166	76	58.155	94.104	707.247
LZYGOMATICB	left	18	19028	43	116	26	64	154	65.832	25.564	706.72
LZYGOMATICA	left	18	19029	44	116	26	64	154	61.355	28.046	710.745

115

C.IV   Probabilistic Design Input Variables and Output Parameters

PDVAR,theta_RFMAXILLA,TGAU,20,52,-70,110
PDVAR,theta_RPALETTE,TGAU,50,40,-40,140
PDVAR,theta_RSMAXILLA,TGAU,122,9,95,149
PDVAR,theta_RORBITALA,TGAU,85.3,13,46.3,124.3
PDVAR,theta_RPARIETALA,TGAU,59,77,-31,149
PDVAR,theta_RFRONTALB,TGAU,35.7,15,-9.3,80.7
PDVAR,theta_RTEMPORALA,TGAU,35.4,26,-42.6,113.4
PDVAR,theta_RSPHENOID,TGAU,153.9,17,102.9,204.9
PDVAR,theta_LZYGOMATICB,TGAU,21,9,-6,48

PDVAR,RFMAXILLA_Ex,
RESP
PDVAR,RFMAXILLA_Ey,
RESP
PDVAR,RFMAXILLA_Exy,
RESP

PDVAR,LFMAXILLA_Ex,R
ESP
PDVAR,LFMAXILLA_Ey,R
ESP
PDVAR,LFMAXILLA_Exy,
RESP

PDVAR,RPALETTE_Ex,RE
SP
PDVAR,RPALETTE_Ey,RE
SP
PDVAR,RPALETTE_Exy,R
ESP

PDVAR,LPALETTE_Ex,RE
SP
PDVAR,LPALETTE_Ey,RE
SP
PDVAR,LPALETTE_Exy,R
ESP

PDVAR,RSMAXILLA_Ex,
RESP
PDVAR,RSMAXILLA_Ey,
RESP
PDVAR,RSMAXILLA_Exy,
RESP

PDVAR,LSMAXILLA_Ex,R
ESP
PDVAR,LSMAXILLA_Ey,R
ESP
PDVAR,LSMAXILLA_Exy,
RESP

PDVAR,RORBITALA_Ex,R
ESP
PDVAR,RORBITALA_Ey,R
ESP
PDVAR,RORBITALA_Exy,
RESP

PDVAR,RORBITALB_Ex,R
ESP
PDVAR,RORBITALB_Ey,R
ESP
PDVAR,RORBITALB_Exy,
RESP

PDVAR,RORBITALC_Ex,R
ESP
PDVAR,RORBITALC_Ey,R
ESP
PDVAR,RORBITALC_Exy,
RESP

PDVAR,RORBITALD_Ex,R
ESP
PDVAR,RORBITALD_Ey,R
ESP
PDVAR,RORBITALD_Exy,
RESP

PDVAR,LORBITALA_Ex,R
ESP
PDVAR,LORBITALA_Ey,R
ESP
PDVAR,LORBITALA_Exy,
RESP

PDVAR,LORBITALB_Ex,R
ESP
PDVAR,LORBITALB_Ey,R
ESP
PDVAR,LORBITALB_Exy,
RESP

PDVAR,LORBITALC_Ex,R
ESP
PDVAR,LORBITALC_Ey,R
ESP
PDVAR,LORBITALC_Exy,
RESP

PDVAR,LORBITALD_Ex,R
ESP
PDVAR,LORBITALD_Ey,R
ESP
PDVAR,LORBITALD_Exy,
RESP

PDVAR,RPARIETALA_Ex,
RESP
PDVAR,RPARIETALA_Ey,
RESP
PDVAR,RPARIETALA_Exy
,RESP

PDVAR,RPARIETALB_Ex,
RESP
PDVAR,RPARIETALB_Ey,
RESP
PDVAR,RPARIETALB_Exy
,RESP

PDVAR,RPARIETALC_Ex,
RESP
PDVAR,RPARIETALC_Ey,
RESP
PDVAR,RPARIETALC_Exy
,RESP

PDVAR,LPARIETALA_Ex,
RESP
PDVAR,LPARIETALA_Ey,
RESP
PDVAR,LPARIETALA_Exy
,RESP

PDVAR,LPARIETALB_Ex,
RESP
PDVAR,LPARIETALB_Ey,
RESP
PDVAR,LPARIETALB_Exy
,RESP

PDVAR,LPARIETALC_Ex,
RESP
PDVAR,LPARIETALC_Ey,
RESP
PDVAR,LPARIETALC_Exy
,RESP

PDVAR,RFRONTALA_Ex,
RESP
PDVAR,RFRONTALA_Ey,
RESP
PDVAR,RFRONTALA_Exy
,RESP

PDVAR,RFRONTALB_Ex,
RESP
PDVAR,RFRONTALB_Ey,
RESP
PDVAR,RFRONTALB_Exy,
RESP

PDVAR,LFRONTALA_Ex,
RESP
PDVAR,LFRONTALA_Ey,
RESP
PDVAR,LFRONTALA_Exy,
RESP

PDVAR,LFRONTALB_Ex,
RESP

PDVAR,LFRONTALB_Ey,
RESP
PDVAR,LFRONTALB_Exy,
RESP

PDVAR,RTEMPORALA_E
x,RESP
PDVAR,RTEMPORALA_E
y,RESP
PDVAR,RTEMPORALA_E
xy,RESP

PDVAR,RTEMPORALB_Ex
,RESP
PDVAR,RTEMPORALB_Ey
,RESP
PDVAR,RTEMPORALB_Ex
y,RESP

PDVAR,LTEMPORALA_Ex
,RESP
PDVAR,LTEMPORALA_Ey
,RESP
PDVAR,LTEMPORALA_Ex
y,RESP

PDVAR,LTEMPORALB_Ex
,RESP
PDVAR,LTEMPORALB_Ey
,RESP
PDVAR,LTEMPORALB_Ex
y,RESP

PDVAR,RSPHENOID_Ex,R
ESP
PDVAR,RSPHENOID_Ey,R
ESP

PDVAR,RSPHENOID_Exy,
RESP

PDVAR,LSPHENOID_Ex,R
ESP
PDVAR,LSPHENOID_Ey,R
ESP
PDVAR,LSPHENOID_Exy,
RESP

PDVAR,RZYGOMATICA_
Ex,RESP
PDVAR,RZYGOMATICA_
Ey,RESP
PDVAR,RZYGOMATICA_
Exy,RESP

PDVAR,RZYGOMATICB_
Ex,RESP
PDVAR,RZYGOMATICB_
Ey,RESP
PDVAR,RZYGOMATICB_
Exy,RESP

PDVAR,LZYGOMATICA_
Ex,RESP
PDVAR,LZYGOMATICA_
Ey,RESP
PDVAR,LZYGOMATICA_
Exy,RESP

PDVAR,LZYGOMATICB_
Ex,RESP
PDVAR,LZYGOMATICB_
Ey,RESP
PDVAR,LZYGOMATICB_
Exy,RESP

APPENDIX D

RAW RESULTS

D.I   Study 1: In vivo vs In silico principal strains, shear strains, and orientation results Models A-D

Table 17: Fully activated EMG: Tensile (Max), Compressive (Min), Shear (Max-Min) strains ($\mu\varepsilon$), and orientations (^{o}) of tensile strain with respect to Element A on strain gage

			Mean Left Anterior Pillar ($\mu\varepsilon$)								
Measurement		In vivo	Model A		Model B		Model C		Model D	
			average	equilateral	average	equilateral	average	equilateral	average	equilateral
Max	(ε_1)	123.07	203.45	246.77	193.48	248.73	145.84	145.40	148.88	145.05
Min	(ε_3)	-86.52	-336.16	-387.67	-293.66	-325.51	-235.47	-280.97	-215.88	-263.42
Shr	(γ_{max})	206.94	539.61	634.44	487.15	574.24	381.31	426.36	364.75	408.47
El_A	(θ_p)	70.64	88.15	88.92	85.72	82.34	84.28	81.62	79.53	82.25

			Mean Right Anterior Pillar ($\mu\varepsilon$)								
Measurement		In vivo	Model A		Model B		Model C		Model D	
			average	equilateral	average	equilateral	average	equilateral	average	equilateral
Max	(ε_1)	65.50	77.06	53.11	78.66	50.11	70.20	54.55	74.95	58.57
Min	(ε_3)	-45.88	-16.42	-20.33	-30.52	-8.35	-28.61	-40.51	-32.02	-44.75
Shr	(γ_{max})	99.15	93.48	73.44	109.19	58.46	98.81	95.05	106.97	103.32
El_A	(θ_p)	76.93	50.69	55.36	60.17	68.15	60.91	46.90	61.37	49.46

			Mean Right Zygomatic Arch ($\mu\varepsilon$)								
Measurement		In vivo	Model A		Model B		Model C		Model D	
			average	equilateral	average	equilateral	average	equilateral	average	equilateral
Max	(ε_1)	129.59	263.56	324.42	269.92	287.29	249.79	312.43	253.92	289.31
Min	(ε_3)	-134.55	-165.37	-93.08	-155.85	-66.91	-172.23	-84.20	-152.37	-69.19
Shr	(γ_{max})	264.08	428.94	417.50	425.77	354.20	422.03	396.63	406.28	358.50
El_A	(θ_p)	68.87	82.47	70.71	80.78	69.95	83.11	69.81	79.70	68.38

Table 18: Scaled with respect to α values: Tensile (Max), Compressive (Min), Shear (Max-Min) strains (με), and orientations (⁰) of tensile strain with respect to Element A on strain gage

Measurement		In vivo	Mean Left Anterior Pillar (με)							
			Model A		Model B		Model C		Model D	
			average	equilateral	average	equilateral	average	equilateral	average	equilateral
Max	(ε_1)	123.07	91.94	92.36	94.83	105.00	83.38	69.05	88.34	73.43
Min	(ε_3)	-86.52	-151.91	-145.10	-143.93	-137.42	-134.62	-133.44	-128.10	-133.36
Shr	(γ_{max})	206.94	243.85	237.45	238.76	242.42	218.00	202.49	216.44	206.79
El_A	(θ_p)	70.64	88.15	88.92	85.72	82.34	84.28	81.62	79.53	82.25

Measurement		In vivo	Mean Right Anterior Pillar (με)							
			Model A		Model B		Model C		Model D	
			average	equilateral	average	equilateral	average	equilateral	average	equilateral
Max	(ε_1)	65.50	34.82	19.88	38.55	21.15	40.13	25.90	37.95	29.65
Min	(ε_3)	-45.88	-7.42	-7.61	-14.96	-3.52	-16.36	-19.24	-19.00	-22.66
Shr	(γ_{max})	99.15	42.24	27.49	53.52	24.68	56.49	45.14	56.95	52.31
El_A	(θ_p)	76.93	50.69	55.36	60.17	68.15	60.91	46.90	61.37	49.46

Measurement		In vivo	Mean Right Zygomatic Arch (με)							
			Model A		Model B		Model C		Model D	
			average	equilateral	average	equilateral	average	equilateral	average	equilateral
Max	(ε_1)	129.59	119.11	121.42	132.29	121.28	142.81	148.38	150.67	146.47
Min	(ε_3)	-134.55	-74.73	-34.84	-76.39	-28.24	-98.47	-39.99	-90.41	-35.03
Shr	(γ_{max})	264.08	193.84	156.26	208.68	149.52	241.27	188.37	241.09	181.50
El_A	(θ_p)	68.87	82.47	70.71	80.78	69.95	83.11	69.81	79.70	68.38

D.II   Study 1: In silico Orthotropic & Isotropic vs in vivo principal strains, shear strains, and orientation results Models A-D

Table 19: Fully Activated EMG: Tensile (Max), Compressive (Min), Shear (Max-Min) strains (µε), and orientations (º) of tensile strain with respect to Element A on strain gage

|			in silico		in vivo
			Orthotropic	Isotropic	
LPILL	Max	(ε_1)	143.20	203.45	123.07
	Min	(ε_3)	-247.17	-336.16	-86.52
	Shr	(γ_{max})	390.37	539.61	206.94
	El_A	(θ_p)	77.84	88.15	70.64
RPILL	Max	(ε_1)	81.03	77.06	65.50
	Min	(ε_3)	-59.35	-16.42	-45.88
	Shr	(γ_{max})	140.38	93.48	99.15
	El_A	(θ_p)	61.29	50.69	76.93
RZARCH	Max	(ε_1)	563.53	263.56	129.59
	Min	(ε_3)	-610.57	-165.37	-134.55
	Shr	(γ_{max})	1174.10	428.94	264.08
	El_A	(θ_p)	81.92	82.47	68.87

Table 20: α scaled: Tensile (Max), Compressive (Min), Shear (Max-Min) strains (με), and orientations (°) of tensile strain with respect to Element A on strain gage

| | | | in silico α scaled | | in vivo |
			Orthotropic	Isotropic	
LPILL	Max	(ε_1)	146.63	91.94	123.07
	Min	(ε_3)	-111.70	-151.91	-86.52
	Shr	(γ_{max})	176.41	243.85	206.94
	El_A	(θ_p)	77.84	88.15	70.64
RPILL	Max	(ε_1)	36.62	34.82	65.50
	Min	(ε_3)	-26.82	-7.42	-45.88
	Shr	(γ_{max})	63.44	42.24	99.15
	El_A	(θ_p)	61.29	50.69	76.93
RZARCH	Max	(ε_1)	254.66	119.10	129.59
	Min	(ε_3)	-275.92	-74.73	-134.55
	Shr	(γ_{max})	530.57	193.84	264.08
	El_A	(θ_p)	81.92	82.47	68.87

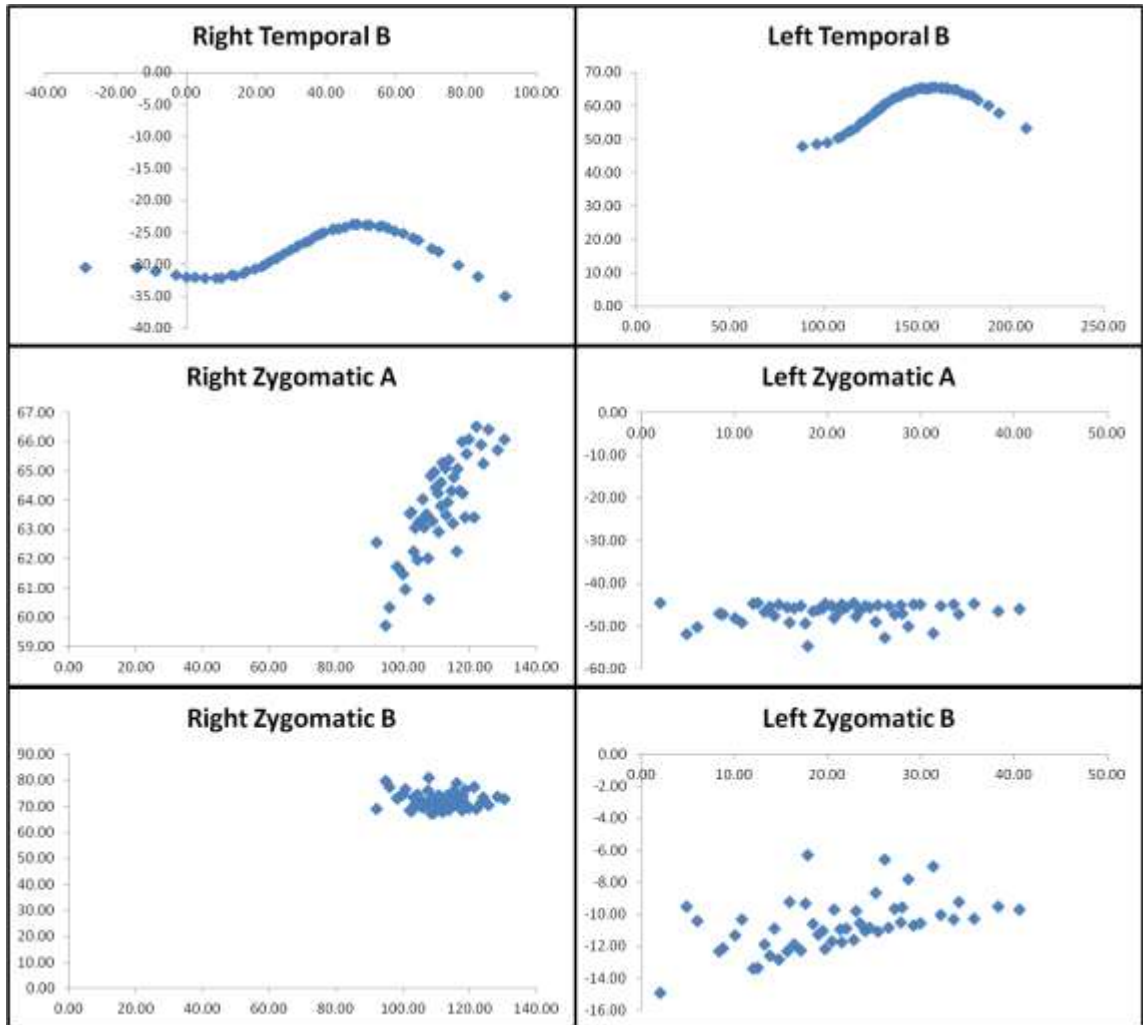## D.III   Study 2: Probabilistic Design Scatter Plots
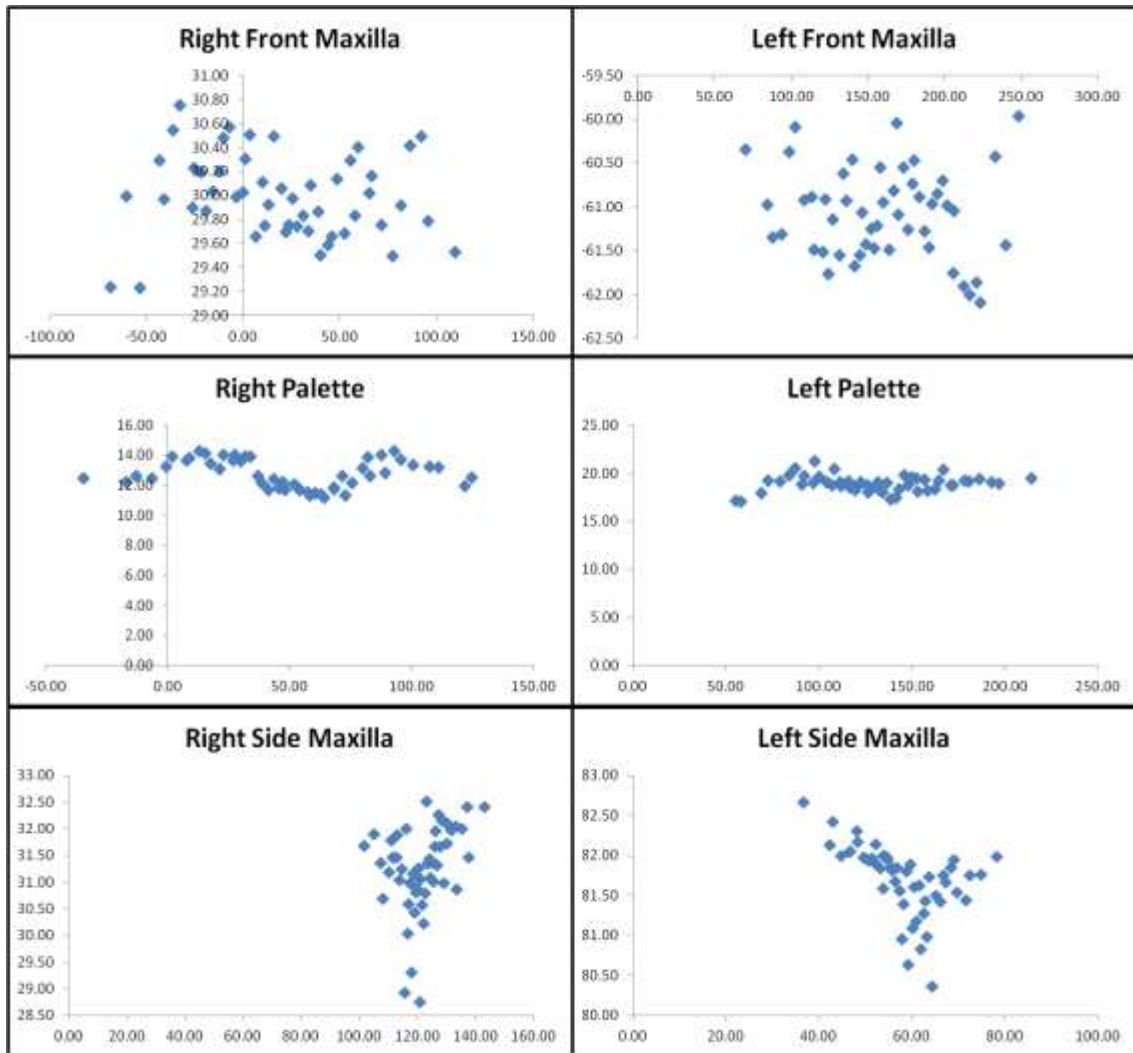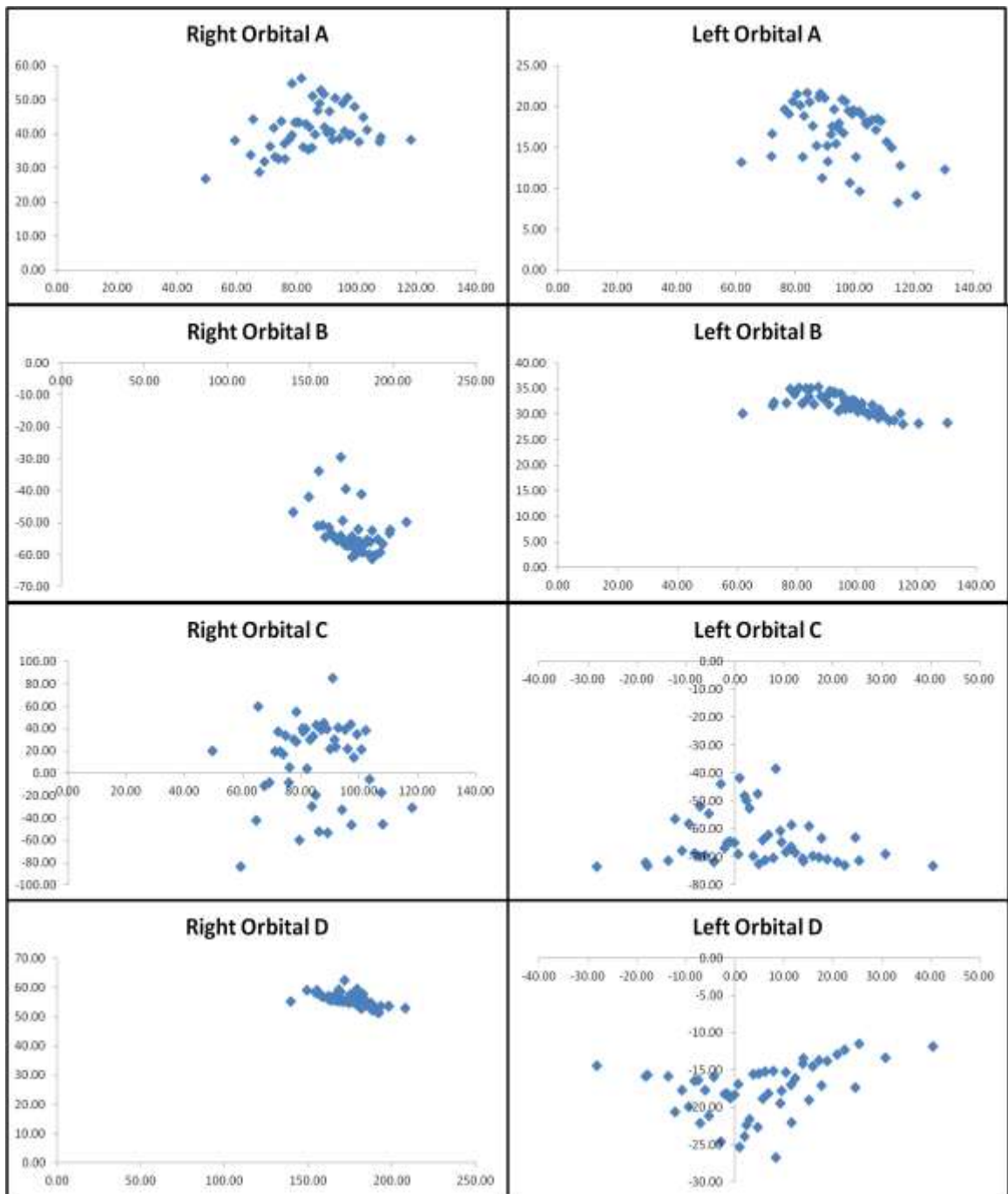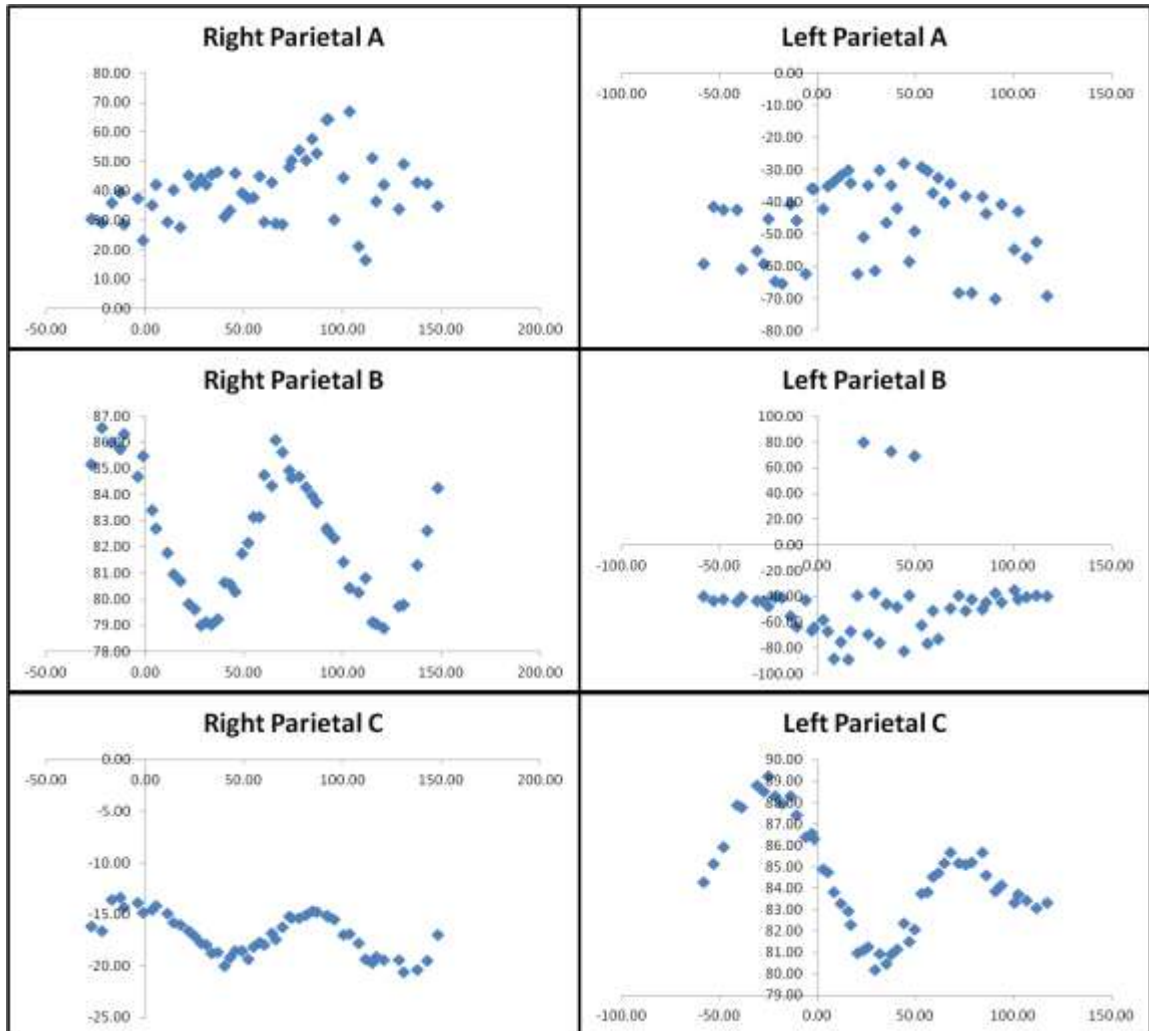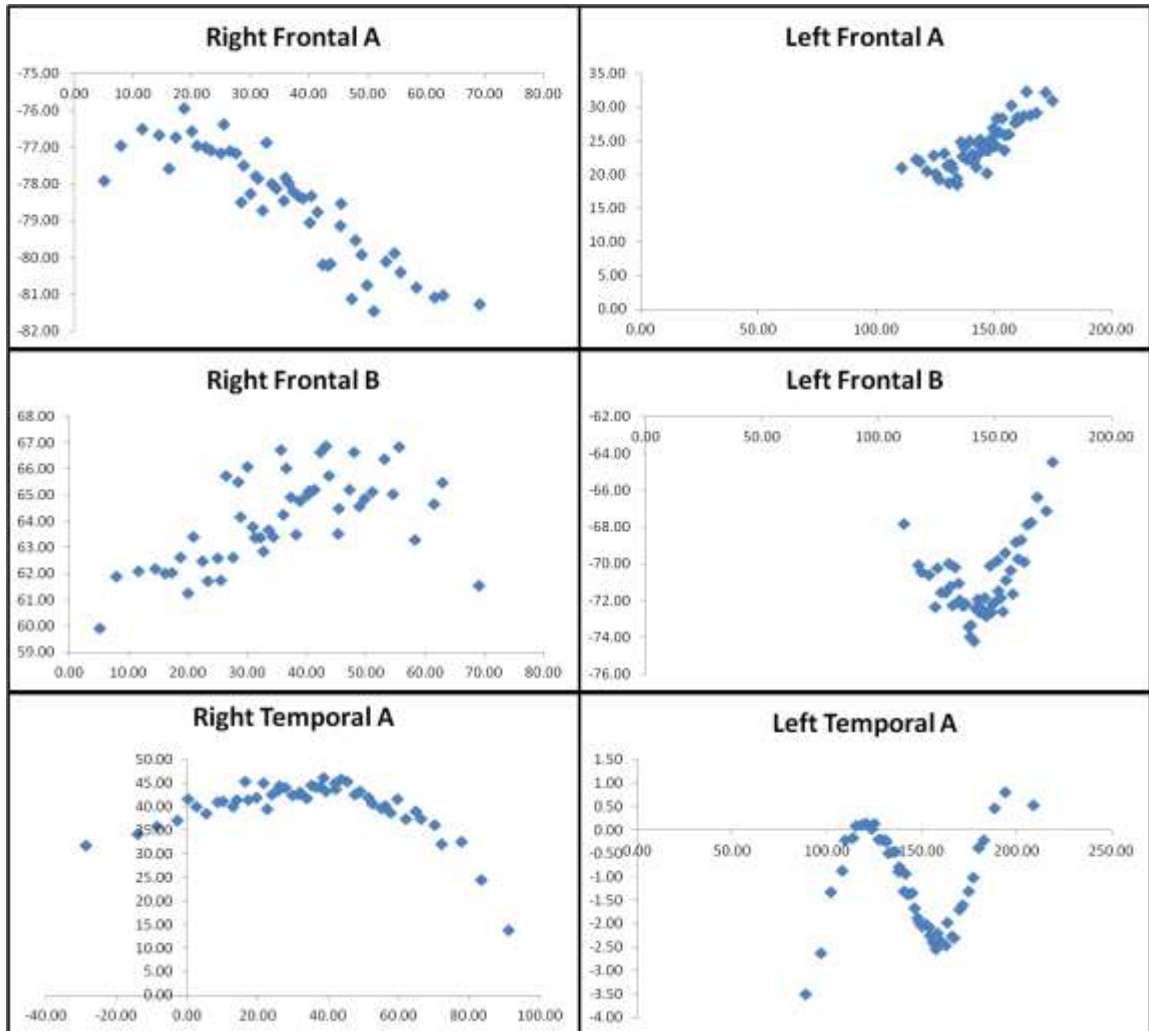
Figure 37: Plots of orientations for each anatomical region (x-axis: Material Property
Stiffness Orientation, y-axis: Maximum Principal Strain Orientation) in degrees

WORKS CITED

ANSYS Mechanical APDL Advanced Analysis Techniques GuideANSYS,
    INC2011Release 14.01-66.

Berthaume, Michael, et al. *Probabilistic Finite Element Analysis of a Craniofacial Finite
    Element Model.* Under Review ed., 2012*.

Berthaume, Michael, et al. "The Effect of Early Hominin Occlusal Morphology on the
    Fracturing of Hard Food Items." *The Anatomical Record: Advances in Integrative
    Anatomy and Evolutionary Biology* 293.4 (2010): 594-606.

Bright, Jen A., and Emily J. Rayfield. "Sensitivity and Ex Vivo Validation of Finite
    Element Models of the Domestic Pig Cranium." *Journal of anatomy* 219.4 (2011):
    456-71.

Bryan, Rebecca, et al. "Statistical Modelling of the Whole Human Femur Incorporating
    Geometric and Material Properties." *Medical engineering & physics* 32.1 (2010): 57-
    65.

Cook, R., et al. *Concepts and Applications of FInite Element Analysis.* University of
    Wisconsin- Madison: John Wiley & Sons Inc., 2002.

Davis, J. L., et al. "Predicting Bite Force in Mammals: Two-Dimensional Versus Three-
    Dimensional Lever Models." *Journal of Experimental Biology* 213.11 (2010): 1844-
    51.

Davis, Julian L., et al. "An Efficient Method of Modeling Material Properties using a
    Thermal Diffusion Analogy: An Example Based on Craniofacial Bone." *PLoS ONE*
    (2011).

Dechow, Paul C., Qian Wang, and Jill Peterson. "Edentulation Alters Material Properties
    of Cortical Bone in the Human Craniofacial Skeleton: Functional Implications for
    Craniofacial Structure in Primate Evolution." *The Anatomical Record: Advances in
    Integrative Anatomy and Evolutionary Biology* 293.4 (2010): 618-29.

Dumont, Elizabeth R., et al. "Finite Element Analysis of Performance in the Skulls of
    Marmosets and Tamarins." *Journal of anatomy* 218.1 (2011): 151-62.

Dumont, Elizabeth R., Justin Piccirillo, and Ian R. Grosse. "Finite-Element Analysis of
    Biting Behavior and Bone Stress in the Facial Skeletons of Bats." *The Anatomical
    Record Part A: Discoveries in Molecular, Cellular, and Evolutionary Biology*
    283A.2 (2005): 319-30.

Grosse, Ian R., et al. "Techniques for Modeling Muscle-Induced Forces in Finite Element Models of Skeletal Structures." *Anatomical Record-Advances in Integrative Anatomy and Evolutionary Biology* 290.9 (2007): 1069-88.

Helgason, Benedikt, et al. "Mathematical Relationships between Bone Density and Mechanical Properties: A Literature Review." *Clinical Biomechanics* 23.2 (2008): 135-46.

Herzog, W. "Muscle." *Biomechanics of the Musculo-Skeletal System.* Eds. B. M. Nigg and W. Herzog. Chichester, UK: Wiley, 1994. 154.

Huiskes, R., and E. Y. S. Chao. "A Survey of Finite Element Analysis in Orthopedic Biomechanics: The First Decade." *Journal of Biomechanics* 16.6 (1983): 385-409.

Hylander, W. L., and K. R. Johnson. "The Relationship between Masseter Force and Masseter Electromyogram during Mastication in the Monkey Macaca Fascicularis." *Archives of Oral Biology* 34.9 (1989): 713-22.

Kupczik, K., et al. "Masticatory Loading and Bone Adaptation in the Supraorbital Torus of Developing Macaques." *American Journal of Physical Anthropology* 139.2 (2009): 193-203.

Kupczik, K., et al. "Assessing Mechanical Function of the Zygomatic Region in Macaques: Validation and Sensitivity Testing of Finite Element Models." *Journal of anatomy* 210.1 (2007): 41-53.

Lucas, Peter W. *Dental Functional Morpholgy: How Teeth Work*. Cambridge: Cambridge University Press, 2004.

Marshall, Andrew, and Richard Wrangham. *Evolutionary Consequences of Fallback Foods.* 28 Vol. Springer Netherlands, 2007.

Olsson, A., and G. Sandberg. "Latin Hypercube Sampling for Stochastic Finite Element Analysis." *J. Eng. Mech.* (2002): 128.

Panagiotopoulou, Olga, Kornelius Kupczik, and Samuel N. Cobb. "The Mechanical Function of the Periodontal Ligament in the Macaque Mandible: A Validation and Sensitivity Study using Finite Element Analysis." *Journal of anatomy* 218.1 (2011): 75-86.

Perry, J., and C. Wall. "Scaling of the Chewing Muscles in Prosimians." *Primate Craniofacial Function and Biology.* Eds. C. Vinyard, M. Ravosa, and C. Wall. New York, NY: Springer, 2008. 217.

Peterson, Jill, and Paul C. Dechow. "Material Properties of the Human Cranial Vault and Zygoma." *The Anatomical Record Part A: Discoveries in Molecular, Cellular, and Evolutionary Biology* 274A.1 (2003): 785-97.

Rayfield, Emily J. "Finite Element Analysis and Understanding the Biomechanics and Evolution of Living and Fossil Organisms." *Annual Review of Earth and Planetary Sciences* 35 (2007): 541-76.

Richmond, Brian G., et al. "Finite Element Analysis in Functional Morphology." *The Anatomical Record Part A: Discoveries in Molecular, Cellular, and Evolutionary Biology* 283A.2 (2005): 259-74.

Ross, Callum F. "Does the Primate Face Torque?" *Primate Craniofacial Function and Biology.* Eds. C. Vinyard, M. Ravosa, and C. Wall. New York, NY: Springer, 2008. 63-81.

Ross, Callum F., et al. "In Vivo Bone Strain and Finite-Element Modeling of the Craniofacial Haft in Catarrhine Primates." *Journal of anatomy* 218.1 (2011): 112-41.

Ross, Callum F., and William L. Hylander. "In Vivo and in Vitro Bone Strain in the Owl Monkey Circumorbital Region and the Function of the Postorbital Septum." *American Journal of Physical Anthropology* 101.2 (1996): 183-215.

Ross, Callum F., et al. "Modeling Masticatory Muscle Force in Finite Element Analysis: Sensitivity Analysis using Principal Coordinates Analysis." *The Anatomical Record Part A: Discoveries in Molecular, Cellular, and Evolutionary Biology* 283A.2 (2005): 288-99.

Ross, Callum F. "In Vivo Function of the Craniofacial Haft: The Interorbital ?Pillar?" *American Journal of Physical Anthropology* 116.2 (2001): 108-39.

Schileo, Enrico, et al. "Subject-Specific Finite Element Models can Accurately Predict Strain Levels in Long Bones." *Journal of Biomechanics* 40.13 (2007): 2982-9.

Shellis, R. P., et al. "Variations in Molar Enamel Thickness among Primates." *Journal of human evolution* 35.4-5 (1998): 507-22.

Strait, D., et al. "Craniofacial Strain Patterns during Premolar Loading: Implications for Human Evolution." *Primate Craniofacial Function and Biology.* Eds. C. Vinyard, M. Ravosa, and C. Wall. New York, NY: Springer, 2008. 173.

Strait, David S., et al. "The Structural Rigidity of the Cranium of Australopithecus Africanus: Implications for Diet, Dietary Adaptations, and the Allometry of Feeding Biomechanics." *The Anatomical Record: Advances in Integrative Anatomy and Evolutionary Biology* 293.4 (2010): 583-93.

Strait, David S., et al. "Masticatory Biomechanics and its Relevance to Early Hominid Phylogeny: An Examination of Palatal Thickness using Finite-Element Analysis." *Journal of human evolution* 52.5 (2007): 585-99.

Strait, David S., et al. "Modeling Elastic Properties in Finite-Element Analysis: How Much Precision is Needed to Produce an Accurate Model?" *The Anatomical Record Part A: Discoveries in Molecular, Cellular, and Evolutionary Biology* 283A.2 (2005): 275-87.

Strait, David S., et al. "The Feeding Biomechanics and Dietary Ecology of Australopithecus Africanus." *Proceedings of the National Academy of Sciences of the United States of America* 106.7 (2009): 2124-9.

Swindler, Daris R. *Primate Dentition an Introduction to the Teeth of Non-Human Primates*. Cambridge, UK: Cambridge University Press, 2002.

Taddei, Fulvia, et al. "The Material Mapping Strategy Influences the Accuracy of CT-Based Finite Element Models of Bones: An Evaluation Against Experimental Measurements." *Medical engineering & physics* 29.9 (2007): 973-9.

Taylor, Andrea B., and Christopher J. Vinyard. "Jaw-Muscle Fiber Architecture in Tufted Capuchins Favors Generating Relatively Large Muscle Forces without Compromising Jaw Gape." *Journal of human evolution* 57.6 (2009): 710-20.

Theory Reference for the Mechanical APDL and Mechanical ApplicationsANSYS, INC2009Release 12.1RWUMassA.

Tsubota, Ken-ichi, et al. "Computer Simulation of Trabecular Remodeling in Human Proximal Femur using Large-Scale Voxel FE Models: Approach to Understanding Wolff's Law." *Journal of Biomechanics* 42.8 (2009): 1088-94.

Using Strand7: Introduction to the Strand7 Finite Element SystemStrand7 Pty Ltd.2010Edition 360.

Vogel, Erin R., et al. "Functional Ecology and Evolution of Hominoid Molar Enamel Thickness: Pan Troglodytes Schweinfurthii and Pongo Pygmaeus Wurmbii." *Journal of human evolution* 55.1 (2008): 60-74.

Wang, Qian, et al. "Surface Strain on Bone and Sutures in a Monkey Facial Skeleton: An in Vitro Approach and its Relevance to Finite Element Analysis." *Primate Craniofacial Function and Biology.* Eds. Chris Vinyard, Matthew J. Ravosa, and Christine Wall.Springer US, 2008. 149-172.

Wang, Qian, Dennis W. Ashley, and Paul C. Dechow. "Regional, Ontogenetic, and Sex-Related Variations in Elastic Properties of Cortical Bone in Baboon Mandibles." *American Journal of Physical Anthropology* 141.4 (2010): 526-49.

Wang, Qian, and Paul C. Dechow. "Elastic Properties of External Cortical Bone in the Craniofacial Skeleton of the Rhesus Monkey." *American Journal of Physical Anthropology* 131.3 (2006): 402-15.

Wood, Sarah A., et al. "The Effects of Modeling Simplifications on Craniofacial Finite Element Models: The Alveoli (Tooth Sockets) and Periodontal Ligaments." *Journal of Biomechanics* 44.10 (2011): 1831-8.

Wood, Sarah. "Assessing the Biomechanical Effect of Alveoli, Periodontal Ligaments, and Squamosal Sutures in Mammalian Crania." Masters Thesis University of Massachusetts Amherst, 2011. Print.Amherst, MA: .

Wright, B. "Craniodental Biomechanics and Dietary Toughness in the Genus Cebus." *Journal of human evolution* 48.5 (2005): 473-92.

Wroe, Stephen, et al. "High-Resolution Three-Dimensional Computer Simulation of Hominid Cranial Mechanics." *The Anatomical Record: Advances in Integrative Anatomy and Evolutionary Biology* 290.10 (2007): 1248-55.